# "Design of Transition-Metal/Zeolite Catalysts for Direct Conversion of Coal-derived CO<sub>2</sub> to Aromatics"

#### DOE

DOE Award #: DE-FE0031719

**Georgia Tech Research Corporation** 505 Tenth Street, NW Atlanta, GA 30318 DUNS: 09-739-4084

**Final Technical Report** Funding Period: 01/01/2019-06/30/2022 Submitted: 09/30/2022

Submitted to Office of Fossil Energy and Carbon Management **National Energy Technology Laboratory** 

PD: Dr. Christopher W. Jones (cjones@chbe.gatech.edu; 404-385-1683)

Contributing Pls: Dr. Andrew Modford

Contributing Pls: Dr. Andrew Medford

SENIOR/KEY INVESTIGATORS: Dr. Matthew Realff

Contributing Personnel: Dr. Iman Nezam, Mr. Gabriel Sabenca Gusmão,

Mr. Dhrumil Shah, Ms. Laura Proaño, Mr. Wei Zhou, Dr. Kristina Golub NETL Program Manager: Naomi R. O'Neil (Naomi.Oneil@netl.doe.gov)

# **Table of Contents**

Disclaimer	4
Acknowledgements	4
Executive Summary	5
Body of the Report	6
I. Overview of the Technology	6
II. Goals and Objectives for the Project	7
III. Task 1.0 - Project Management and Planning	
IV. Task 2.0 - Preliminary Technology Feasibility Study	8
V. Task 3.0 – Retrofitting Reactor  A. Goals and Objectives of the Task  B. Background and Experimental Methods  C. Results and Discussion  D. Conclusions	9 9
VI. Task 4.0 Experimental Testing of Baseline Systems  A. Goals and Objectives of the Task  B. Background and Experimental Methods  C. Results and Discussion  D. Conclusions	11 12 13
VII. Task 5.0 – Computational Modeling of Baseline Systems  A. Goals and Objectives of the Task  A. Background and Research Methods  B. Results and Discussions  C. Conclusion	31 31
VIII. Task 6.0 – Experimental testing of different zeolite crystallite structure sizes	43 43
IX. Task 7.0 – Computational screening model development  A. Goals and Objectives of the Task  B. Background and Research Methods  C. Results and Discussions  D. Conclusions	48 48 48
X. Task 8.0 – Experimental testing of chemical mixtures (hydrogenation catalyst supported on zeolite catalyst)	

B. Background and Research Methods	56
C. Results and Discussions	
D. Conclusions	61
W. Tarloon, Constitution of the constitution	64
XI. Task 9.0 – Computational screening of alloy compositions	
A. Goals and Objectives of the Task	
B. Objectives and Research Methods	
C. Results and Discussions	
D. Conclusions	67
XII. Task 10.0 – Experimental testing of new alloy compositions	67
A. Goals and Objectives of the Task	67
B. Objectives and Research Methods	
C. Results and Discussions	68
D. Conclusions	70
XIII. Task 11.0 – Refine mechanism based on presence of aromatics	71
A. Goals and Objectives of the Task	
B. Background and Research Methods	
A. Results and Discussions	
B. Conclusions	87
II. Task 12.0 – Experimental optimization of conditions for best alloy	87
A. Goals and Objectives of the Task	87
B. Background and Research Methods	
C. Results and Discussions	88
D. Conclusions	89
III. Task 13.0 – Technology assessment of intensified reactor	89
A. Goals and Objectives of the Task	
B. Background and Research Methods	
C. Results and Discussions	
D. Conclusions	
IV. References	00
IV. REIEIEILES	99

#### Disclaimer

This report was prepared as an account of work sponsored by an agency of the United States Government. Neither the United States Government nor any agency thereof, nor any of their employees, makes any warranty, express or implied, or assumes any legal liability or responsibility for the accuracy, completeness, or usefulness of any information, apparatus, product, or process disclosed, or represents that its use would not infringe privately owned rights. Reference herein to any specific commercial product, process, or service by trade name, trademark, manufacturer, or otherwise does not necessarily constitute or imply its endorsement, recommendation, or favoring by the United States Government or any agency thereof. The views and opinions of authors expressed herein do not necessarily state or reflect those of the United States Government or any agency thereof.

### **Acknowledgements**

This material is based upon work supported by the Department of Energy under Award Number DE-FE0031719.

## **Executive Summary**

This project introduces a lab-scale, stand-alone process to produce aromatics from CO<sub>2</sub>. Besides reducing the amount of coal-derived CO<sub>2</sub> emission, this process can provide new approaches to produce valuable chemicals such as benzene, toluene, and xylene (BTX). These chemicals are the starting material in various industries such as pharmaceuticals, polymers, paints, and coatings. The focus of the project is on developing a suitable reaction configuration, feed composition, and catalyst combination that leads to high aromatics selectivity and CO<sub>2</sub> conversions. To achieve these objectives, computational catalysis will accompany hands-on experiments to provide insights to potential transition metals or alloys that may serve as optimal active sites for different steps of the reaction mechanism, such as reduction of CO<sub>2</sub> and dehydration (in the case of alcohol intermediates) and oligomerization (in the case of paraffins or olefins) of intermediate hydrocarbons.

Task 3.0 focused on rebuilding and retrofitting the experimental apparatus for the production of aromatics from CO<sub>2</sub>. Task 4.0 involved the experimental testing of the baseline system. Catalysts such as Cu/Zn/Al, ZnZrOx (ZnZrO), ZnGa2O4 are studied for conversion of CO<sub>2</sub> to MeOH. Of the three catalysts studied, it was found that the ZnZrO catalyst shows the optimum performance for MeOH production. Of the multiple H-ZSM-5 synthesized with varying Si/Al and mixed with ZnZrO and tested for CO2 hydrogenation, H-ZSM-5 with Si/AI = 300 shows the best performance. This catalyst was then further tested for optimum performance with respect to WHSV and temperature. It was found that temperature of 320 °C, WHSV of 7200 mL/gcat/h shows the best performance. The best performing catalyst ZnZrO/H-ZSM-5-300 was tested for optimum performance for varying CO<sub>2</sub>/H<sub>2</sub> ratio between 1 to 6. It was found that the ratio CO<sub>2</sub>/H<sub>2</sub> = 3 would show the maximum selectivity for aromatics. In task 6.0, H-ZSM-5 of varying sizes were tested in different patterns of fixed bed arrangements. Of the 3 patterns considered, mixed particle arrangement shows the best performance for CO<sub>2</sub> hydrogenation for high selectivity for aromatics production. However, in the case of mixed particle arrangement, it found that optimum an H-ZSM-5 particle size exists where the selectivity for aromatics for CO<sub>2</sub> hydrogenation is highest. This is based on the interaction between the two catalysts and the optimal distance between ZnZrO and H-ZSM-5 is observed when H-ZSM-5 of 300 nm is used. Hence, ZnZrO/H-ZSM-5 has the best performance catalyst combination with respect to high aromatics selectivity. To further minimize the distance between the two catalysts, H-ZSM-5 was impregnated with ZnZrO as part of Task 8.0. While the aromatics production rate increased, the rate of paraffins production also increased leading to lower aromatics selectivity as compared to physically mixed catalysts. Based on the results from Task 9.0, catalysts NiGa/SiO<sub>2</sub>, PdGa/SiO<sub>2</sub> and PdZn/SiO<sub>2</sub> were tested with varying temperatures and WHSV. While all the three catalysts still show very low selectivity for MeOH compared to ZnZrO, PdGa/SiO<sub>2</sub> shows the best performance of the 3 catalysts. The best performing catalyst PdGa/SiO<sub>2</sub> was mixed with H-ZSM-5 and tested for CO<sub>2</sub> hydrogenation for aromatics production. PdGa/SiO<sub>2</sub>/H-ZSM-5 shows little to no production of aromatics at

temperatures between 280-340 °C. Hence, from the experimental studies done in this project, ZnZrO/H-ZSM-5 shows the highest aromatics selectivity.

Computational tasks entailed constructing ab-initio screening and mechanistic macroscale models to guide catalyst selection and support chemical process design, respectively. In Task 5.0 a baseline microkinetic model was built based on the CO<sub>2</sub> reduction model by Grabow et. al.<sup>1</sup> encompassing methanol and reverse water-gas shift reaction (RWGS) reaction routes specifically for Cu(211). The microkinetic model was extended to other reactions involving oxygenates 1-3 and hydrocarbons 4 routes, and assessed over different temperature and pressure ranges. In Task 7.0 additional density functional theory (DFT) calculations were carried out for other transition metals, e.g. Pd, Pt, Ag, Au, Rh. Binding energies for CO\* and O\* were utilized as descriptors to determine regions of higher methanol selectivity given the same microkinetic model structure. In task 9, the descriptor-based approach was applied to bimetallic catalysts over a wide range of metal combinations available in the CatalysisHub database, which provided insights into potential active sites, and hence catalyst formulation. Since experimental results for metal-oxide-based tandem catalysts exhibited higher performance than transition metals, a macroscale kinetic model was developed in Task 11 based on experimental data. A lumped-kinetic model for methanol synthesis was readjusted based on Froment's CuZnO/Al<sub>2</sub>O<sub>3</sub> model and several machine-learning based strategies were developed to provide a Langmuir-Hinshelwood-Hougen-Watson (LHHW) kinetic model for the methanol conversion to aromatics and hydrocarbons over ZSM-5.

In Task 13.0, the process was studied for carbon footprint based on duties estimated in an Aspen simulation done for this reaction. The current commercial process of benzene production was used as basis for comparison of the carbon footprint of the current process. It was found that this process has 4 times the impact estimated in current benzene production pathway. However, there is still potential of decreasing the carbon footprint. In Subtask 13.2, we find that simply purifying the waste CO<sub>2</sub> could potentially decrease the utilities and hence the overall cost as well as carbon footprint.

# **Body of the Report**

# I. Overview of the Technology

This project aims to develop a technology for the conversion of coal-derived CO<sub>2</sub> directly into mixed aromatic chemicals that are currently sourced from petroleum. Aromatic chemicals such as benzene, toluene, and xylenes (BTX) face growing demand due to their expanding use in plastics and packaging, chiefly in poly(ethylene terephthalate) (PET). BTX is normally produced from oil in a petroleum refinery via multiple steps, involving several different reactions and separations. In this project we will explore a process intensification effort that begins the development of a new technology for the conversion of coal-derived CO<sub>2</sub> directly into BTX in a single reactor. This approach involves hydrogenation of CO<sub>2</sub> into methanol or short chain alkanes and related olefins,

which subsequently encounters a second catalyst that converts the intermediate species to BTX in the same reactor. A BTX production technology based on this reaction scheme would significantly deviate from the state-of-the-art, allowing the use of CO<sub>2</sub> as a feedstock, reducing the number of process steps and unit operations, and allowing smaller, more modular installations, which is commensurate with siting near large coal-fired power plants, minimizing costs of CO<sub>2</sub> storage and transportation.

Some studies have investigated BTX production from species like methanol or syngas using bifunctional metal/zeolite composites,<sup>5–7</sup> but the in-situ production of these intermediates from CO<sub>2</sub> will be addressed in this project. The proposed transition-metal (TM)/zeolite catalyst platform couples known metallic hydrogenation catalysts (Cu, Co) with known zeolitic aromatization catalysts (ZSM5). Other bifunctional metal/zeolite composites have been investigated for syngas conversion to methanol or alkanes, followed by aromatization on the acid site.<sup>8,9</sup> However, the direct synthesis of aromatics from CO<sub>2</sub> using bifunctional catalysts has rarely been reported.<sup>5,6</sup>

By changing process/material variables, the TM/ZSM5 catalyst systems could selectively produce one particular light aromatic component, or even one isomer within the xylenes. This can substantially reduce separation costs downstream. A detailed evaluation of a target selling price for this technology is not currently accessible because of the current low Technology Readiness Level (TRL) of this process; this has been addressed over the course of the project as the technology developed, and a techno-economic report is also submitted as part of this project.

Our approach involves combining catalysts that produce (i) methanol from CO<sub>2</sub> or (ii) hydrocarbons from CO<sub>2</sub> with zeolite catalysts that convert alcohols and/or hydrocarbons to aromatics.

# II. Goals and Objectives for the Project

The overall objective of this project is to design and test catalytic materials for the direct conversion of coal-derived CO<sub>2</sub> into mixed aromatic chemicals (benzene, toluene and xylenes (BTX)). BTX are currently produced from oil in a petroleum refinery in multiple reaction and separation steps. In this project, a single reactor will be used for the hydrogenation of coal-derived CO<sub>2</sub> into methanol or light alkanes on one catalyst followed by conversion to BTX on a separate catalyst. The development of this technology will be completed with a combined experimental and theoretical modeling approach. Specific objectives include: (i) synthesis and testing of composite catalytic materials that include known methanol (Cu) and hydrocarbon (Co) synthesis catalysts mixed with a known aromatization catalyst (ZSM5); (ii) varying material and reaction properties such as catalyst domain size or reactant composition to investigate effects on measured rates and selectivities; (iii) developing a microkinetic computational model on baseline systems and extending to various alloys and reactant compositions; (iv) refining computational mechanism(s) based on experimental data and including product interactions and

subsequent reactions into the model for more realistic surface coverage effects; and (v) synthesis of alloys based on computational models to improve selectivities to BTX species. In addition to the mentioned metals above, other metallic/metal oxide catalysts may be evaluated based on the primary results obtained and the up-to-date literature review. The primary objectives of the first year are retrofitting the current reactor and computational/ experimental investigation of existing baseline systems known to work independently, including conversion/selectivity as a function of reactant composition. In the second year, the main objectives were to synthesize more complex composite catalyst systems, to develop reaction/transport models, and to improve computational models for screening of alloys. In the third year, computational model refinement to include adsorbate interactions, synthesis and testing of alloys predicted from theory, as well as completion of a technical and economic feasibility assessments were primary objectives.

### III. Task 1.0 - Project Management and Planning

### A. Summary of Project Management Activities

This project began on January 1st, 2019. The Project Director (PD), Jones, gave a project overview at the kick-off meeting held through WebEx on March 19th, 2019. In the first quarter, a Ph.D. student, Gabriel Sabenca Gusmao was hired to lead the computational-catalysis related tasks in the project. Later, near the end of the first quarter, a post-doctoral researcher, Iman Nezam, joined the group for the experimental activities. Prior to Dr. Nezam's arrival, Dr. Kristina Golub assessed the current state of the reactor, identified replacement components, and aided Dr. Nezam's planning for reactor rebuild activities. In June 2021, a Ph.D. student, Dhrumil Rajendra Shah took over the project from Dr. Nezam and carried out the project along with another Ph.D. student, Laura Proaño from the experimental catalysis front. Around January 2021, Elizabeth Clayton, an undergraduate student at Georgia Tech, contributed a techno-economic analysis based on the results obtained from computational and experimental catalysis results.

Regular monthly meetings were held throughout the funding period with all the involved parties regularly updating the results obtained as the tasks were performed, to define the path ahead. A quarterly project report was submitted to DOE as promised with an annual update presentation provided by PD, Prof. Jones.

# IV. Task 2.0 - Preliminary Technology Feasibility Study

The TMP was developed and submitted to the program manager before its due date on July 1<sup>st</sup>, 2019. This document, describes the purpose and commercial applications of the project, reviews the current state-of-the-art concept, and discusses its current technology readiness level (TRL). Further, it describes a three-year approach to improve this TRL, and finally suggests some post-project plans upon the successful implementation of the 3-year approach.

# V. Task 3.0 - Retrofitting Reactor

### A. Goals and Objectives of the Task

The objective of the task is to retrofit an existing reactor with new lines, storage tanks, back-pressure regulators, etc., to remove any traces of previously used H<sub>2</sub>S in the reaction system. Pressure testing and Gas Chromatography (GC) calibration needed to be performed to verify the system functionality per expectations.

### B. Background and Experimental Methods

The reactor system that is already in place for the experimental section has been previously used for a project that involved sulfur as one of the chemicals in the stream. Therefore, substantial sulfur contamination was expected to be present in the gas piping and reactor apparatus. This required replacing all parts that were associated with the chemicals in the system. Also, some minor modifications needed to be done to make the former system compatible with the current project requirements. The system was studied to assess and order parts needed for replacements and make the appropriate changes needed to make the reactor system effective for studies in this project.

#### C. Results and Discussion

The process of retrofitting the reactor was completed during the third quarter. The reactor system that is already in place for the experimental section has been previously used for a project that involved sulfur as one of the chemicals in the stream. Therefore, substantial sulfur contamination was expected to be present in the gas piping and reactor apparatus. This required replacing all parts that were associated with the chemicals in the system. Also, some minor modifications needed to be done to make the former system compatible with the current project requirements. Among these modifications are upgrading the gas booster, backpressure regulators, pressure transducers, and adding extra feed flow controllers and the liquid feed injection stream. A schematic of the process installed is shown in Figure 1. All of the parts were tested for the approval of their performance and calibrated for enhancing their precision. For instance, during the tests, it was found that the two mass flow controllers (MFCs) that are located before the reactors were sized for a different range of flow rates than what was ordered originally. Therefore, the parts were returned and asked for recalibration at the vendor's expense.

The reaction setup involved a 1/4" diameter tube with a 10"-long heated zone along with a heated chamber that keeps the temperature of the product stream above 140 °C in the vapor phase and a wax trap for considering the unlikely event of the formation of wax products during the reaction.

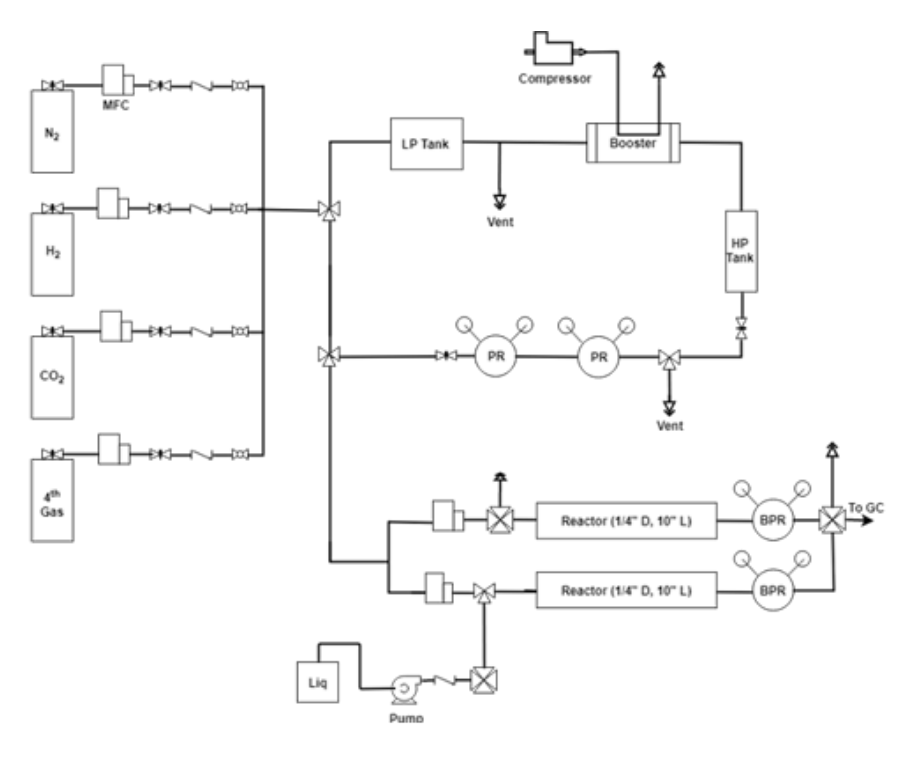


Figure 1: Schematics of the CO<sub>2</sub> aromatization process setup

Besides the parts discussed so far in this document and previous quarterly reports, a cofeed liquid pump was added to the process setup for bringing the flexibility of doing experiments with liquid samples as the feed. This will become useful for studying the performance of reaction intermediates at experimental conditions. Also, as it will be discussed later, gas chromatography (GC) peak calibrations can be done using this liquid pump. An up-to-date picture of the experimental setup is shown in Figure 2.

Aside from the experimental rig, an in-house created LabVIEW program had been developed. This program provides the opportunity to control and log variable changes throughout the experimental analysis without the need to be present on-site, which is considered as a valuable safety feature for this setup. Figure 3 shows two of the main sections of this program. The parameters that can be controlled and stored through this program are the feed flow rate, pressure and reactor temperature at different locations within the unit. Additionally, the program includes a safety protocol that gets activated upon surpassing the process temperature or pressure of a certain value. This activation happens by automatically shutting down the heat sources within the process.

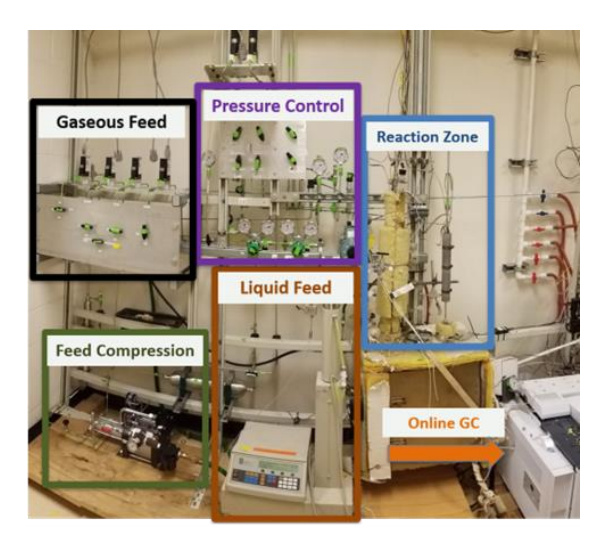


Figure 2: Picture of the experimental rig

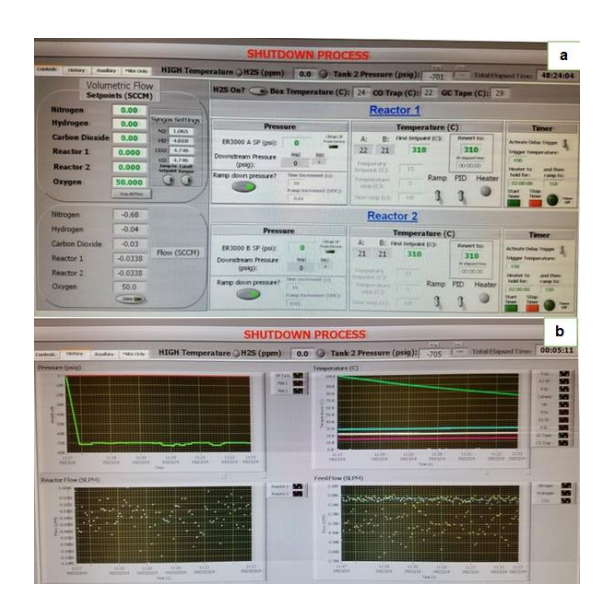


Figure 3: LabVIEW program developed for experimental analysis. 3a: Control unit 3b: Log unit

### **D.** Conclusions

In this task, an already existing reactor was retrofitted appropriately for this study. As shown in Figure 1, the setup has been designed keeping in mind the requirement for high pressure in our studies as well as the capability to log important reactor conditions with time autonomously.

## VI. Task 4.0 Experimental Testing of Baseline Systems

# A. Goals and Objectives of the Task

The goal of this task is to define a baseline system based on the up-to-date literature review. Known methanol and hydrocarbon synthesis catalysts will initially be tested, followed by combinations of those catalysts with a known aromatization catalyst (ZSM5) to benchmark the reactor system against up-to-date literature data.

<u>Subtask 4.1 - Experimental evaluation of "control" catalysts:</u> A commercially established transition metal alloy catalyst will be used for initial CO<sub>2</sub> conversion. This catalyst will not only be purchased commercially but also be synthesized in the lab. Post routine catalyst characterization, these catalysts would be tested for CO<sub>2</sub> hydrogenation.

<u>Subtask 4.2 – Experimental evaluation of physical mixtures of catalysts:</u> Based on the performance of the catalytic combinations in Subtask 4.1, the catalysts will be assessed for their CO selectivity, as CO is the main side-product of the methanol synthesis catalyst. Then one catalyst will be selected for this subtask and future subtasks. Two synthesized and characterized ZSM-5 catalysts with low and high acidity will be physically mixed with each other for the chosen metallic catalysts and tested for their performance. The catalysts will be evaluated by steady-state conversion testing, measuring rates, and selectivity.

<u>Subtask 4.3 – Experimental evaluation of impact of CO<sub>2</sub>/H<sub>2</sub> ratio:</u> The C/H ratio is a critical variable likely to affect the catalytic performance. Steady-state conversion testing, measuring rates, and selectivity as a function of CO<sub>2</sub>/H<sub>2</sub> ratio will be conducted to assess this factor.

# B. Background and Experimental Methods

<u>Subtask 4.1 - Experimental evaluation of "control" catalysts:</u> The metal catalyst that has been used for initial CO<sub>2</sub> conversion will be the Cu/Zn/Al mixture. This catalyst has been chosen as the most active and promising transition metal (TM)/alumina combination according to the paper review performed on CO<sub>2</sub> conversion to hydrocarbons.<sup>5</sup> Initial studies will be done using the ordered Riogen commercial methanol synthesis catalyst available on their website.

Along with the studies on this commercial catalyst, an in-house catalyst will also be synthesized according to the guidelines available on the literature for this catalyst. 10–12 The following steps will describe the procedure that will be taken for catalyst preparation:

- 1. Pumping a solution of metal nitrates [(Cu(NO<sub>3</sub>)<sub>2</sub> (0.6 mol/L), Zn(NO<sub>3</sub>)<sub>2</sub> (0.3 mol/L), Al(NO<sub>3</sub>)<sub>3</sub> (0.1 mol/L))] and adding a solution of Na<sub>2</sub>CO<sub>3</sub> (1 mol/L) as a precipitant (at constant flow rate of 5 ml/min) into a stirred and heated glass reactor with a starting volume of 200 ml of demineralized water.
- 2. Maintaining the temperature of 70 °C during the precipitation process.
- 3. Continuously pumping the sodium carbonate solution to the metal nitrate and demineralized water solution to maintain a constant pH of 6 (±0.1 unit).
- 4. Stopping the co-precipitation after adding 40 mL of metal nitrate solution.

- 5. Keeping the pH constant during the aging process through the controlled addition of metal nitrate or sodium carbonate solution.
- 6. Aging the solution for 1 h.
- 7. Filtering the precipitates.
- 8. Washing the precipitates three times with 150 mL of demineralized water each time.
- 9. Drying the precipitates overnight at 80°C.
- 10. Grinding the mixture.
- 11. Calcining the resulting 200–500 mg of the dried hydroxycarbonate precursor at 300 °C under air for 3 h (heating ramp 2°C/min), resulting in the oxide precursor.

The catalyst will be prepared according to the mentioned steps as the control-experiments with the commercial catalysts are started. Initial surface characterization studies by nitrogen adsorption (BET), Scanning electron microscopy and energy dispersive X-ray spectroscopy (SEM/EDS), H<sub>2</sub>/CO<sub>2</sub>/NH<sub>3</sub> Temperature-programmed desorptions (TPDs) will be conducted on the fresh and used catalysts to obtain baseline information for further analysis.

<u>Subtask 4.2 – Experimental evaluation of physical mixtures of catalysts:</u> Primary surface characterization studies that are targeted for the different commercial and in-house catalysts are SEM/EDS, X-ray diffraction (XRD), X-ray photoelectron spectroscopy (XPS), and N<sub>2</sub> porosity measurements. These studies are favored since they can help the most in justifying the experimental observations by giving information regarding the surface elemental composition, structure, topology, morphology, and porosity of the catalysts.

<u>Subtask 4.3 – Experimental evaluation of impact of CO<sub>2</sub>/H<sub>2</sub> ratio:</u> Recently published studies have shown that upon increasing the H<sub>2</sub>/CO<sub>2</sub> ratio, the selectivity toward CO decreases and CO<sub>2</sub> conversion and the selectivity toward paraffins increases. As a result, while the selectivity toward aromatics in none of these studies showed any significant improvement, the rate of aromatics production slightly improves.<sup>7,13,14</sup> The H<sub>2</sub>/CO<sub>2</sub> ratio of 1 to 6 will be tested.

#### C. Results and Discussion

<u>Subtask 4.1 - Experimental evaluation of "control" catalysts:</u> The activities in this subtask involved performing experiments on a commercial Cu/Zn/Al<sub>2</sub>O<sub>3</sub> catalyst to assess its behavior in the CO<sub>2</sub> to methanol reaction at different operational conditions. Prior to the catalytic experiments, several characterization studies were performed to better understand the nature of the catalyst (BET, TPR, XRD, SEM/EDS). The catalyst had a surface area of 85 m<sup>2</sup>/g and pore size of 9 nm, with the best reducibility performance in the range of 100 °C- 200 °C. The chemical composition of the catalyst was found to be 63% Cu, 26% Zn, and 11% Al, all being at their oxide phase on the surface of the catalyst at room temperature. Batches of lab-made catalyst with similar composition and surface

characterizations were synthesized after deciding to continue experiments using this catalytic mixture.

The parameters studied in this task were the temperature of the reaction, pressure of the reaction, and feed weight hourly speed velocity (WHSV). All the experiments were done using the hydrogen-added flue gas mixture, 11% CO<sub>2</sub>, 33% H<sub>2</sub>, and 56% N<sub>2</sub>. The molar concentrations and selectivities that will be discussed through this report were all confirmed through preparing standard mixtures of each chemical at different concentrations.

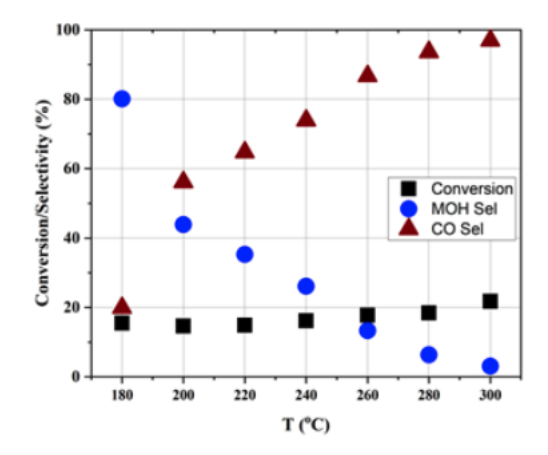


Figure 4: The performance of commercial Cu/Zn/Al catalyst at different temperatures. Other reaction parameters are: P=600 psi, WHSV=6000 ml/gcat/h, catalyst mass=0.4g, H<sub>2</sub>/CO<sub>2</sub>=3

The temperature of the reaction was varied between 180 °C and 300 °C, with step size of 20 °C. The conversion and products selectivity results are shown in Figure 4. As can be seen, the conversion of the reaction stays in the range of 15-20% for the studied range, which is due to the opposing thermochemistry behavior of the two main reactions in this system. Reaction 1, the RWGS reaction producing CO, is endothermic and is favored at higher temperatures, while reaction 2, the methanol production reaction, is exothermic and operates at a higher rate at lower temperatures. The best methanol production performance is observed at the lowest studied temperature with the rate of 3.8 mmol MOH/g cat/h. However, since the ZSM-5 catalyst, which is important in the second step (conversion of methanol to aromatics) is mostly activated at higher temperatures (300-400 °C), 15,16 other reaction parameters (P and WHSV) were studied at the temperature of 280 °C. At this temperature and using the reaction parameters mentioned in Figure 4, the rate of methanol production is 0.4 mmol/g cat/h. The temperature of 300 °C was not chosen for investigating other parameters, since methanol selectivity was too low at this temperature for a good comparison.

To further understand the behavior of this catalyst, a thermodynamic equilibrium analysis was conducted at the same temperature range and pressure as experimental analysis. The results are shown in Figure 5. There is a strong agreement between the thermodynamic equilibrium results and reaction products' composition at different conditions, especially at higher temperatures. This shows that the thermodynamic behavior of the CO<sub>2</sub>-CO-methanol mixture is the determining step of the reaction at the

studied conditions. Higher flow rates (WHSV) may need to be employed to have the reaction kinetics as the rate-determining step.

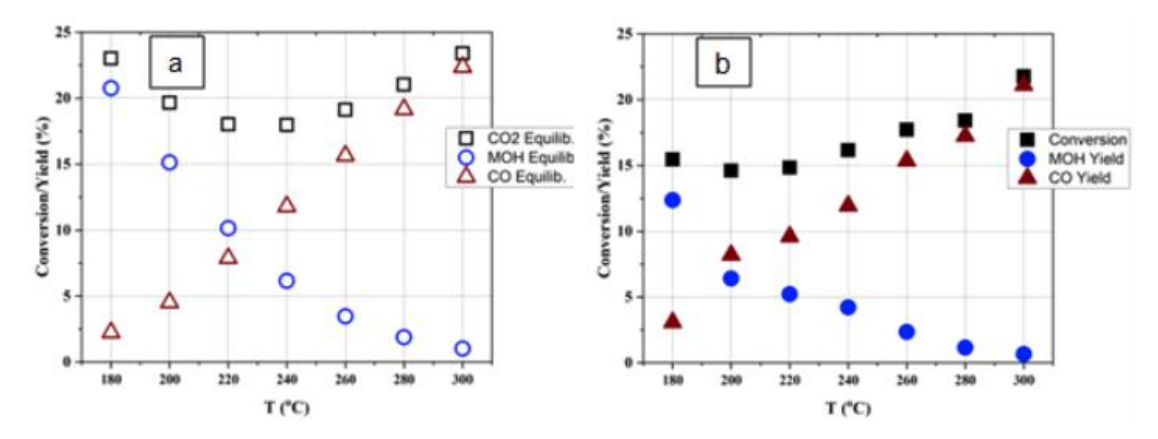


Figure 5: Comparison of CO<sub>2</sub> conversion reaction kinetics and the thermodynamics of the CO<sub>2</sub>-CO-methanol at different temperatures. (a) Composition of the three chemicals at thermodynamic equilibrium, (b) Experimental results obtained

The studies on the behavior of the reaction at different space velocities are shown in Figure 6. First, the WHSV was changed in the range of 3000-66000 mL/g cat/h; however, no significant change in the behavior of the reaction was observed. This was because the reaction approached thermodynamic equilibrium at this space velocity range. Upon going to WHSVs beyond 70,000 mL/gcat/h, a decreasing trend in CO2 conversion and CO selectivity, and an increasing trend in methanol selectivity was observed. At these WHSVs, the kinetics start to become the selectivity-determining steps. The selectivity of methanol can increase from 7% to 30% at WHSV of 250,000 mL/gcat/h. However, this range of space velocities is not of interest for future studies due to design limitations, such as the need for a larger preheating chamber reactor size, on the lab scale, and which may be economically unfavored upon scaling-up the process. It is worthwhile to note that for higher ranges of WHSV, instead of increasing the feed flow rate, the catalyst loading was reduced. This was done to ensure that the feed gas spends enough time in the preheating zone to reach the setpoint temperature before getting to the reaction zone.

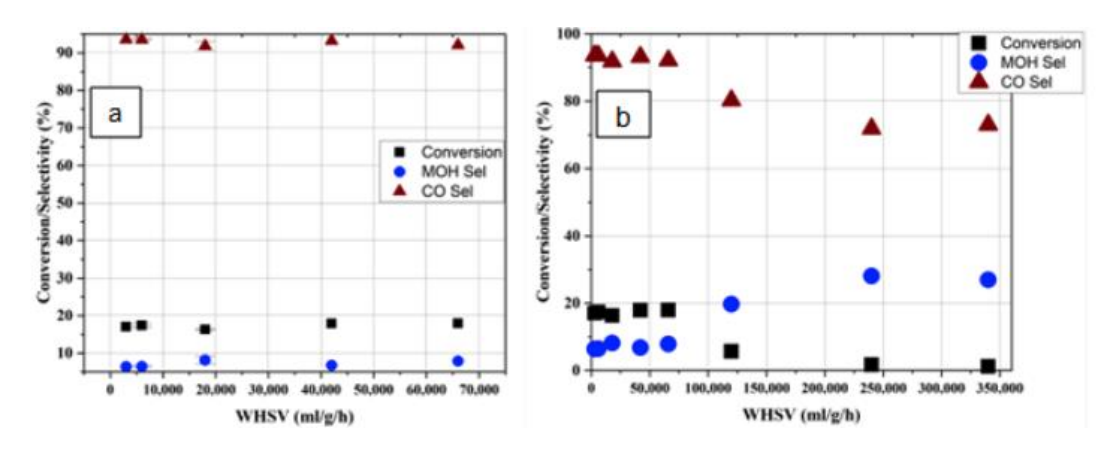


Figure 6: The performance of commercial Cu/Zn/Al catalyst at different speed velocities. Other reaction parameters are: T=280 °C, P=600 psi, catalyst mass=0.4 g, H<sub>2</sub>/CO<sub>2</sub>=3

The catalytic performance at different reaction pressures is shown in Figure 7. According to the Le Chatelier's principle, it is expected that higher methanol production rates are achieved at higher reaction pressures. This was confirmed by the experimental results as the best performance for methanol production was observed at the highest studied pressure, 1500 psi. At this pressure, the methanol production rate was as high as 1.6 mmol/g cat/h.

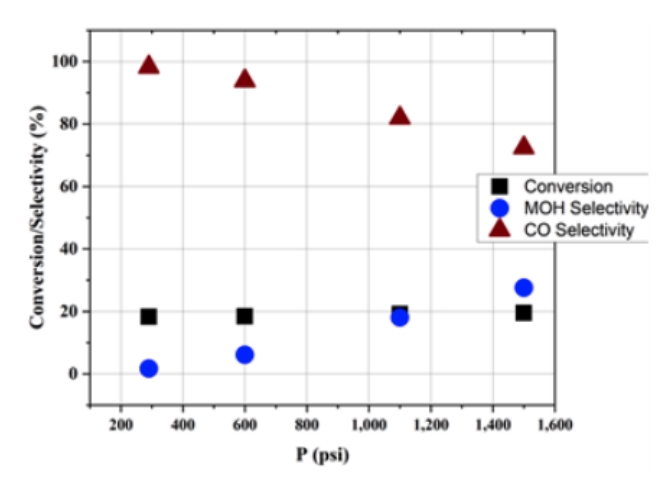


Figure 7: The performance of commercial Cu/Zn/Al catalyst at different pressures. Other reaction parameters are: T= 280 °C, WHSV= 6000 ml/gcat/h, catalyst mass= 0.4 g, H<sub>2</sub>/CO<sub>2</sub>= 3

Overall, different reaction parameters were studied during this subtask to understand the behavior of the first step of the reaction (CO<sub>2</sub> to methanol) using the commercial Cu/Zn/Al catalyst. The results show that the active temperature range for methanol production is below 200 °C, while the second step is expected to be most active at the range of >300 °C. At temperatures above 300 °C, CO is the major product in the system. Increasing the space velocity improves the methanol production rate since CO is a thermodynamically more stable chemical compared to methanol, and thermodynamics is the selectivity-determining step at lower WHSVs. Higher pressures are desired for methanol production, as supported by the Le Chatelier's principle.

Besides the Cu/Zn/Al catalyst, the catalytic behavior of the ZSM-5 catalyst was studied at selected reaction conditions. Studies were performed in the temperature range of 280 °C- 340 °C, and showed negligible CO<sub>2</sub> conversion at all temperatures.

The other metallic catalyst that was proposed for the CO<sub>2</sub> aromatization project was a Co/Al<sub>2</sub>O<sub>3</sub> catalyst. Cobalt was suggested as a catalyst with the potential of producing aromatics from CO<sub>2</sub> with olefins as intermediate products. However, a review of the paper recently published showed that cobalt, as the only metal involved, does not effectively follow this pathway, therefore it cannot produce aromatics from CO<sub>2</sub> under our proposed conditions. Instead, methane is the major product upon feeding CO<sub>2</sub> with cobalt as the catalyst. One strategy that can be obtained to produce olefins using a cobalt catalyst is by integrating this metal with a zeolite with a larger cage size compared to ZSM-5. The most common zeolite used for this purpose is SAPO-34. However, the challenge with using Co/SAPO-34 mixture for olefins production in our project is that SAPO-34 can compete with ZSM-5 for converting CO<sub>2</sub> to undesired products instead of aromatics.

Due to the reasons mentioned above, we decided not to pursue the cobalt catalyst for the rest of the tasks in this quarter, as literature suggests it will not produce enough long chain hydrocarbons to give aromatic products after combination with zeolite ZSM-5.

Next, we tested a ZnO-ZrO<sub>2</sub> (ZnZrO) catalyst that was synthesized in-house. The synthesis was based on the co-precipitation method used by Wang et al.<sup>19</sup> Typically, Zn(NO<sub>3</sub>)<sub>2</sub>·6H<sub>2</sub>O and Zr(NO<sub>3</sub>)<sub>4</sub>·5H<sub>2</sub>O with a fixed molar ratio (1/6 for this study) were dissolved in 100 mL deionized water. Then 3.06 g of (NH<sub>4</sub>)<sub>2</sub>CO<sub>3</sub> was dissolved in 100 mL deionized water as precipitant, and added dropwise to the mixed solution under vigorous stirring at 70°C. The white suspension was aged for 2 hours at 70 °C. After cooling to the room temperature, the solid product was recovered by filtration, washed with deionized water, and dried overnight at 80 °C. The ZnZrO was obtained after calcination at 500 °C for 5 h.

For the catalyst characterization, powder X-ray diffraction (XRD) patterns were recorded at room temperature on a PANalytical X'Pert PRO Alpha-1 diffractometer using Cu Kα radiation in the 2θ range from 5° to 90°. As shown in Figure 8, the XRD pattern of ZnZrO (Zn/Zr molar ratio of 1/6) is ascribed to the tetragonal ZrO<sub>2</sub> phase and no diffraction peaks belonging to ZnO were observed, which indicated that the doped ZnO was highly dispersed into the lattice of tetragonal ZrO<sub>2</sub> or was amorphous. Also, this XRD pattern coincided well with the previous literature reports.<sup>19,20</sup>

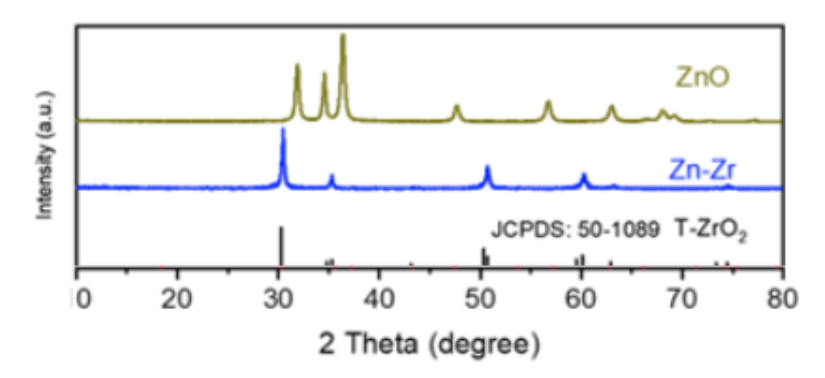


Figure 8: XRD pattern of ZnZrO (1/6 Zn/Zr molar ratio), commercial ZnO, and tetragonal ZrO<sub>2</sub>

Reaction studies were done at three temperatures relevant to the second step of the  $CO_2$  aromatization reaction (methanol conversion to aromatics). The trends obtained in this study were quite similar to those obtained in the previous quarter (as reported in Q5 report). The obtained products from this reaction were primarily CO and methanol, with minimal amounts of ethanol. The results of Figure 9.A indicate that an increase in reaction temperature would improve the catalytic activity for  $CO_2$  conversion; however, CO becomes the primary product at higher temperatures. Also, three different WHSVs were studied at the middle temperature (320 °C) to understand the effect of the feed flow rate on the catalyst activity. Results in Figure 9.B indicate that higher WHSVs improve the methanol selectivity. On the other hand, the  $CO_2$  conversion decreases from 17% to 9%, as the WHSV increases.

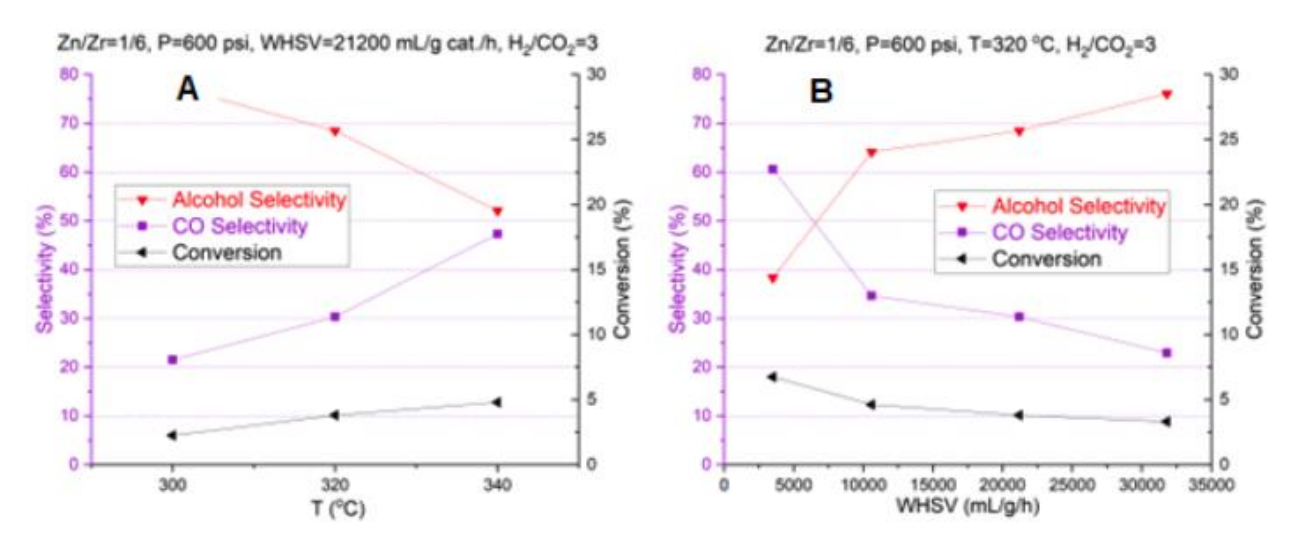


Figure 9: Experimental studies over the ZnZrO catalyst. (A) temperature, and (B) WHSV study

Among the different conditions explored using the ZnZrO<sub>x</sub> catalyst, the best methanol production rate was observed at the temperature of 320 °C, pressure of 600 psi, and WHSV of 32,000 mL/g catalyst/h with a methanol production rate of 4.3 mmol CO<sub>2</sub>/g catalyst/h. This rate is comparable to the one reported in some previous reports<sup>19</sup> and smaller than those reported in some other studies with the same metal oxide catalyst.<sup>21</sup>

ZnGa was also considered as the catalyst. The ZnGa oxide with Zn/Ga molar ratio of 1:2 was synthesized by a co-precipitation method.<sup>22</sup> First, 2.97 g of Zn(NO<sub>3</sub>)<sub>2</sub>·6H<sub>2</sub>O and 5.10 g of Ga(NO<sub>3</sub>)<sub>3</sub>·xH<sub>2</sub>O (M = 255.5 g mol<sup>-1</sup>) were dissolved in 100 mL of deionized water under vigorous stirring. Then, the precipitant of 25 wt% aqueous ammonia solution was added dropwise into the mixed solution at room temperature until the pH approaching 7. The white suspension was then aged for 2 hours at 70 °C. After cooling down to the room temperature, the solid products were recovered by filtration, washed with deionized water, and dried overnight at 80 °C. The Zn-Ga oxide was obtained after calcination at 500 °C for 5 h. XRD studies shows that the ZnGa oxide catalyst have a spinal structure (Figure 10), an observation that is consistent with the literature.<sup>22</sup>

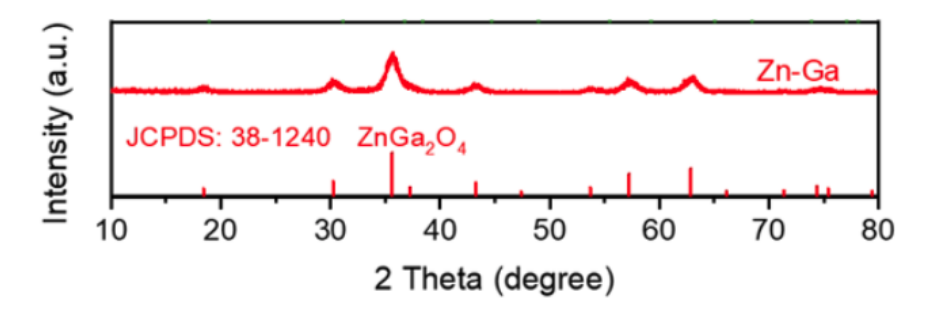


Figure 10: XRD pattern of ZnGa oxide catalyst

The experiments with the synthesized ZnGaO catalyst at different temperature were conducted at three different temperatures and three different WHSVs. The results are shown in Figure 11. Carbon monoxide and methanol are the only products of the reaction using this catalyst. It can be observed that upon increasing the reaction temperature the catalytic activity for CO<sub>2</sub> conversion improves (Figure 11.a); however, CO becomes the predominant product at higher temperatures, where its selectivity exceeds 90% at temperatures beyond 350 °C. Also, three different WHSVs were studied at the middle temperature (350 °C) to understand the effect of the feed flow rate on the catalyst activity. Results in Figure 11.b indicate that higher WHSVs improve the methanol selectivity. On the other hand, the CO<sub>2</sub> conversion decreases from 21% to 9% as WHSV increases, which is evidence that CO<sub>2</sub> conversion is not as sensitive to WHSV as products' selectivities are.

In summary, the performance of the  $ZnGa_2O_4$  catalyst is not as good as the ZnZrO catalyst that was discussed earlier. Among the temperatures explored using the  $ZnGa_2O_4$  catalyst at 21000 mL/g catalyst/h and 600 psi, the best methanol production rate was observed at a temperature of 320 °C, with a methanol production rate of 1.9 mmol/g catalyst/h. The methanol selectivity in none of the cases exceeded 31%, this value is about 15% lower than the maximum selectivity reported for the ZnZrO catalyst, an indication that the ZnZrO catalyst contains more ideal sites for the conversion of  $CO_2$  to methanol.

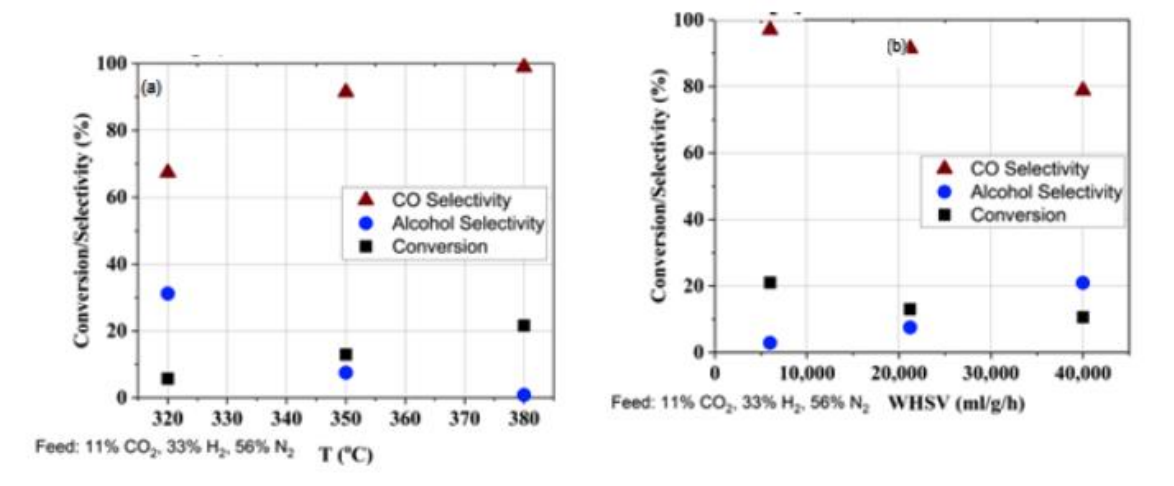


Figure 11: Performance of ZnGa<sub>2</sub>O<sub>4</sub> catalyst at (a) different temperatures, and (b) weight hourly space velocities

Subtask 4.2 – Synthesis, characterization, reactor testing of physical mixtures: The most common range of Si/Al ratio in zeolite catalysts used in the literature for the methanol conversion to aromatics is 20-40.<sup>15,23</sup> This number for the CO<sub>2</sub> aromatization studies varies in an extensively wider range (12-800), although the general consensus is that higher Si/Al ratios (lower acidity) contribute to higher aromatics selectivity, the selectivity of the products of interest remains within the same order of magnitude in different studies.<sup>5,13</sup> Therefore, we started the initial physical mixture studies using the commercial ZSM-5 catalyst with Si/Al ratio of 40 (CBV 8014, Zeolyst) which was available in large scale. Upon achieving an acceptable range of aromatics selectivity, we will study the effect of higher Si/Al ratio using our lab-made ZSM-5 catalysts that are synthesized as described in Subtask 6.1.

For the preparation of the catalyst mixtures, powders of the commercial Cu/Zn/Al and ZSM-5 catalysts were mixed with the ratio of 1/2 (Cu-Zn-Al / ZSM-5), pelletized, and then sieved to the mesh size of 40-120, as suggested in the literature. 19,24,25 Initial experiments were done at the WHSV of 6000 mL/g cat/h (equivalent of 18000 mL/g cat/h for the Cu/Zn/Al catalyst) and a pressure of 600 psi at three temperatures (280 °C, 310 °C, and 340 °C). Although the ZSM-5 catalyst is reported to be mainly active at temperatures beyond 300 °C, for the comparison of the metal catalyst and physically mixed catalyst results, the temperature of 280 °C was chosen as this was the reference temperature that has shown some methanol production activity in the metal (Cu) studies.

Results of the physical mixture catalyst studies at different temperatures are shown in Figure 12. The results indicate that CO is the primary product at all temperatures, CO selectivity increases at higher temperatures. The methanol selectivity is very similar to its value in the separate metal catalyst studies; furthermore, the sum of the selectivity of alkanes/alkenes (mostly C2 and C5) and CO is equal to the selectivity of CO in Cu/Zn/Al experiments. This suggests that alkanes and alkenes might be produced from the conversion of CO, and CO plays the role of an intermediate product in this reaction.

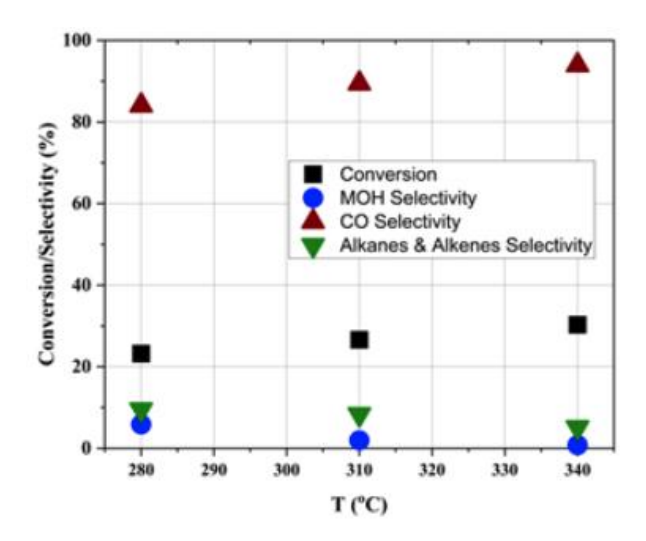


Figure 12: The performance of Cu-Zn-Al/ZSM-5 catalyst at different temperatures. Other reaction parameters are: P= 600 psi, WHSV= 6000 ml/g<sub>cat</sub>/h, catalyst mass= 0.3 g, H<sub>2</sub>/CO<sub>2</sub>= 3, metal/ZSM-5 mass ratio = ½

The selectivity toward aromatics in all the above experiments was below 0.3% with a decreasing trend as the temperature increased. This low selectivity agrees with the recently published studies that have used the same catalyst at selected conditions. The low selectivity of aromatics for the copper catalyst could be attributed to its higher M-H bond dissociation energy (280 kcal/mol) compared to the metals that have shown higher aromatics selectivity (86 for Zn-H and >270 for Ga-H). This higher M-H dissociation energy is suspected to be more favored for the formation of side products such as CO and paraffins. Besides, metal oxides generally have shown better catalytic performance for aromatics selectivity since they provide heterolytic hydrogen cleavage (as opposed to homolytic cleavage for M-H bonds) and their oxygen vacancy sites absorb oxygen-containing chemicals such as CO<sub>2</sub> and CO more effectively. Selectively 1.25

The metal oxide catalysts are responsible for the production of methanol intermediate in the CO<sub>2</sub> aromatization reaction. The results of the ZnZr oxide catalyst for CO<sub>2</sub> to methanol reaction showed a better methanol selectivity performance for this metal oxide combination compared to the ZnGa oxide catalyst. This agrees with the literature review on the superior methanol synthesis performance of ZnZr oxide catalyst compared to the ZnGa oxide catalyst.<sup>20</sup> Therefore, the ZnZr oxide catalyst was chosen for this subtask and future subtasks. The synthesis of this catalyst was based on the co-precipitation method used by Wang et al. Typically, Zn(NO<sub>3</sub>)<sub>2</sub>·6H<sub>2</sub>O and Zr(NO<sub>3</sub>)<sub>4</sub>·5H<sub>2</sub>O with a fixed molar ratio (1/6 for this study) were dissolved in 100 mL of deionized water. Then 3.06 g of (NH<sub>4</sub>)<sub>2</sub>CO<sub>3</sub> was dissolved in 100 mL deionized water as a precipitant and added dropwise to the mixed solution under vigorous stirring at 70°C. The white suspension was aged for 2 hours at 70 °C. After cooling to the temperature, the solid product was recovered by filtration, washed with deionized water, and dried overnight at 80 °C. The ZnZrO was obtained after calcination at 500 °C for 5 h.

As mentioned in the previous sections, prior studies have shown the importance of controlling the Zn/Zr ratio on the methanol selectivity and have considered the optimum value of this ratio to be between 1/6-1/8. Experiments in the previous quarter were done with a catalyst that utilized an old sample of Zr(NO<sub>3</sub>)<sub>4</sub>·5H<sub>2</sub>O, therefore it was reasonable to expect that this chemical has adsorbed water and other adsorbing species over time. A new batch of this chemical was ordered during this quarter for the purpose of synthesizing new ZnZr oxide catalysts for the CO<sub>2</sub> aromatization reaction. Methanol synthesis experiments will be repeated in the future to confirm the previous behavior of this metal oxide catalyst at different temperatures and WHSVs.

It is widely accepted that strong acid sites in H-ZSM-5 catalysts are the active site for the aromatization reactions. To investigate the effect of the strength of acid sites on the catalytic performance of CO<sub>2</sub> to aromatics, the ZSM-5 with different Si/Al ratios were synthesized. The H-ZSM-5 was synthesized using the hydrothermal method. The starting molar ratio of the chemicals for the synthesis was 1.0 SiO<sub>2</sub>/0.45 TPAOH/x Al<sub>2</sub>O<sub>3</sub>/50 H<sub>2</sub>O/0.1 L-lysine, with x being 0.0125, 0.01, and 0.0083 for different acidities desired. First, TPAOH was mixed with deionized water; after 10 min of vigorous stirring, TEOS was added into the mixture. Then NaAlO<sub>2</sub> was added until TEOS was completely hydrolyzed. Next, the gel mixture was transferred into a teflon-lined stainless steel autoclave for crystallization under 170 °C for 3 days, or 80 °C for 2 days and 170 °C for 1 day. The as-synthesized solid products were centrifuged, washed with water and ethanol several times, and dried at 80 °C overnight, followed by calcination at 550 °C for 6 h. The Na-form zeolite was further exchanged with the aqueous solution of NH<sub>4</sub>NO<sub>3</sub> (1.0 M) two times at 80 °C for 4 h to obtain the H-form ZSM-5 (H-ZSM-5).

Characterization studies were performed to better understand the structure of each catalyst. For comparison, the commercial ZSM-5 catalyst with Si/Al ratio of 40 (CBV 8014 Zeolyst, labeled as CZSM-5-40 in this report), was used as the standard for the characterizations. Powder X-ray diffraction (XRD) patterns were recorded at room temperature on a PANalytical XPert PRO Alpha-1 diffractometer using Cu Ka radiation in the 20 range from 5° to 90°. Scanning electron micrograph (SEM) images were obtained using a Hitachi SU8010 SEM microscope operating at 1 kV without a metal coating. The nitrogen physisorption isotherms were measured with a Tristar II 3020 (Micromeritics) at 77 K. CO<sub>2</sub> or NH<sub>3</sub> temperature-programmed desorption (TPD) measurements were conducted on the AutoChem II automated chemisorption analyzer equipped with a thermal conductivity detector (TCD). For CO<sub>2</sub>-TPD, typically, 100 mg of sample was pretreated in H<sub>2</sub> stream at 400 °C for 1 h. Then, the gas flow was switched to He for 30 min to clean its surface and the sample was cooled to 50 °C. It was then switched to the CO<sub>2</sub> stream for 60 min, and afterward, the sample was flushed by the He stream until a stable baseline was obtained. The temperature was then ramped from 50 °C to 800 °C at 10 °C/min and the desorbed CO<sub>2</sub> was measured using a TCD detector. For NH3-TPD, 50 mg of sample was pretreated in He at 400 °C for 1 h and the sample was then cooled to 100 °C. It was then switched to the NH<sub>3</sub>-He mixture (10 vol% NH<sub>3</sub>) stream for 60 min; the sample was flushed by He stream until a stable baseline was obtained. The temperature

was then ramped from 50 °C to 800 °C at 10 °C/min and the desorbed NH $_3$  was detected using the TCD.

The XRD pattern of the synthesized and commercial zeolites (Figure 13) shows that all samples have signature peaks of the MFI zeolite. However, SEM images show that the particle sizes distribution of ZSM-5-40 and ZSM-5-20 are broader than that of the high Si/AI ratio samples, and their morphology is irregular compared to the other synthesized zeolites (Figure 14). This is due to the high AI content in those zeolites that causes adverse effects on the morphology of the MFI structure. For the investigation of the effect of Si/AI ratios of ZSM-5 on CO<sub>2</sub> aromatization reaction, the other factors like morphology and particle size needs to be controlled. To address this issue, we will enlarge the ratio of H<sub>2</sub>O/SiO<sub>2</sub> in the synthesis recipe from 50 to 150. A more diluted beginning gel mixture can obstruct the detrimental effect of high content of AI when the Si/AI ratio is low; however, it can undesirably increase the longevity of the stirring process.

The  $N_2$  physisorption isotherms and detailed porosity data are also shown in Figure 15 and Table 2. The porosity of the synthesized ZSM-5 is like that of commercial ZSM-5. Overall, the XRD patterns and  $N_2$  physisorption isotherms indicate a good similarity between the crystallinity of the synthesized ZSM-5 and the commercial catalyst. It is worth mentioning that the sample recoveries for the synthesized zeolites were in good agreement with the theoretical weight expected (yields of all the three samples were above 85% as seen in Table 1).

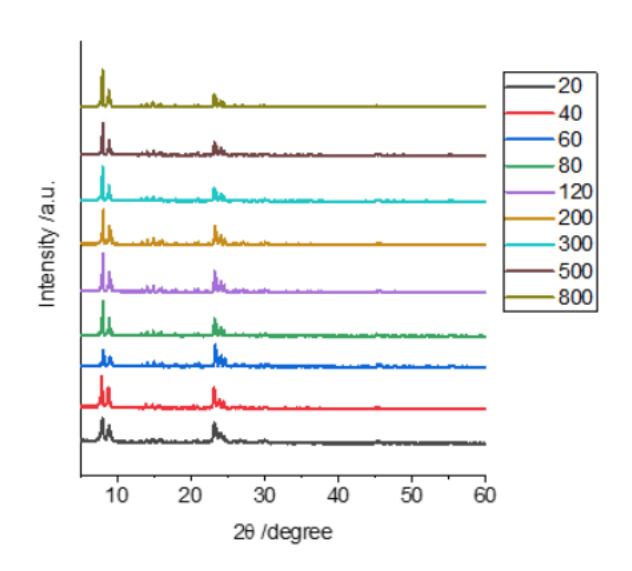


Figure 13: XRD patterns of synthesis of different Si/Al ratios of ZSM-5

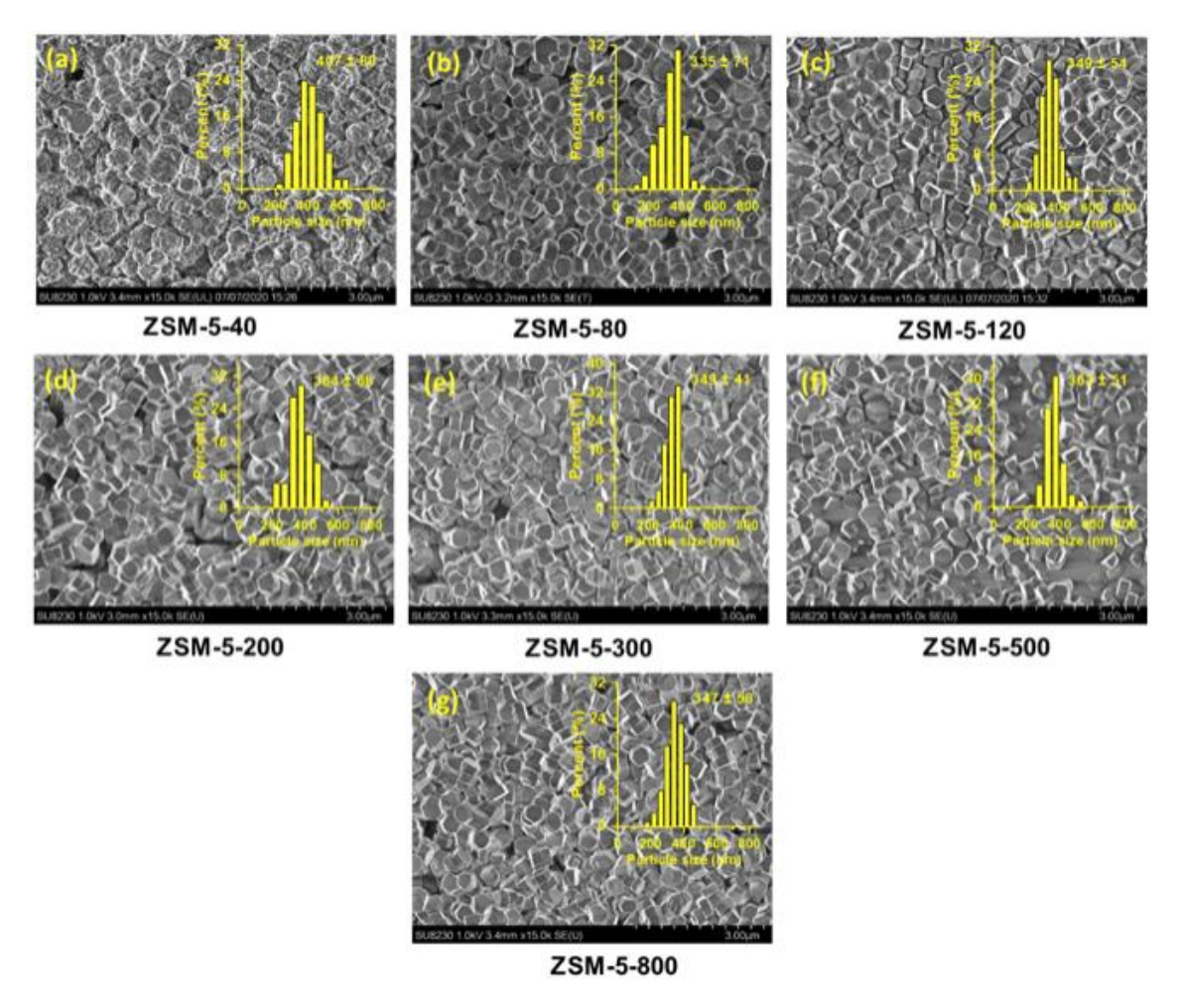


Figure 14: SEM images of (a) ZSM-5-40, (b) ZSM-5-80, (c) ZSM-5-120, (d) ZSM-5-200 and (e) ZSM-5-300, (f) ZSM-5-500 and (g) ZSM-5-800

Table 1: Porosity and Product yield of commercial ZSM-5 and synthesized zeolite

Si/Al	$S_{BET^b}$	Smicro	S <sub>ext</sub>	$V_{\text{total}}^{c}$	$V_{ m micro}{}^{ m d}$	$V_{\rm meso}^{\rm e}$	Yield <sup>f</sup> (%)
	$(m^2 g^{-1})$	$(m^2 g^{-1})$	$(m^2 g^{-1})$	(cm³ g-1)	(cm³ g-1)	(cm³ g-1)	
C-40a	371	264	107	0.21	0.13	80.0	-
60	343	284	59	0.18	0.12	0.06	89%
80	327	224	103	0.21	0.13	0.08	86%
100	381	216	165	0.19	0.10	0.09	90%
120	359	268	91	0.17	0.13	0.04	92%

<sup>&</sup>lt;sup>a</sup> C-40 denotes commercial ZSM-5-40.

<sup>&</sup>lt;sup>b</sup> the Determined by BET method.

 $<sup>^{\</sup>circ}$  Determined by the adsorbed volume at P/P<sub>0</sub> = 0.97.

<sup>&</sup>lt;sup>d</sup> Determined by t-plot method.

<sup>&</sup>lt;sup>e</sup> Determined by V<sub>total</sub>-V<sub>micro</sub>.

Yield = w1/w2, where w1 and w2 are the weight of the calcined sample and the theoretical zeolite sample, respectively

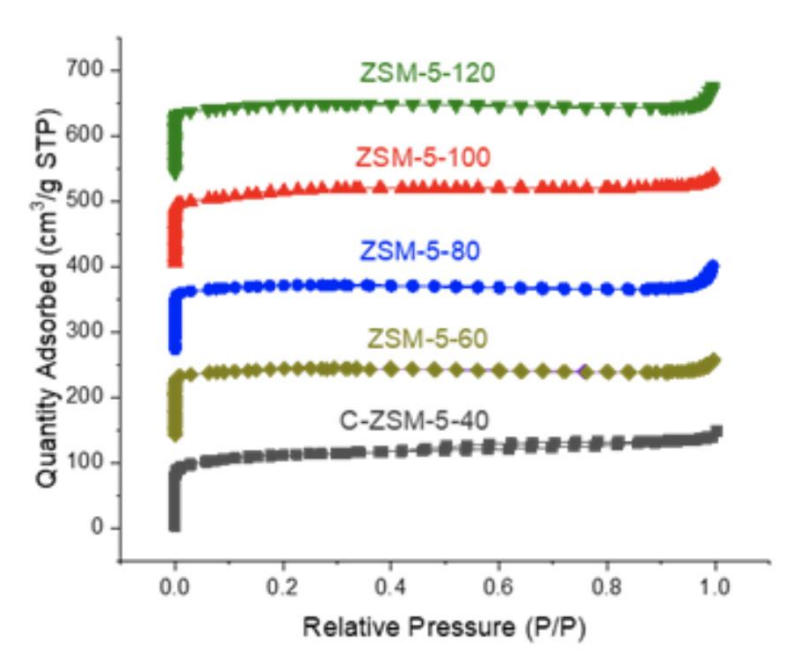


Figure 15: N<sub>2</sub> physisorption isotherms of commercial ZSM-5 and synthesized ZSM-5

NH<sub>3</sub>-TPD measurement was adopted to quantify the density of acid sites of H-ZSM-5 (Figure 16). For all the samples, two NH<sub>3</sub> desorption peaks were observed. Generally, the lower-temperature peak and the higher-temperature are ascribed to desorption of NH<sub>3</sub> adsorbed on the weak and strong acid sites, respectively. The density of each of these acid sites are quantified from the intensity of their relevant peak. It was found that the density of strong acid sites, that are active at relevant reaction temperatures, increase with the decrease in the Si/Al ratios. The density of strong acid sites of H-ZSM-5-60 is about 121  $\mu$ mol g<sup>-1</sup>, which is larger by a factor of two compared to the H-ZSM-5-120 (61  $\mu$ mol g<sup>-1</sup>).

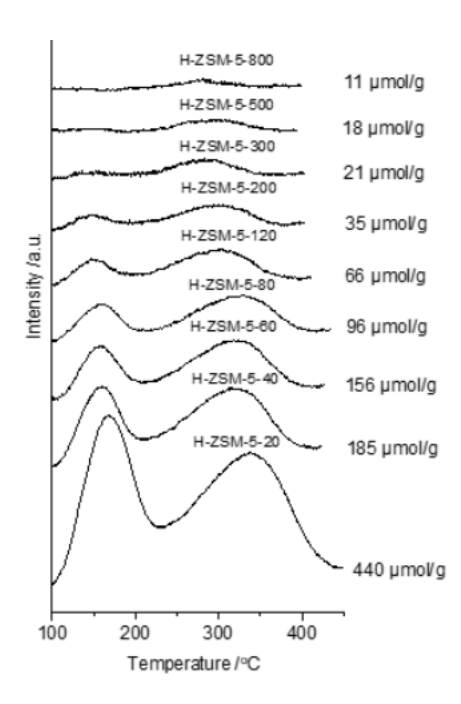


Figure 16: NH<sub>3</sub>-TPD profiles for the different Si/Al ratios of synthesized H-ZSM-5. The density of strong acid sites quantified from the intensity of higher-temperature peak were showed in the figure

Initial experiments with ZnZrO/H-ZSM-5 bifunctional catalysts were started with the H-ZSM-5 catalyst with the Si/Al ratio of 80. It is worth noting that all the experiments in this subtask are reported with the ZnZrO as the metal oxide catalyst with Zn/Zr ratio of 1/6, and the H-ZSM-5 as the zeolite with the crystal size of 300 nm. The first value is within the optimum range of within the metal oxide for catalyzing the CO<sub>2</sub> to methanol reaction, <sup>19,20,25</sup> and the second one will be studied and optimized during the future tasks. Since the H-ZSM-5 catalysts in this project contain various Si/Al ratios and crystal sizes, we show each H-ZSM-5 catalyst in the format of H-ZSM-5-xxx-yyy, where xxx represents the Si/Al ratio, and yyy is the crystal size in nm.

Figure 17 shows the behavior of the CO<sub>2</sub> aromatization reaction over ZnZrO/H-ZSM-5-80-300 catalyst under different operational conditions. Figure 17A shows the catalytic performance in the temperature range of 300 °C- 360 °C. Since the RWGS reaction is an endothermic reaction, CO selectivity increases at higher temperatures, and becomes the primary side-product of this reaction. Paraffins are the other major side-product, which also show enhanced selectivity at higher temperatures. Therefore, the aromatization reaction becomes more favorable at the lower temperature ranges (300-320 °C) for two reasons: (i) lower RWGS reaction rate, and (ii) slower conversion of intermediate olefins to paraffins via hydrogenation. On the other hand, since the CO<sub>2</sub> conversion reduces to the range of below 5% at 300 °C, the 320 °C seems to be the ideal temperature for this reaction. Figure 17B shows the reaction performance at different WHSVs. As expected, conversion decreases upon increasing the WHSV. The aromatics selectivity is not significantly affected upon going to WHSVs beyond 1,500 mL/gcat/h. However, the fact that upon increasing the WHSVs to 7,000 mL/gcat/h, the shifts the selectivity towards intermediate olefins and (partially intermediate) C<sub>6+</sub> chemicals increase, provides further

motivates interest to in this range of WHSVs. Upon going to WHSVs beyond 7,200 mL/ $g_{cat}$ /h, the aromatics selectivity slightly decreases and the increase in selectivity for olefins and C<sub>6+</sub> chemicals becomes slower. Therefore, the 7,200 mL/ $g_{cat}$ /h seems to be within the range of optimum feed velocities for this catalyst and reactor.

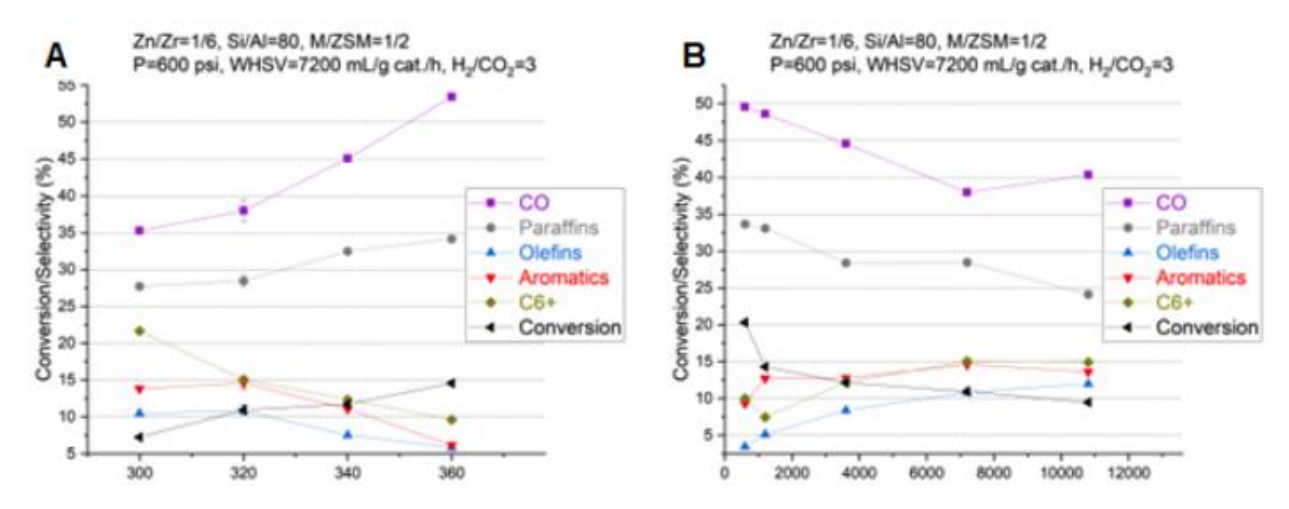


Figure 17: Experimental studies over the ZnZrO/H-ZSM-5-80-300 catalyst, (A) temperature, and (B) WHSV

Based on the above discussions, we decided to continue the rest of the experiments at the temperature of 320 °C and WHSV of 7,200 mL/g<sub>cat</sub>/h. It is worthwhile noting that the experiments with the catalyst used in Figure 17 with the mentioned optimum conditions were repeated 5 times via different runs using the same batch of catalyst and with two separately synthesized batches of catalyst to assure the reproducibility of the results. The error bars at the temperature of 320 °C in Figure 17A are displayed to show the extent of reproducibility of the runs.

Using the catalysts described earlier in this subtask, containing the same crystal size and different acid site densities, we studied the effect of Si/Al ratio on the catalytic performance at the temperature of 320 °C, WHSV of 7200, and the pressure of 600 psi (Figure 18). As it can be seen, very low acidities are favored for aromatics production; the Si/Al ratio of 300-500 provides the best aromatics selectivity. Furthermore, CO selectivity is at its minimum value for Si/Al>300, which is attributed to the promotion of the RWGS reaction under high acid densities (low Si/Al ratios). Finally, conversion decreases as the acid site density decreases, and becomes very close to the conversion of the H-ZSM-5-free catalyst at very low acid densities.

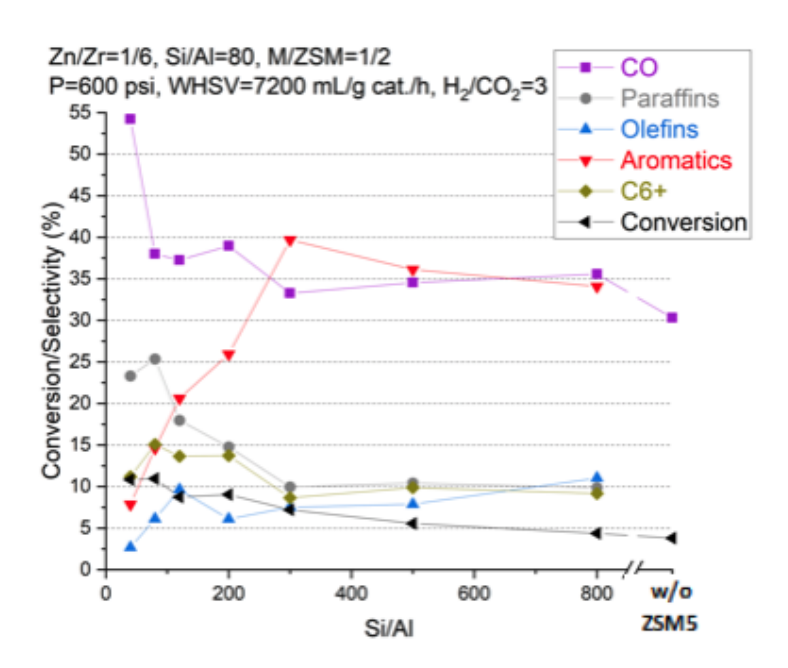


Figure 18: Studying the effect of Si/Al ratio on the performance of CO<sub>2</sub> aromatization reaction. Reaction conditions: 320 °C, 600 psi, and 7200 mL/g<sub>cal</sub>/h

Having a closer look at the product distribution for a sample experiment with ZnZrO/H-ZSM-5-300, the catalyst that provided the highest aromatics selectivity, gives some further insight into the performance of this catalyst. Figure 19A shows the distribution of non-aromatic hydrocarbons. Interestingly, while paraffins formed in the system are in the C1-C6+ range, it is clear that olefins do not follow the ASF distribution; the only olefins that are present in the system are ethylene and propylene. Furthermore, olefins, as the intermediate species, form 29% of non-aromatic hydrocarbons. This shows that the aromatics selectivity can further improve upon modifying the catalyst design so that it converts these unreacted intermediates. Figure 19B shows the aromatics products distribution. Among different aromatics, C9 products are the most common species; a similar observation was reported in previous studies. This is possibly due to (de)alkylation reactions on the external surface of the catalyst, which gets intensified in our catalyst due to its small crystal size and high external surface area. Poisoning the surface acid sites of the catalyst or reducing the diffusion path lengths are the key methods that we hypothesize can lead to lower ratios of C9+ chemicals within the aromatic compounds.

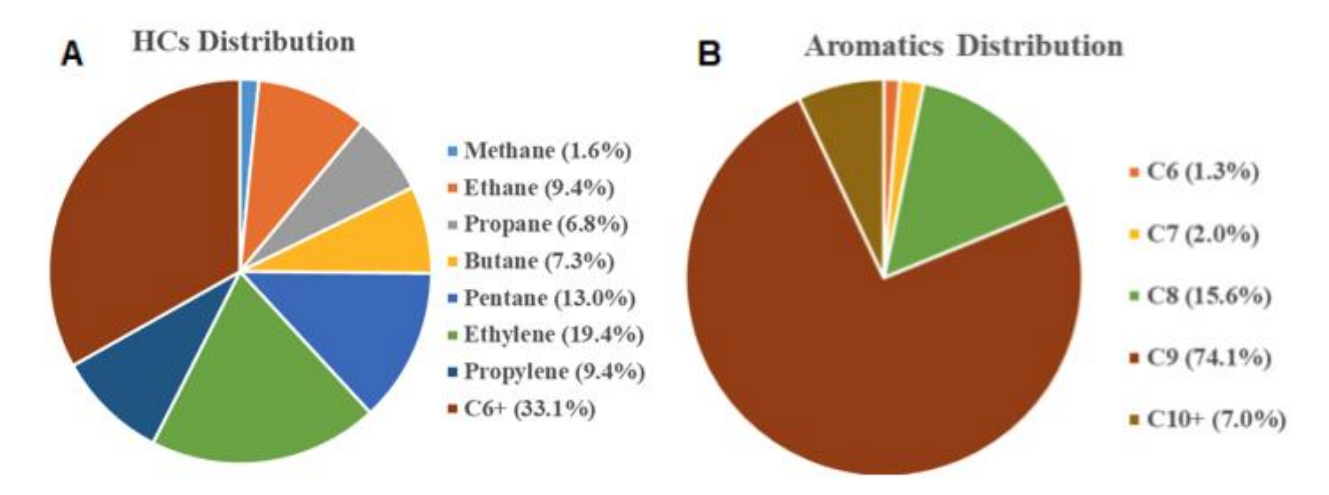


Figure 19: Detailed product distribution among (A) aliphatic hydrocarbons and (B) aromatic hydrocarbons. Reactions are done with the ZnZrO/H-ZSM-5-300-300 catalyst at 320 °C, 600 psi and 7200 mL/g<sub>cat</sub>/h

#### Subtask 4.3 – Experimental evaluation of impact of CO<sub>2</sub>/H<sub>2</sub> ratio:

The ideal Si/Al ratio, temperature, and WHSV for the ZnZrO/H-ZSM-5 catalyst were identified in the previous subtask. ZnZrO/H-ZSM-5 catalyst with a Si/Al ratio of 300 at 320 °C, 600 psi, and WHSV of 7,200 mL/gcat/h provides the most optimum conditions for the highest aromatics selectivity of 44% at about 7% CO<sub>2</sub> conversion. Therefore, these conditions were used to evaluate the reactions behavior at different H<sub>2</sub>/CO<sub>2</sub> ratios.

The H<sub>2</sub>/CO<sub>2</sub> ratios of 1.5, 2, 3, 4, and 6 were chosen for this subtask. These values were chosen in an effort to analyze the reaction performance at feed ratios below, equal, and above the stoichiometric H<sub>2</sub>/CO<sub>2</sub> ratio of 3, the value required for activating the first step of the reaction, i.e. CO<sub>2</sub> conversion to methanol. The CO<sub>2</sub>/N<sub>2</sub> ratio was kept fixed in all experiments to maintain the composition of the flue gas. The mass flow controllers of H<sub>2</sub>, CO<sub>2</sub>, and N<sub>2</sub> were adjusted for each experiment to obtain the desired ratios. Before the start of each reaction, the reactor was washed three times, each time for 10 hours with the new feed composition, to assure that the feed composition will stay steady during the course of the experiment.

Figure 20 shows the overall reaction performance at different feed compositions. The CO<sub>2</sub> conversion steadily increases from 3% to 11% upon the increase in H<sub>2</sub>/CO<sub>2</sub> ratio. This is mainly due to the expected increase in the rate of RWGS reaction, methanol synthesis reaction, and olefins hydrogenation to paraffins reactions in the presence of excess amounts of hydrogen. The CO selectivity has a minimum value at the H<sub>2</sub>/CO<sub>2</sub> ratio of 3. The ratios below 3 are excess in hydrogen for the RWGS reaction while it is below the stoichiometric value for the CO<sub>2</sub> to methanol reaction. The increasing trend in CO selectivity observed at high H<sub>2</sub>/CO<sub>2</sub> ratios is unlike what is reported in similar studies using different families and compositions of catalysts.<sup>7,14</sup> It appears that for the catalyst used in our studies, the increasing trend in the rate of RWGS reaction outweighs the increase in the rate of CO hydrogenation and the decrease in the rate of olefins aromatization (discussed below) at high H<sub>2</sub>/CO<sub>2</sub> ratios. This leads to an overall increase in CO selectivity

when increasing the  $H_2/CO_2$  ratio from 4 to 6. More investigations could be performed to verify and justify this observation.

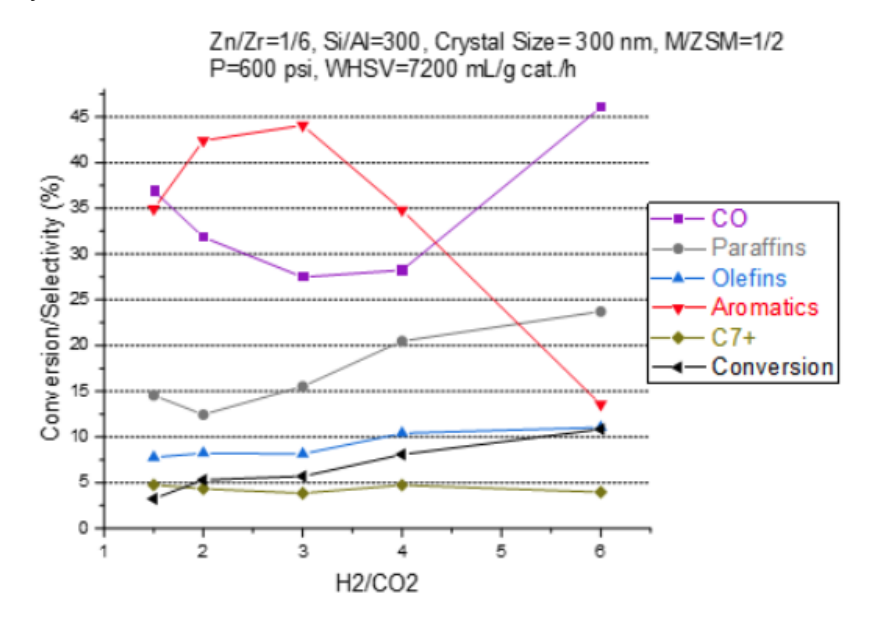


Figure 20: Reaction performance at different H<sub>2</sub>/CO<sub>2</sub> ratios

The aromatics selectivity is maximized at the H<sub>2</sub>/CO<sub>2</sub> ratio of 3. As mentioned earlier, the values below 3 are excess in hydrogen for the RWGS reaction and limited in hydrogen for producing the intermediate methanol. Moreover, excess amounts of hydrogen can act as an inhibitor for the rate-limiting step of the aromatization reaction, olefin dehydrogenation.<sup>30</sup> Other research groups further confirm this by observing a drop in aromatics selectivity upon introducing hydrogen to methanol and ethylene for the aromatization reaction.<sup>14</sup>

The aromatics selectivity of 44.1% at 5.7%  $CO_2$  conversion provides the highest aromatics selectivity of 0.89 mmol  $CO_2/g_{cat}/h$ . This value is in the same range as those reported in similar studies in the literature using metal oxide/zeolite catalysts.<sup>14,25,31</sup> In some cases, the aromatics formation rate is higher, <sup>20,26</sup> mainly due to the use of flue gas concentration feed in our study, which has 10-15%  $CO_2$  concentration, compared to other studies with pure  $CO_2$  co-fed with hydrogen.

#### D. Conclusions

<u>Subtask 4.1 - Experimental evaluation of "control" catalysts:</u> Catalysts Cu/Zn/Al, ZnZrO, ZnGa<sub>2</sub>O<sub>4</sub> are studied for conversion of CO<sub>2</sub> to MeOH. Of the three catalysts studied, it was found that the ZnZrO catalyst shows the optimum performance for MeOH production.

<u>Subtask 4.2 – Experimental evaluation of physical mixtures of catalysts:</u> Catalyst ZnZrO was used for  $CO_2$  hydrogenation for production of methanol. The aromatization catalyst H-ZSM-5 was synthesized for varying Si/Al ratios from 20 to 800 as well as with no Al in the framework. Of the multiple H-ZSM-5 synthesized and mixed with ZnZrO and tested for  $CO_2$  hydrogenation, H-ZSM-5 with Si/Al = 300 shows the best performance. This

catalyst was then further tested for optimum performance with respect to WHSV and temperature. It was found that temperature of 320  $^{\circ}$ C, WHSV of 7200 mL/g<sub>cat</sub>/h shows the best performance.

<u>Subtask 4.3 – Experimental evaluation of impact of  $CO_2/H_2$  ratio</u>: The best performing catalyst ZnZrO/H-ZSM-5-300 was tested for optimum performance for varying  $CO_2/H_2$  ratio between 1 to 6. It was found that the ratio  $CO_2/H_2 = 3$  would show the maximum selectivity for aromatics.

### VII. Task 5.0 – Computational Modeling of Baseline Systems

### A. Goals and Objectives of the Task

Density functional theory (DFT) calculations of energetics of relevant species for known methanol (Cu) and hydrocarbon (Co) catalysts will be performed and collected from databases to establish rate constants for steady-state microkinetic models of CO<sub>2</sub> hydrogenation.

<u>Subtask 5.1 – Develop microkinetic mode</u>l: A model for CO2+H2 → CH4, C2H6, MeOH, EtOH will be prepared based on mechanisms in the existing literature.

<u>Subtask 5.2 – Calculate DFT-based rates</u>: DFT calculations necessary to supplement existing data to calculate rates for Cu (111) surf aces will be completed.

<u>Subtask 5.3 – Calculate rates under varied conditions</u>: CatMAP will be utilized to rapidly calculate rate as a function of gas composition for Cu (111) surfaces.

# A. Background and Research Methods

This task started with a broad literature review on the chemical pathways for methane and methanol synthesis from carbon dioxide, carbon monoxide, and hydrogen mixtures. A complete microkinetic model spanning chemical paths toward low-molecular-weight alcohols, methanol and ethanol, paraffinic compounds, methane and ethane, and other oxygenate byproducts: formic acid, methyl formate, formaldehyde, and acetaldehyde.

The microkinetic model was implemented in the CatMAP<sup>32</sup> (python-library) framework. Its structure, i.e., a set of elementary reactions and underlying thermochemistry, was determined as a tailored combination of different literature reference data. Grabow and Mavrikakis<sup>33</sup>; carbon dioxide hydrogenation to methanol, single-carbon oxygenate compounds and methyl formate, forward and reverse water-gas-shift on Cu(111). Falsig et al.<sup>34,35</sup>: O<sub>2</sub> adsorption-desorption and dissociation on Cu(111). Wang et al.<sup>36</sup>: formaldehyde adsorption-desorption on Cu(111). Schumann et al.<sup>37</sup>: pathways to acetaldehyde and ethanol on Cu(111). Hansen et al.<sup>4</sup>: ethane route on Cu(111).

The formation-energy approach was used to re-parametrize the reaction and activation energies to consistent reference states to ensure thermodynamic consistency between studies. Vibrational frequencies were utilized to generate thermodynamic data (entropy, enthalpy, and heat capacity) by the harmonic approximation for further Shomate-equation parameters regression. Whenever vibrational frequencies were not available for transition

states, an average thermal correction in terms of the involved initial and final state corrections was included as an approximation for the transition state thermal correction.

A modular-schematic overview of tasks involved in the baseline system construction workflow is shown in Figure 21. A single microkinetic model structure (3) spanning both copper and cobalt catalysts routes. Additionally, composition and thermodynamic mappings (4) can be calculated once a microkinetic model structure and thermodynamic data are available.

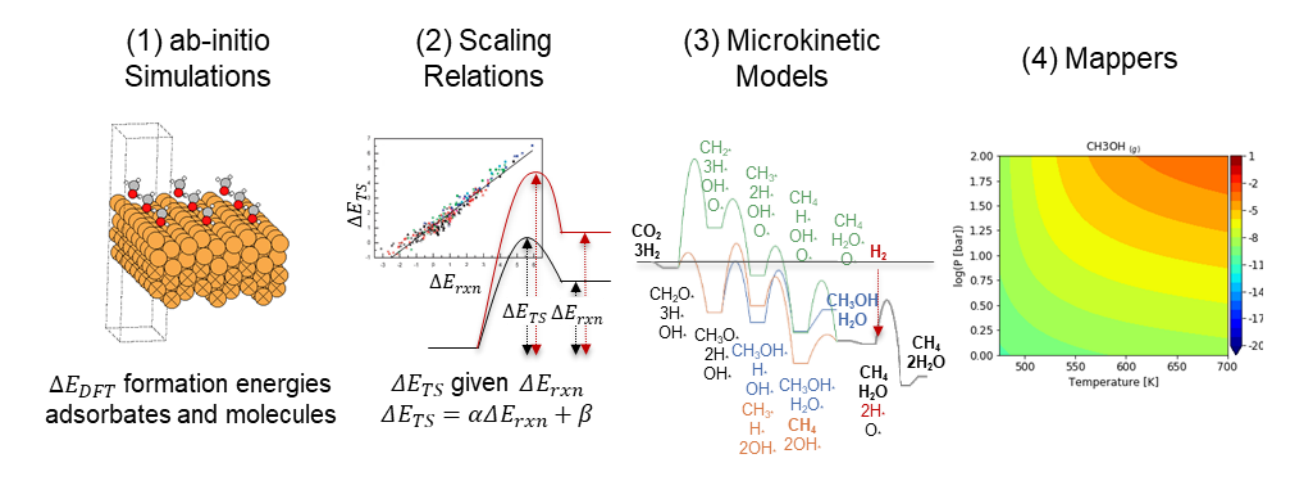


Figure 21. Workflow overview: from left to right, (1) ab-initio DFT-simulations, (2) scaling relations, (3) microkinetic models and (4) mappers.

#### B. Results and Discussions

### (i) Subtask 5.1 – Develop microkinetic model

#### (a) Microkinetic model

For the solution of mean-field microkinetic models one relies on the assumption that surface reaction rates are significantly faster than adsorption-desorption steps; whereby the pseudo-steady-state hypothesis (PSSH) or quasi-steady-state approximation allows turn-over frequency estimation as the solution of differential algebraic equations, as in equation (1), where M is the stoichiometric matrix, with positive and negative integer entries as a linear map from reaction rate equations  $r_j$  and material balances of species i, i.e.  $\sum_j M_{i,j} r_j = \delta_i$ . Under PSSH,  $\delta_i \approx 0$  if i is a surface species and  $\delta_i \neq 0$  if i is a bulk-phase species.

$$M \times \mathbf{r} = \delta \mid M \in \mathcal{N}^{n \times m}, \, r \in \mathcal{R}^m, \, \delta \in \mathcal{R}^n \tag{1}$$

Microkinetic model solutions are obtained by finding adsorbate coverage fractions  $\theta$ :  $\sum_i \theta_i = 1$  such that the PSSH is satisfied. It can be shown that a reduced version of (1) can be solved in terms of adsorbate coverage fractions only with no slack or surplus degrees of freedom<sup>38</sup>. Nevertheless, rate equation terms are typically nonlinear with

respect to  $\theta$  and solution is obtained through an iterative processes based on linearization of (1), as shown in (2), which are highly dependent on initial guesses for  $\theta$ .

$$\Delta\theta_{k} \mid M \times (r_{k} + \nabla_{\theta} r_{k} \times \Delta\theta_{k}) = \delta = 0\theta_{k+1} = \theta_{k} + \Delta\theta_{k} r_{k+1} = r(\theta_{k+1})$$

$$= r(\theta_{k} + \Delta\theta_{k})$$
(2)

At each iteration,  $\theta$  update is obtained either by diagonalization/factorization methods (e.g., LU-, LDL-, QR-decomposition) or complementary iterative ordinary-differential equation methods (ODE, e.g., Euler, Runge-Kutta methods). Currently, CatMAP resorts to standard libraries to perform LU-decomposition and solve for  $\theta$  updates according to (2). The CatMAP framework initializes  $\theta$  according to a Boltzmann-distribution over adsorbate binding energies and adopts a descriptor-based mapping philosophy (e.g., temperature and pressure, concentration ensembles) that speeds up successive solution iterative processes by continuously bisecting previously found solutions as initial guesses for the following nearby points in the descriptor map.

### (b) Rate equations and thermochemistry

Elementary reactions are assumed to obey power-law kinetics, as in (3).

$$r_j = k_j \prod_{p} \theta_{j,p}^{M_{j,p}} \mid k \in \mathcal{R}^m, \theta_j \subset \theta \in \mathcal{R}^n$$
(3)

Where  $k_j$  is rate constant and  $\theta_{j,p}$  are reactants coverage fractions or concentrations involved in the elementary rate j. The transition state theory (TST) derives rate constants from system partition functions as described in (4):

$$k_{j} = \frac{k_{B}T}{h} \exp\left(-\frac{\Delta G^{0^{\ddagger}}}{k_{B}T}\right) = \frac{k_{B}T}{h} \exp\left(\frac{S^{0^{\ddagger}}}{k_{B}}\right) \exp\left(-\frac{\Delta H^{0^{\ddagger}}}{k_{B}T}\right) \tag{4}$$

in which  $k_B$  is the Boltzmann constant, h is Planck constant and  $\Delta G^{0^{\ddagger}}$  is the change in standard Gibbs free energy between the initial state (reactants) and the corresponding reaction transition state. Consequently, a microkinetic model can be assessed at different temperatures as long as the Gibbs free energy of each species and transition states can be estimated with satisfactory accuracy.

CatMAP handles the enthalpic Gibbs free energy parcel from different contributions: electronic structure (density functional theory or DFT-energy), zero-point-energy (ZPE) and thermal (Cp) corrections, as in (5). DFT energies (E) are obtained from expensive quantum mechanical simulations and ZPE. Cp corrections and total entropy can be determined from species vibrational frequencies by using the harmonic approximation or correlations or, for the latter two, empirical correlations.

$$H_i^0(T) = E_i + ZPE_i + \int_{T_{ref}}^{T} Cp_i(T) dT$$
 (5)

In this work, whenever only vibrational frequencies were available for species, entropies and enthalpies were evaluated under the harmonic approximation and successively fitted to Shomate equations<sup>39</sup>, for parameters A to H, as shown in (6), so that thermodynamic properties can be simply evaluated instead of calculated during the iterative solution process.

$$Cp^{0} [J/mol K] = A + Bt + Ct^{2} + Dt^{3} + E/t$$

$$\Delta H^{0} [kJ/mol K] = At + Bt^{2}/2 + Ct^{3}/3 + Dt^{4}/4 - E/t + F - H$$

$$S^{0} [J/mol K] = A \ln(t) + Bt + Ct^{2}/2 + Dt^{3}/3 - E/2t^{2} + G$$

$$t = T [K]/1000$$
(6)

Once thermodynamic properties can be evaluated as a function of thermodynamic variables, DFT energies and ZPE corrections are available, the microkinetic model can be evaluated at different conditions.

#### (c) Reaction mechanism

The reaction mechanism encompasses 62 different elementary reactions, with 12 gasand 30 adsorbate-species as shown in Table 2 along with their respective references, DFT energy of reaction,  $\Delta E_r$ , and activation energy,  $E_A$ .

Table 2 – Elementary steps relevant to reaction mechanism(s)

Reaction	$\Delta E_r (eV)$	$E_A(eV)$	Reference
$CO_{2(g)} + * \rightarrow CO_2*$	-0.08	0	Grabow & Mavrikakis <sup>33</sup>
$H_{2(g)} + 2^* \rightarrow 2H^*$	-0.29	0	
$CO_{(g)}$ + * $\rightarrow$ $CO$ *	-0.86	0	
$H_2O_{(g)} + * {}_{\rightarrow} H_2O*$	-0.21	0	
HCOOH <sub>(g)</sub> + * → HCOOH*	-0.22	0	
$CH_2O_{(g)}$ + * $\rightarrow$ $CH_2O^*$	-0.04	0	
$CH_3OH_{(g)} + * \rightarrow CH_3OH^*$	-0.28	0	
HCOOCH <sub>3</sub> (g) + * → HCOOCH <sub>3</sub> *	-0.10	0	
$CO^* + O^* \rightarrow CO_2^* + *$	-1.12	0.65	
CO* + OH* → COOH* + *	0.14	0.56	
$COOH^* + * \rightarrow CO_2^* + H^*$	-0.55	1.23	
$COOH^* + OH^* \rightarrow CO_2^* + H_2O^*$	-0.76	0	
COOH* + H* → HCOOH* + *	-0.59	0.73	
$H_2O^* + * \rightarrow OH^* + H^*$	0.21	1.39	
$OH^* + * \rightarrow O^* + H^*$	0.72	1.68	
2OH* → H2O* + O*	0.51	0.61	
CO2* + H* → HCOO* + *	-0.25	0.87	
$HCOO^* + H^* \rightarrow H_2CO_2^* + *$	0.87	1.59	

HCOO* + H* → HCOOH* + *	0.23	0.91	
HCOOH* + H* → CH <sub>3</sub> O <sub>2</sub> * + *	0.10	1.04	
$H_2CO_2^* + H^* \rightarrow CH_3O_2^* + *$	-0.54	0.74	
$H_2CO_2^* + ^* \rightarrow CH_2O^* + O^*$	0.91	0.91	
$CH_3O_2^* + * \rightarrow CH_2O^* + OH^*$	0.74	0.74	
$CH_2O^* + H^* \rightarrow CH_3O^* + *$	-1.02	0.24	
CH <sub>3</sub> O* + H* → CH <sub>3</sub> OH* + *	-0.23	1.17	
CO* + H* → HCO* + *	0.78	0.99	
CO* + H* → COH* + *	1.15	2.26	
HCOO* + * → HCO* + O*	2.18	2.36	
HCO* + H* → HCOH* + *	0.09	0.91	
HCO* + H* → CH <sub>2</sub> O* + *	-0.40	0.47	
$CH_2O^* + H^* \rightarrow CH_2OH^* + *$	-0.06	0.82	
HCOH* + H* → CH <sub>2</sub> OH* + *	-0.55	0.47	
$CH_2OH^* + H^* \rightarrow CH_3OH^* + *$	-1.19	0.51	
HCOOH* + * → HCO* + OH*	1.24	1.63	
HCOOH* + * → HCOH* + O*	2.04	2.5	
$CH_3O_2^* + * \rightarrow CH_2OH^* + O^*$	1.39	2.01	
$CO_2^* + O^* \rightarrow CO_3^* + ^*$	0.11	0.34	
$CO_3^* + H^* \rightarrow HCO_3^* + *$	-1.21	1	
O* + HCO* → OH* + CO*	-1.50	0	
$OH^* + HCO^* \rightarrow H_2O^* + CO^*$	-0.99	0.30	
HCOO* + HCO* → HCOOH* + CO*	-0.56	0.60	
$HCOO^* + HCO^* \rightarrow H_2CO_2^* + CO^*$	0.09	0.80	
$HCOOH^* + HCO^* \rightarrow CH_3O_2^* + CO^*$	-0.68	0.42	
$CH_2O^* + HCO^* \rightarrow CH_3O^* + CO^*$	-1.81	0	
$CH_3O^* + HCO^* \rightarrow CH_3OH^* + CO^*$	-1.02	0.38	
$CH_3O^* + HCOO^* \rightarrow HCOOCH_3^* + O^*$		1.24	
$CH_3O^* + CH_2O^* \rightarrow H_2COOCH_3^* + ^*$	-0.78	0.13	
$HCOOCH_3^* + H^* \rightarrow H_2COOCH_3^* + *$	0.01	0.94	
2CH <sub>2</sub> O* → HCOOCH <sub>3</sub> * + *	-1.81	1.11	
$O_{2(g)} + * \rightarrow O_{2}*$	-0.21	0	Falsig et al. <sup>35</sup>
$O_2^* + ^* \rightarrow 2O^*$	-2.38	0.22	Falsig et al. <sup>34</sup>
$C_2H_{6(g)} + 2^* \rightarrow 2CH_3^*$	1.46	3.51	Hansen et al. <sup>4</sup>
$CH_2O^* + * \rightarrow CH_2^* + O^*$	0.83	2.45	Wang et. al. <sup>36</sup>
$CH_3O^* + H^* \rightarrow CH_3^* + OH^*$	0.22	1.58	Schumann et al.37
$CH_3CO^* + * \rightarrow CH_3^* + CO^*$	0.46	1.35	
CH <sub>3</sub> CHO* + * → CH <sub>3</sub> CO* + H*	0.78	1.26	
$CH_3CHO_{(g)} + * \rightarrow CH_3CHO*$	0.41	0	
$CH_3^* + * \rightarrow CH_2^* + H^*$	1.15	1.68	
$CH_{4(g)} + 2^* \rightarrow CH_3^* + H^*$	1.31	1.89	
$CH_3CH_2OH^* \rightarrow CH_3CH_2OH_{(g)} + *$	0.33	0	
CH <sub>3</sub> CHOH* + * → CH <sub>3</sub> CHO* + H*	-0.46	0.76	
CH <sub>3</sub> CH <sub>2</sub> OH* + * → CH <sub>3</sub> CHOH* + H*	1.42	1.84	

#### (d) Formation energy overall consistency

Since multiple references have been used to build the microkinetic model, formation energies associated with individual species cannot be utilized as is; however, formation energies can be estimated as a linear combination of reaction energies if energies are indirectly assigned to each atom in the system. An algebraic representation of this relationship is as follows:

$$M \times \Delta E_f = \Delta E_r \mid M \in \mathcal{N}^{n \times m}, \Delta E_f \in \mathcal{R}^m \text{ and } \Delta E_r \in \mathcal{R}^n$$
 (7)

where M is the microkinetic model stoichiometric matrix,  $\Delta E_f$  is an array of species formation energies and  $\Delta E_r$  is a reaction DFT-energy array. We have developed a programmatic strategy to assess whether the microkinetic model is consistent and to <u>parametrize</u> formation energies in terms of arbitrary reference species. The strategy consists of performing singular-value decomposition (SVD) on M and analyzing the singular value spectrum:

$$U \times S \times V^{T} = M \mid U \in \mathcal{R}^{n \times n}, S \in \mathcal{R}^{\min(n,m)}, V \in \mathcal{R}^{m \times m}$$
 (8)

where U and V are the orthonormal basis of  $\mathcal{R}^{n\times n}$  and  $\mathcal{R}^{m\times m}$ , such that  $U^TU=I$  and  $V^TV=I$ , respectively, and S is a diagonal matrix with singular values along its diagonal.

Figure 22 conveys that out of the 42 involved species there are 4 degrees of freedom, which are related to the number of different atoms among all chemical species plus the catalytic site. Therefore, as long as (a) three species are arbitrarily chosen such that the set of all their atoms wholly constitute all other chemical species (i.e. each atomic species has a corresponding molecular reference), (b) some energy is associated to catalytic sites (i.e. the surface energy of the active surface is defined) and (c)  $U^T \Delta E_r \in \mathcal{R}^n$ , meaning that the projection of  $\Delta E_r$  on  $U^T$  has at most n non-zero elements (i.e. we decompose M into its largest subset of linearly independent or non-redundant elementary reactions), the problem becomes well posed.

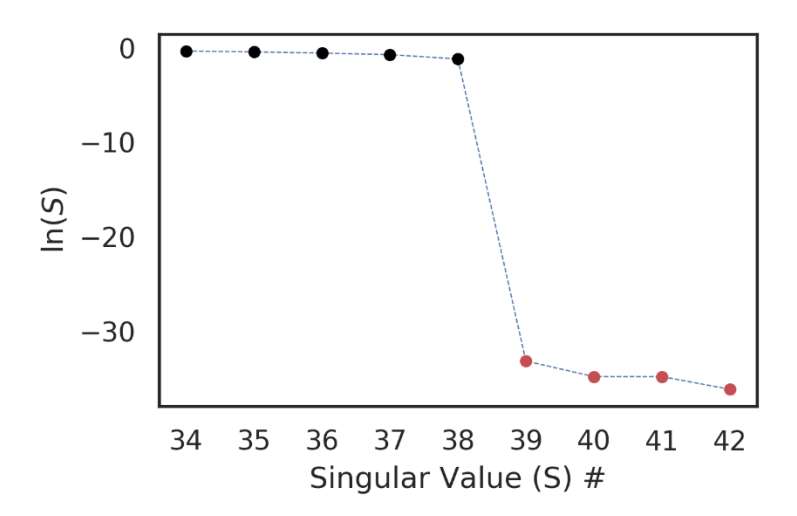


Figure 22 - Stoichiometric matrix, M, singular values.

For this work, gas phase (desorbed) methane, carbon dioxide and carbon monoxide were chosen as reference species, such that (7) can be rewritten as:

$$M' \times \Delta E_f' = \Delta E_r - M^{ref} \times \Delta E_f^{ref} = \Delta E_r'$$

$$M' \in \mathcal{N}^{n \times m - 4}, \Delta E_f' \in \mathcal{R}^{m - 4}, M^{ref} \in \mathcal{N}^{n \times 4}, \Delta E_f^{ref} \in \mathcal{R}^4 \text{ and } \Delta E_r \in \mathcal{R}^n$$

$$(9)$$

where  $M^{ref}$  consists of the columns of M that correspond to reference species and M' are the remaining columns.  $\Delta E'_f$  is a column vector of non-reference species formation energies for which we are solving and are parametrized by  $\Delta E^{ref}_f$ . Following this, we confirm for condition (c), as in Figure 23, by performing SVD on M', such that  $U'S'V'^T = M'$ , allowing the direct solution for  $\Delta E'_f$  in (9) by evaluating the following expression. Chemically, this corresponds to finding a linear map that connects the reaction-specific energies to thermodynamically-consistent species-specific energies.

$$\Delta E_f' = V' S'^{-1} U'^T \Delta E_r' \tag{10}$$

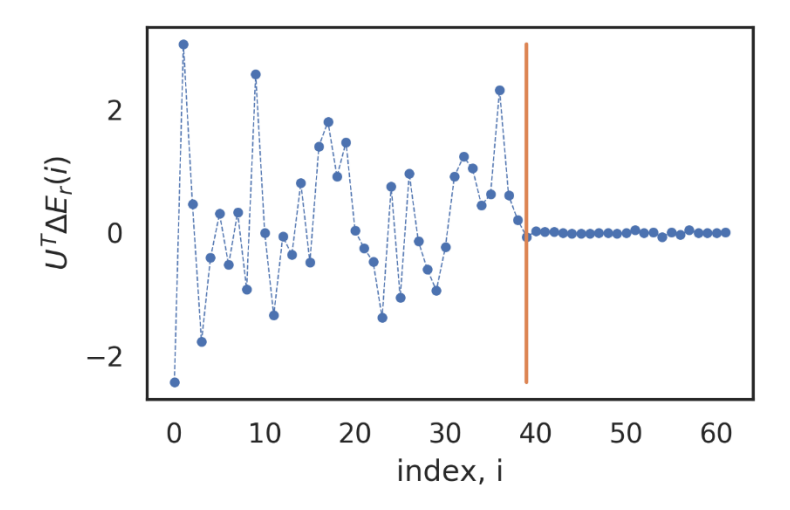


Figure 23 –  $U^T \Delta E_r$  spectrum.

Figure 24 portrays the robust results from parametrization, with the Pearson correlation coefficient over 0.999 and absolute error below  $10^{-2}$  eV. Such parametrization will be used whenever new reactions are appended to the current chemical path scaffold, not only to automate formation energy calculations given by the arbitrary references, but also to detect disconnected chemical paths, which arise as additional degrees of freedom in the M' singular value spectrum.

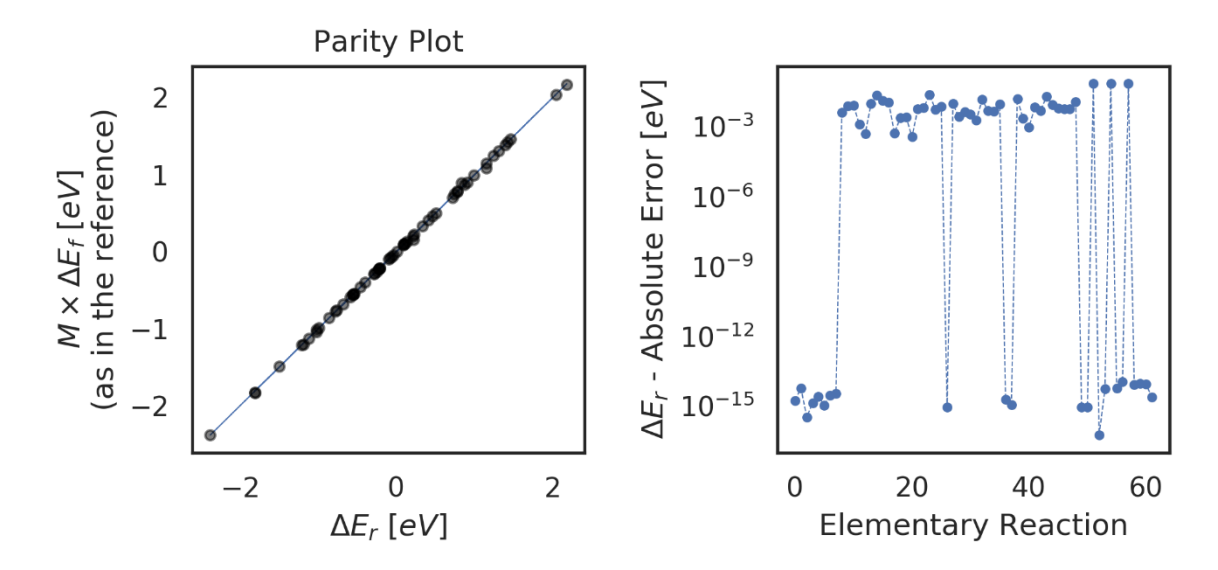


Figure 24 – Parity plot (left) and absolute error (right) between reference and estimated elementary reaction energies.

The overall comprehensive CO<sub>2</sub>-hydrogenation microkinetic-model structure, entailing 42 species and 62 elementary-reaction steps, has been described in Q2 Report and minor additions have been included in Q3 and Q4. As conveyed in the Q3 report, the initial mechanism, which was centered about the production of methanol on Cu(111), was

extended to entail relevant intermediate molecules and associated elementary steps believed to be present on cobalt; therefore, it ultimately enables a single model to mimic both copper- and cobalt-exclusive reactions and those which are common to both.

# (ii) Subtask 5.2 – Calculate DFT-based rates

DFT-based rates are given as gas species turn-over frequencies (TOF) calculated from the solution of the mean-field microkinetic model under PSSH at different gas-phase concentrations and thermodynamic descriptors, pressure, and temperature. In this report, we convey TOFs estimated over a wide range of temperatures and pressures, i.e., from 450 K to 700 K and 1 bar to 100 bar, respectively, for Cu(111), which is a direct parallel to the Cu(211) surface in terms of relative TOFs.

According to results shown in Figure 25, copper is more active for the production of methanol as compared to methane over the temperature and pressure ranges under analysis and fixed bulk phase reactants concentrations. The maps also confirm that rates increase with temperature and pressure, consistent with chemical intuition. Figure 25 may also be referred to as 'volcano plot'. Water formation exhibits the same behavior as methane.

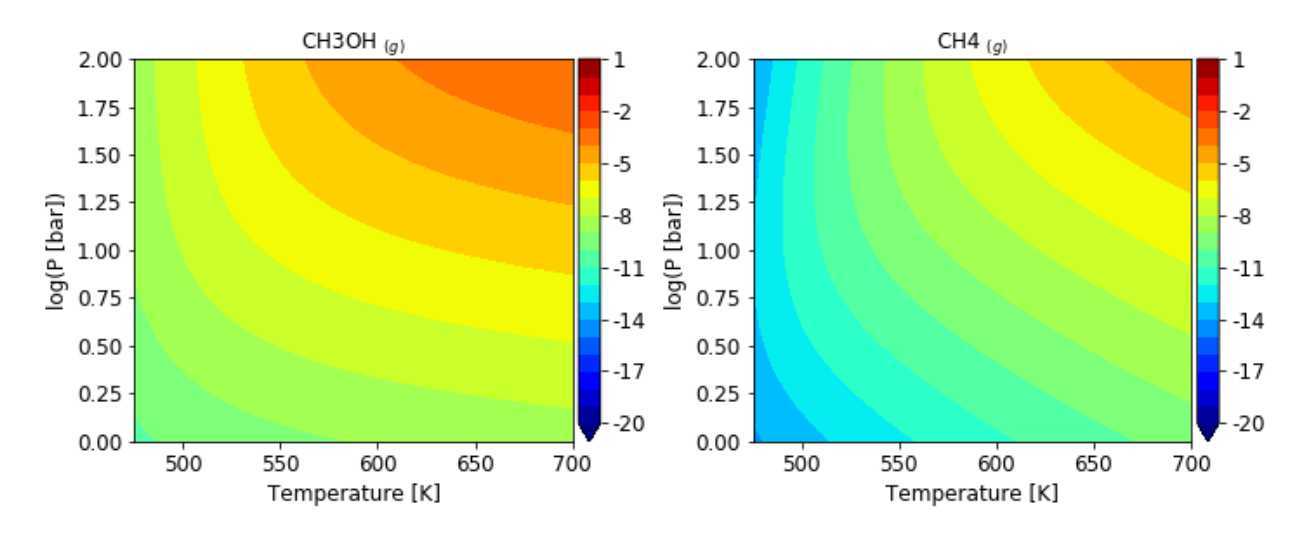


Figure 25 – Main reaction products calculated  $log_{10}(TOF)$  at bulk phasestatic concentration of 0.05:0.05:0.90 CO:CO<sub>2</sub>:H<sub>2</sub>.

Since microkinetic model-derived TOFs reflect instantaneous rates in the mean-field sense for a given chemical system, it is often found that even though the equilibrium constant for some specific reaction is unfavorable, the actual catalytic activity is high. The chemical system and reactions under appraisal follow a similar pattern. As shown in Figure 26, copper has a high activity for the production of formic acid and formaldehyde. However, since they are intermediate species along paths to methanol, it is expected that their composition rapidly equilibrates, causing the TOF's to drop to zero. However, the reaction will proceed in the direction of methane (most favorable species) and methanol since their concentrations will not approach equilibrium.

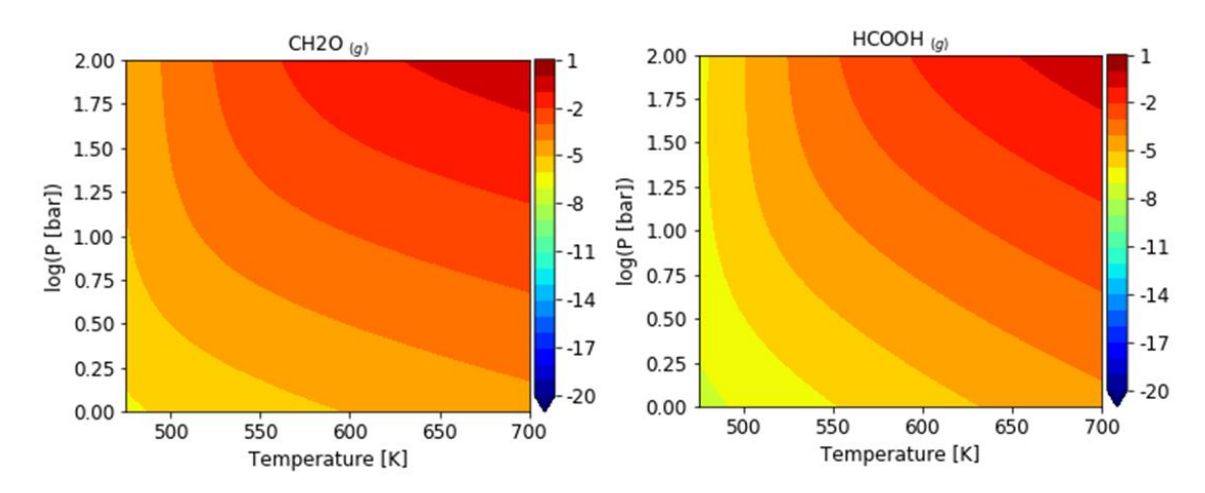


Figure 26 – Minor reaction products calculated log<sub>10</sub>(TOF) at bulk phasestatic concentration of 0.05:0.05:0.90 CO:CO<sub>2</sub>:H<sub>2</sub>.

#### (a) BEP (Brønsted-Evans-Polanyi) relations

The BEP (Brønsted–Evans–Polanyi) $^{40}$ , relations have been used to estimate transitions state energies ( $\Delta E_{TS}$ ), which are based on thelinear dependence with respect to their associated reaction energies ( $\Delta E_{rxn}$ ). Universal BEP mappings have been object of study in recent years, where for example Wang et. al. $^{41,42}$  assessed a subset of C-C and C-O coupling, and (de)hydrogenation reactions.

$$\Delta E_{TS} = \alpha \, \Delta E_{rxn} + \beta \tag{11}$$

Where  $\Delta E_{TS}$  is the activation barrier for the change in free-energy described by  $\Delta E_{rxn}$ . The parameters  $\alpha$  and  $\beta$  are fitted parameters which, in the case of BEP relations, map reaction energies to transition state energies across transition metals of the same facets, e.g. close-packed, stepped, etc.; hence, given such parameters for a specific elementary step, knowing reaction energies for a specific transition metal suffices for to one be able to estimate what the related transition state energies should be given the correlation-specific uncertainties, which are commonly published along.

To avoid using multiple references for the regressed  $\alpha$  and  $\beta$  parameters for the studied mechanism we chose to reduce the transition state estimation layer complexity by grouping all reactions into two types: hydrogen or heavy adatoms. This approach is consistent with the one adopted by Ullissi et. al.<sup>43</sup> when studying similar syngas conversion reactions.

### (b) DFT-energies estimation

The plane-wave density-functional theory (DFT) code Quantum Espresso (QE), version 6.5.1, has been used to estimate chemical species adsorption energies on the computer cluster operated by the Partnership for an Advanced Computing Environment (PACE)<sup>44</sup> at the Georgia Institute of Technology. Although QE has also been compiled with Bayesian Error Estimation Functional (BEEF)<sup>45</sup> to speed up calculations and results

generation, plain PBE (Perdew–Burke-Ernzerhof)<sup>46</sup> has been chosen as standard exchange correlation functional for the DFT-based rates. This strategy allows faster structural convergence of DFT simulations.

DFT adsorption energies for the intermediate species on Cu(111), Cu(211) and Co(211) have been calculated using QE 6.5.1. The simulation parameters were: standard solid-state pseudopotentials (SSSP), energy cutoff of 500 eV, (4,4,1) k-points, PBE exchange correlation functional, unrestricted Hartree-Fock (spin polarized), dipole corrections.

Figure 27 conveys the parity plot between formation energies estimated from this work's DFT simulations and those reported by Grabow and Mavrikakis<sup>33</sup>. There is general agreement between results, though the mean absolute difference between predicted reaction energies of around 0.65 eV. This is attributed to differences in the numerical techniques (energy cutoff, pseudopotentials) and physical approximation (exchange-correlation functional) used in the two studies.

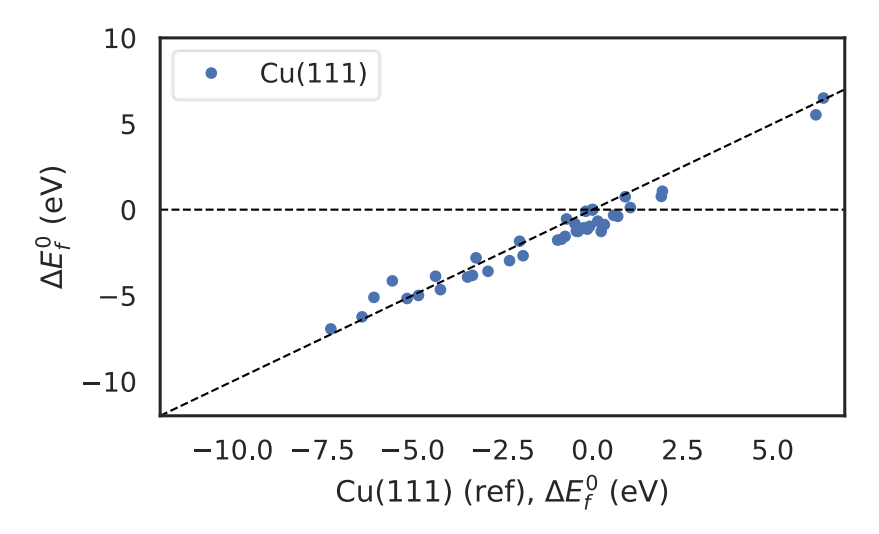


Figure 27. Calculated formation energies amd formation energies reported by Grabow and Mavrikakis<sup>33</sup> parity plot.

#### (iii) Subtask 5.3 – Calculate rates under varied conditions

The capability of calculating rates under varied conditions has been demonstrated for the initially devised mechanism for CO<sub>2</sub> hydrogenation in Subtask 5.2 – Calculate DFT-based rates, where turnover frequencies (TOF) were calculated over varying feed compositions, temperature, and total pressure ranges.

To perform model sensitivity analysis in terms of gas species concentrations (or molar fractions), an additional routine was created in CatMAP that allows the analysis TOFs given a varying ratio of two components at different balance species (in this case H<sub>2</sub>-only) proportions. More generally, let  $x_i$  be the molar fraction of species i. We can analyze the effect on TOF of varying the ratio  $\alpha$ , between species A and B molar fractions, and the fraction  $\beta$ , of A and B with respect to all other species molar fractions while keeping the the relative molar fractions between other species k not A or B fixed at  $r_k$ .

$$\alpha = x_A/x_B \tag{12}$$

$$\beta = \frac{x_A + x_B}{\sum_i x_i = 1} \tag{13}$$

$$r_k = \frac{x_k}{\sum_k x_k = 1 - \beta}; k \neq A \text{ or } B$$
 (14)

From equations (12) to (14), we can directly define x's as function of  $\alpha$ ,  $\beta$  and  $r_k$ , such that  $x_A = \alpha \beta/(1+\alpha)$ ,  $x_B = \beta/(1+\alpha)$  and  $x_k = (1-\beta) r_k$ ;  $\sum_k r_k = 1$ . As a base case study, this concentration mapping functionality was tested for varying carbon monoxide to carbon dioxide ratios at varying slack hydrogen at 650 K and 50 bar, as shown in Figure 28.

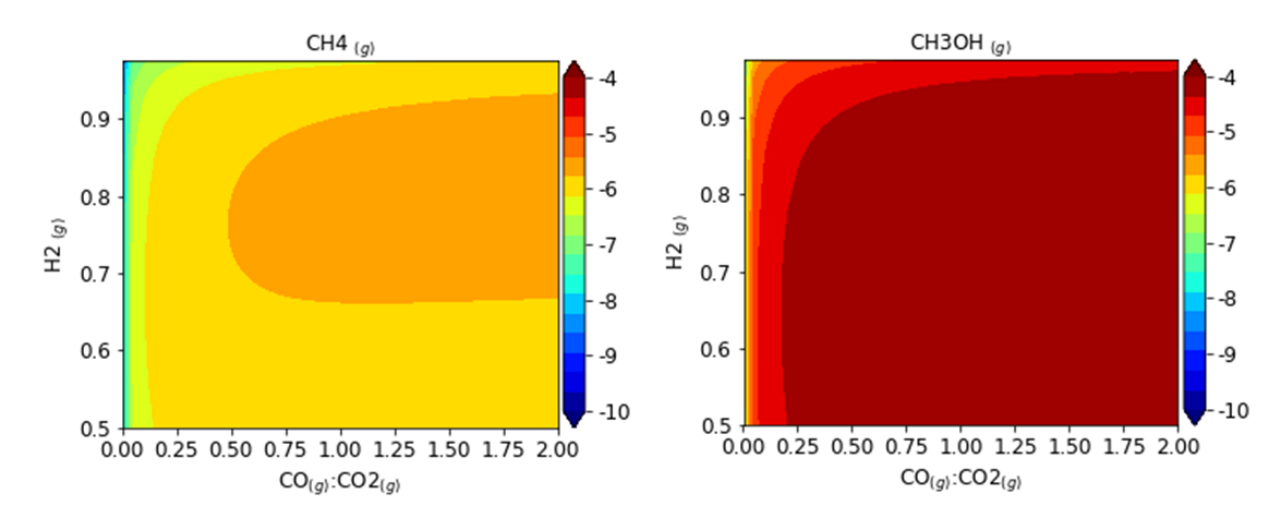


Figure 28 – Main reaction products  $log_{10}(TOF)$  as a function of gas-phase composition at 650K and 50 bar.

Hence, higher CO-to-CO<sub>2</sub> ratios favored not only methanol but also methane catalytic activity. We note that these volcano plots only allow inferences to be drawn in terms of intrinsic catalytic activity, or instantaneous rate. To calculate macroscale quantities such as selectivity, conversion, and yield, the microkinetic model would be solved as a source term in a macroscale reactor model. We are investigating the possibility of integrating the microkinetic model with more realistic process models (e.g., PFR) to provide this insight later in the project.

#### C. Conclusion

<u>Subtask 5.1 – Develop microkinetic model:</u> A full model has been devised encompassing all chemical species in the chemical system. Completion target was 3/31. Incremental changes to the microkinetic model might be necessary as new metals are explored.

<u>Subtask 5.2 – Calculate DFT-based rates</u>: DFT-based rates have been successfully evaluated for the microkinetic model under Cu(111) energies, and the effects of Cu(211)

and other defects were evaluated using parameters obtained from fits to experimental data. DFT-energies simulations on Cu(211) have been planned/executed.

<u>Subtask 5.3 – Calculate rates under varied conditions</u>: A general concentration mapper has been developed and added to the CatMAP framework. Results have been derived for Cu(111) and will be reassessed for other metal/lattices once DFT calculations are completed (Subtask 5.2).

# VIII. Task 6.0 – Experimental testing of different zeolite crystallite structure sizes

## A. Goals and Objectives of the Task

Using Subtask 4.2 as a basis, we control the reaction-diffusion length scales by changing the acid domain size within physical mixtures.

<u>Subtask 6.1 – Establish synthesis procedures:</u> Synthesis and routine characterization of ZSM5 structures with uniform (within a sample) but varied (across samples) crystallite sizes will be conducted.

<u>Subtask 6.2 – Experimental evaluation of impact of crystallite size:</u> The catalysts will be evaluated by steady-state conversion testing, measuring rates and selectivities to compare to the initial physical mixture synthesized in Subtask 4.2.

# B. Background and Research Methods

Subtask 6.1 – Establish synthesis procedures: The ZSM-5-300-120 was synthesized by the method reported by Zhang et al.<sup>29</sup> The starting molar ratio of the chemicals for this synthesis was 1.0 SiO<sub>2</sub>/0.45 TPAOH/0.0067 Al<sub>2</sub>O<sub>3</sub>/50 H<sub>2</sub>O/0.1 L-lysine, where *L*-lysine, as an inhibitor, effectively suppressed the crystal growth. First, tetrapropylammonium hydroxide (TPAOH) (Acros) was mixed with deionized water while stirring vigorously for 10 min. Then tetraethyl orthosilicate (TEOS) (Sigma-Aldrich), sodium aluminate (Sigma-Aldrich), and L-lysine (Sigma-Aldrich) were separately added to the mixture and the mixture was stirred for another 30 min. Next, the gel mixture was transferred into a Teflon-lined stainless-steel autoclave for crystallization at 80 °C for 2 days and 170 °C for 1 day. This two-step crystallization was adopted to further decrease the crystal size. The assynthesized solid products were centrifuged, washed with water several times, and dried at 80 °C overnight, followed by calcination at 550 °C for 6 h. The Na-form zeolite was further exchanged with the aqueous solution of NH<sub>4</sub>NO<sub>3</sub> (Sigma-Aldrich) (1.0 M) two times at 80 °C for 4 h to obtain the H-form ZSM-5.

The starting molar ratio of the chemicals for the synthesis of ZSM-5-300-350 was 1.0 SiO<sub>2</sub>/0.45 TPAOH/z Al<sub>2</sub>O<sub>3</sub>/150 H<sub>2</sub>O, with the value of z varying for the two Si/Al ratios desired. The synthesis recipe was the same as the one described for ZSM-5-300-120, excluding the addition of L-lysine, and having a single-step crystallization at 170 °C for two days.

The starting molar ratios for the synthesis of ZSM-5-300-850 and ZSM-5-300-2600 were 1.0 SiO<sub>2</sub>/0.15 TPAOH/0.0067 Al<sub>2</sub>O<sub>3</sub>/0.075 Na<sub>2</sub>O/50 H<sub>2</sub>O and 1.0 SiO<sub>2</sub>/0.1 TPAOH/0.0067 Al<sub>2</sub>O<sub>3</sub>/0.115 Na<sub>2</sub>O/50 H<sub>2</sub>O, respectively. The synthesis recipe for these two zeolites was similar to that of the ZSM-5-300-350; however, the molar ratio of TPAOH/SiO<sub>2</sub> was reduced, and 10% NaOH (Sigma-Aldrich) was added to adjust the pH of the synthesis mixture.<sup>47</sup> Moreover, TEOS and Ludox AS-40 (Sigma-Aldrich) were used as the silica sources for obtaining crystal sizes of 850 nm and 2600 nm, respectively.

<u>Subtask 6.2 – Experimental evaluation of impact of crystallite size:</u> The reaction conditions were also obtained based on previous sections at 320 °C, 600 psi, and 7,200 mL/g<sub>catalyst</sub>/h and H<sub>2</sub>/CO<sub>2</sub> ratio of 3. All results are obtained at similar CO<sub>2</sub> conversion, which excludes the impact of intermediate products concentration variations on the catalytic performance and provides a fair comparison between different H-ZSM-5 crystal sizes studied. Several experiments were conducted using H-ZSM-5 of different crystal sizes in combination with ZnZrO<sub>x</sub> in different bed orientations. The bed orientations are (i) separate beds, (ii) mixed particles, and (iii) mixed powders.

#### C. Results and Discussions

Subtask 6.2 – Experimental evaluation of impact of crystallite size: Several experiments were conducted using H-ZSM-5 of different crystal sizes in combination with ZnZrO in different bed orientations. The bed orientations are (i) separate beds, (ii) mixed particles, and (iii) mixed powders, where the separate bed structure provides the lowest interactions between the two functionalities, and the mixed powders provides the highest. The results of these studies are shown in Figure 29. Generally, the highest aromatics selectivity was obtained for the mixed powders, since the diffusion path length is the shortest and the common interfacial surface area is the highest when the catalyst particles are the smallest and have more interactions with each other. The catalytic performance of the two other bed structures is very similar to each other, with the conversion being slightly higher in the mixed particles case compared to the separate beds. This is probably due to the increased contact time between the reactant and the ZnZrO particles because of the mixing effect in the case of mixed particles.

Upon increasing the zeolite crystal sizes from 100 nm to 2600 nm, there are two different behaviors observed at different bed orientations. For the separate beds and mixed particles orientations, the aromatics selectivity increases as the zeolite crystal size decreases. This is expected since shorter reaction-diffusion length scales are achieved at smaller crystal sizes of zeolites. The major side-products of this system are recognized as CO and paraffins, CO is the side-product that is produced via the metal-oxide domain and paraffins are the side-products produced over both metal-oxide and H-ZSM-5 domains.<sup>6,20</sup> The shorter diffusion path length will reduce the distance that the intermediate chemicals must travel over these sites, and therefore reduces the opportunities of undesired side-reactions.

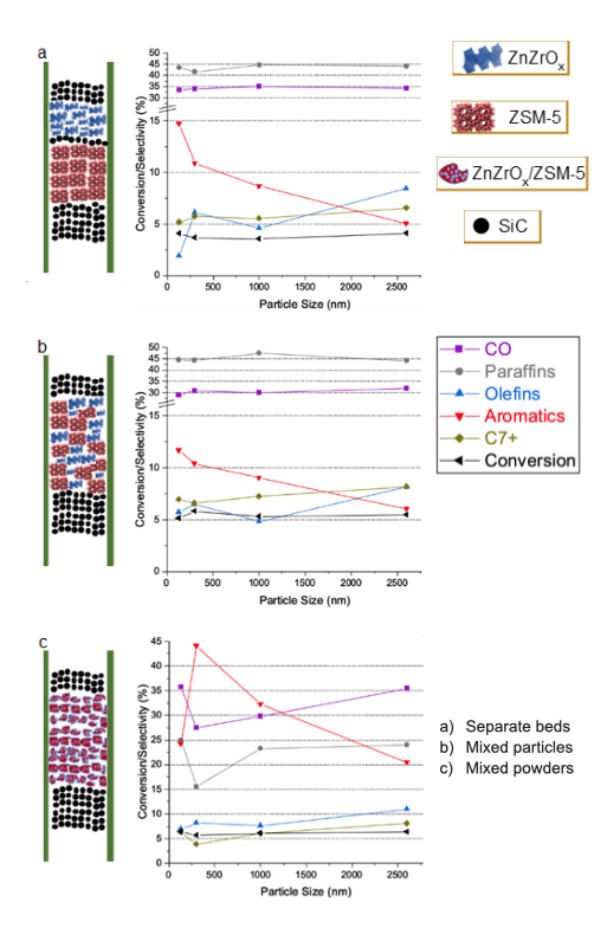


Figure 29: Reaction performance at different H-ZSM-5 crystal sizes at different bed structures. Reaction conditions are:  $T = 320 \,^{\circ}\text{C}$ , WHSV = 7200 mL/g<sub>cat</sub>/h,  $P = 4 \,\text{MPa}$ ,  $\text{CO}_2/\text{H}_2 = 3$ , ZnZrO/H-ZSM-5 = 1/2, Si/Al = 300

A similar increasing trend in aromatics selectivity is observed in the mixed powders orientation when the crystal size of ZSM-5 reduces from 2600 nm to 300 nm. The aromatics selectivity can be as high as 44% when the ZSM-5 crystal size is 300 nm; this value is among the highest reported in the literature thus far. However, unlike the two other cases, in the mixed powders orientation the aromatic selectivity reduces significantly as the ZSM-5 crystal size reduces from 300 nm to 100 nm. Besides that, while the CO selectivity for the first two orientations is always independent of the ZSM-5 crystal size, this value varies significantly at different crystal sizes for the mixed powders orientation. This is not expected, since the only parameter that is changed is ZSM-5 crystal size, which is not considered as a dominantly active site for the RWGS reaction compared to ZnZrO. This is further evidence that some other factor, probably related to ZnZrO, also plays a role in these experiments.

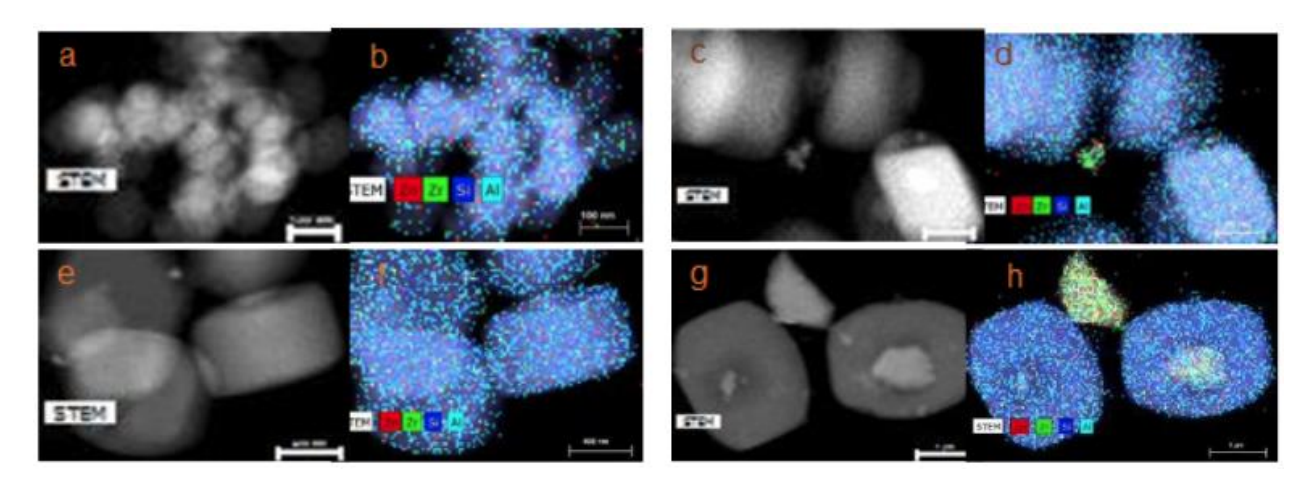


Figure 30: STEM images and elemental mapping of a,b) ZnZrO/ZSM-5-300-120; c,d) ZnZrO/H-ZSM-5-300-300; e,f) ZnZrO/H-ZSM-5-300-120; g,h) ZnZrO/ZSM-5-300-3000

For a better understanding of these observations, different microscopy and spectroscopy techniques were employed for each mixed powder catalyst. The ZSM-5 crystals are known for their lamellar structure with hexagons; however, crystals with irregular shapes and extra-framework materials can form during the ZSM-5 synthesis as well.<sup>47</sup> Since the intention of this study was to synthesize ZSM-5 materials that can provide a uniform range of crystal sizes, it is expected that the irregular shapes of ZSM-5 are minimized in the product batch. TEM images coupled with EDS analysis were employed at multiple snapshots of each catalyst to confirm that most of the particles with irregular shapes are ZnZrO particles (Figure 30). Upon examining the mixed powders at a relatively larger scale using SEM images, it was noticed that for the ZSM-5-300-2600 catalyst, the ZnZrO particles tended to attach to the surface of ZSM-5 crystals (Figure 31e,f). This tendency reduces upon going to smaller ZSM-5 crystals. For the ZSM-5-300-300 catalyst, it is noticed that along with small ZnZrO<sub>x</sub> particles attaching to ZSM-5 crystals, there are segregated particles of ZnZrO<sub>x</sub> that are surrounded by ZSM-5 crystals (Figure 31c,d). Upon further reducing the ZSM-5 crystal to 100 nm, most of the ZnZrO<sub>x</sub> particles are segregated and little to no small ZnZrO<sub>x</sub> can be observed (Figure 31a,b).

To further approve and quantify this observation, large scale SEM/EDS analysis was performed to measure and quantify the ZnZrO particle sizes based on the elemental mapping for each powder mix. The results of these measurements are shown in Figure 32. For all mixed powder catalysts, the ZnZrO particle sizes vary significantly from the nm range to  $\mu$ m range, some are attached to ZSM-5 crystals and have formed small particles, while others are segregated into bigger particles. As ZSM-5 crystal size decreases, a consistent increasing trend in ZnZrO particle size can be observed. It is hypothesized that bigger crystals of ZSM-5 provide a more effective surface on which metal oxides can attach. Therefore, smaller particles are more favored at larger zeolite crystal sizes. In contrast, smaller crystals of ZSM-5 do not provide the minimum surface area required for ZnZrO particles to attach, and segregation to bigger particles is observed in those cases.

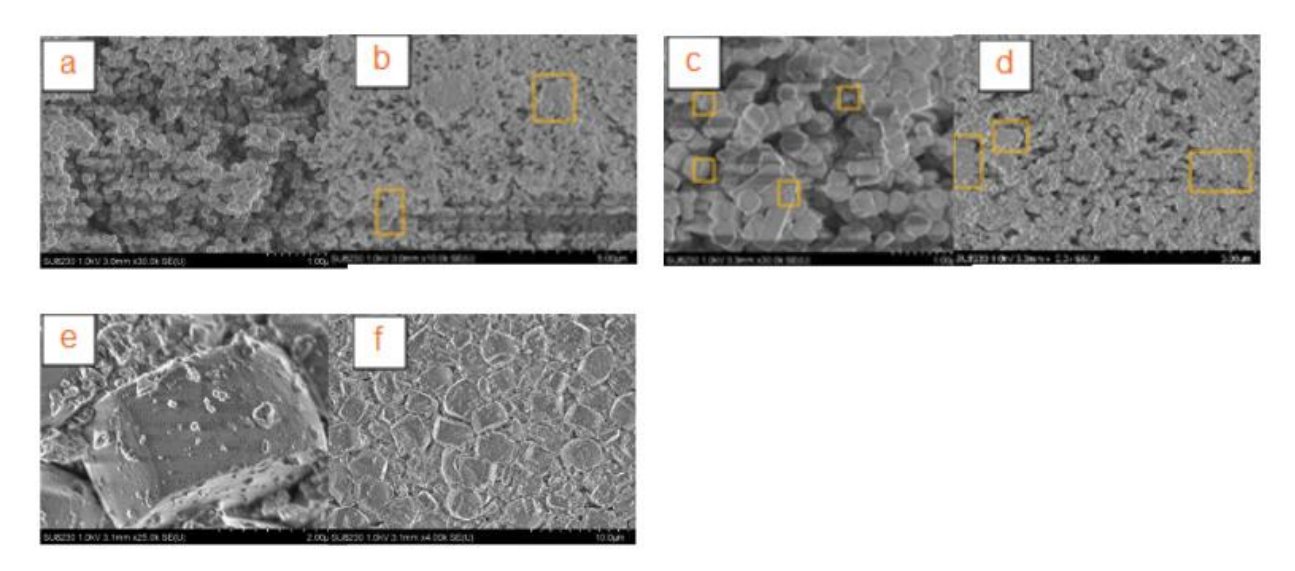


Figure 31: Small scale and large scale SEM images of a,b) ZnZrO/ZSM-5-300-120; c,d) ZnZrO/ZSM-5-300-300; e,f) ZnZrO/ZSM-5-300-3000. Highlighted rectangles in b-d point to ZnZrO particles

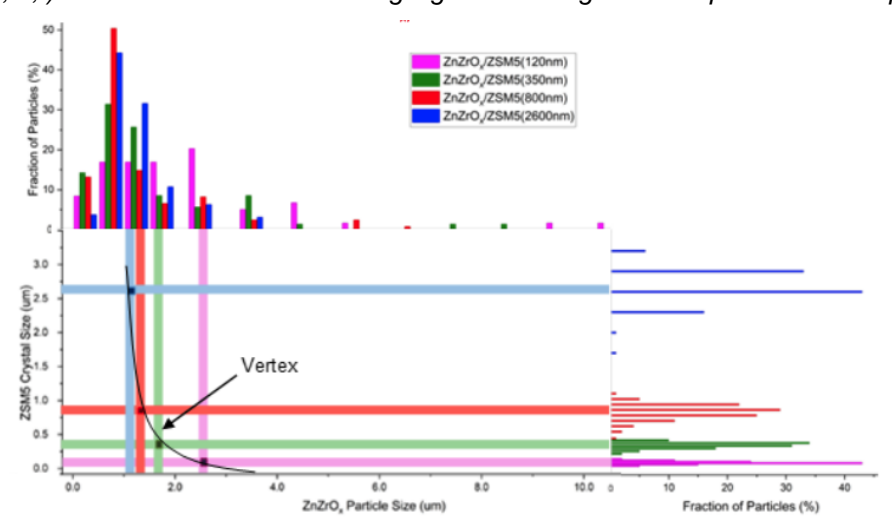


Figure 32: Correlations between ZnZrO and ZSM-5 particle sizes in the mixed powder catalysts

Bifunctional catalysts such as the ZnZrO/ZSM-5 catalyst provide the optimum performance when the interfacial surface area between the two functionalities is maximized. This interfacial surface area is directly proportional to the particle sizes of both functionalities. The hyperbolic plot of ZnZrO particle size against ZSM-5 crystal size in Figure 32 indicates that the most optimal interaction of the two sites is obtained at its vertex (closest point to (0,0), Figure 32), where the combination of the two particle sizes is at their minimum value. Therefore, this point has the highest aromatics selectivity.

#### D. Conclusions

H-ZSM-5 of varying sizes were tested in different patterns of fixed bed arrangements. Of the 3 patterns considered, mixed particle arrangement shows the best performance for CO<sub>2</sub> hydrogenation for high selectivity for aromatics production. However, in case of mixed particle arrangement, it was found that an optimum H-ZSM-5 particle size exists

where the selectivity for aromatics for CO<sub>2</sub> hydrogenation is highest. This is based on the interaction between the 2 catalysts and the optimal distance between ZnZrO and H-ZSM-5 is observed when H-ZSM-5 of 300 nm is used. Hence, ZnZrO/H-ZSM-5 has the best performance catalyst combination with respect to high aromatics selectivity.

# IX. Task 7.0 – Computational screening model development

# A. Goals and Objectives of the Task

Using results from Task 5.0, a high-throughput screening model will be developed to determine rates and selectivities as a function of metal(s), gas composition, and reaction-diffusion length scales.

<u>Subtask 7.1 – Extend to other metals</u>: Complete the necessary DFT calculations for intermediates/transition states (TS) on other metals (e.g. Rh, Pt, Pd, Au, Ag).

<u>Subtask 7.2 – Construct screening model</u>: Use CatMAP to construct scaling relations and build a microkinetic screening model.

<u>Subtask 7.3 – Computationally identify target catalysts</u>: Calculate rates as a function of gas composition and descriptor(s) (C/O binding energy) and identify promising singlemetal catalysts.

# B. Background and Research Methods

To extend the microkinetic model to the additional transition metals, different adsorbate-adatom and metal-sites pairs DFT energies need be computed, e.g. carbon and oxygen as adatoms in methanol, and top, bridge and hollow sites in Cu(111). The generation of new initial structures to be simulated is a time-consuming process and prone to user bias, since the DFT simulation consists of an iterative non-linear optimization problem, which can be non-convex, and therefore different initial structures might lead to different final ionic ground-states. With that in mind, we created a series of routines that, given transition-metal slabs and converged radical structures, generate the ensemble of all possible combinations of radical-adatoms (all atoms, except hydrogen are considered) and pre-defined adsorption sites, based on an optimization criterion that maximizes the distance between any slab atom and all other non-adatom radical components.

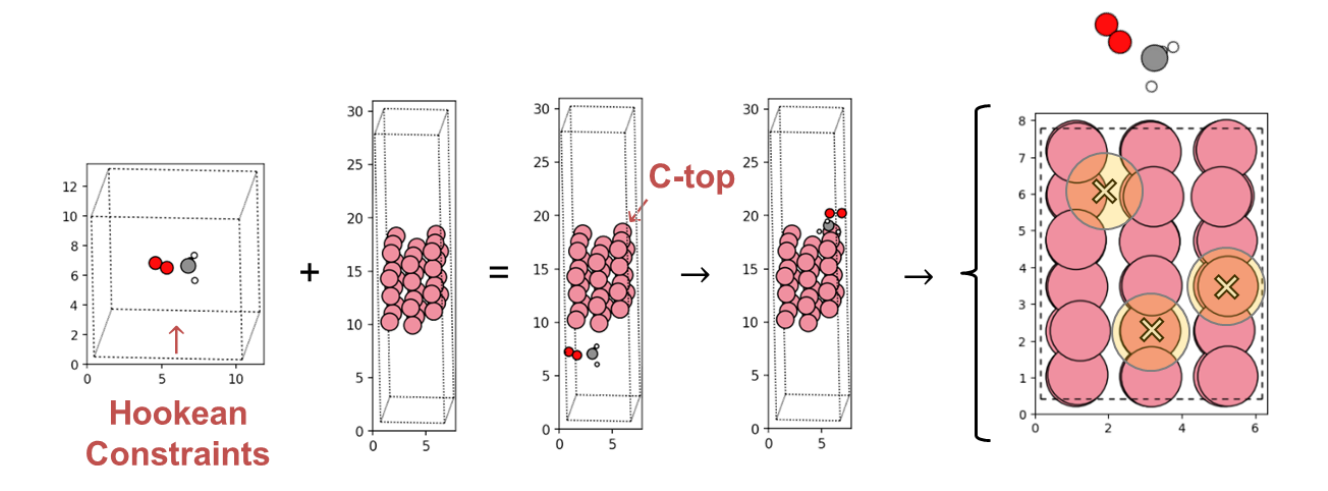


Figure 33. Automatic adsorbate-slab pair generation diagram.

Figure 33 illustrates the automatic adsorbate-slab pair generation routine, in which: (i) pre-converged metal-slab and radical structures are provided, (ii) the routine iterates over all adatoms and metal sites where it fixes the adatom position as pivot at an arbitrary distance from the surface and (iii) a global optimization algorithm is used to maximize the distance between other non-adatom atoms in the radical and the metal atoms on the surface, and finally (iv) simulations are submitted to the computer cluster.

#### C. Results and Discussions

### (i) Subtask 7.1 – DFT calculations of other TMs

DFT calculations of the same intermediate species as those in the current microkinetic model will be also carried out for rhodium, platinum, palladium, gold and silver slabs. As proposed in Subtask 5.2, to speed up the computational catalyst screening process, BEP scaling relations were also be used for these new metals for the prediction of transition state energies. Therefore, the framework used for Subtask 5.2 were extended to Subtask 7.1.

Single-metal DFT calculations for adsorbates on palladium, gold and silver were completed, as shown in Figure 34, where *nsp* refers to non-spin polarized DFT calculations. In parallel, cobalt calculations were discontinued due to convergence issues and the additional computational cost associated with its magnetic properties; however, their results would have been only incremental from the standpoint of developing the extended microkinetic model.

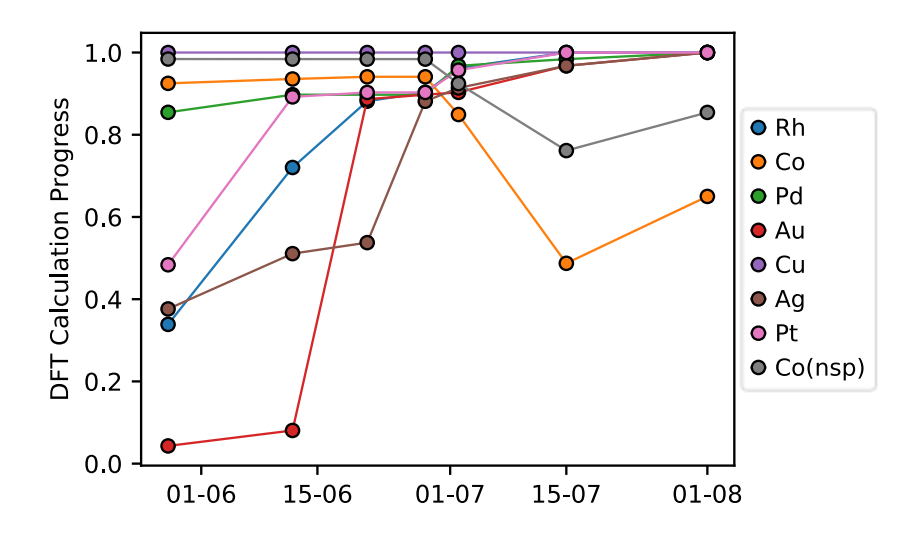


Figure 34. DFT calculations progress for additional transition-metal catalysts in Q7.

Fast progress in DFT simulations was only possible through the reduction of the total number of simulations to be run by detecting symmetries in the molecules or radicals to be positioned on different catalyst active sites, e.g. hollow, top, bridge, etc. DFT simulations were run in a series of calculations with improving fidelity, where convergence criteria are subsequently tightened leading to an improved trade-off between computational accuracy and walltime.

Symmetry detection was carried out through eigenspectrum analysis of molecules/radicals atom-distance matrix, as shown in the anecdotal example Figure 35. In such example, the biphenyl molecule atom-distance matrix is calculated, and the 16 adatoms (in this case, only carbon atoms) are classified according to the similarities between theirs scores on the first principal component  $(\overrightarrow{v_0})$  given a difference threshold. For this anectodal example, off of the 16 carbon atoms, there are only 4 unique groups, reducing the total number of simulations to be run by a factor of 4.

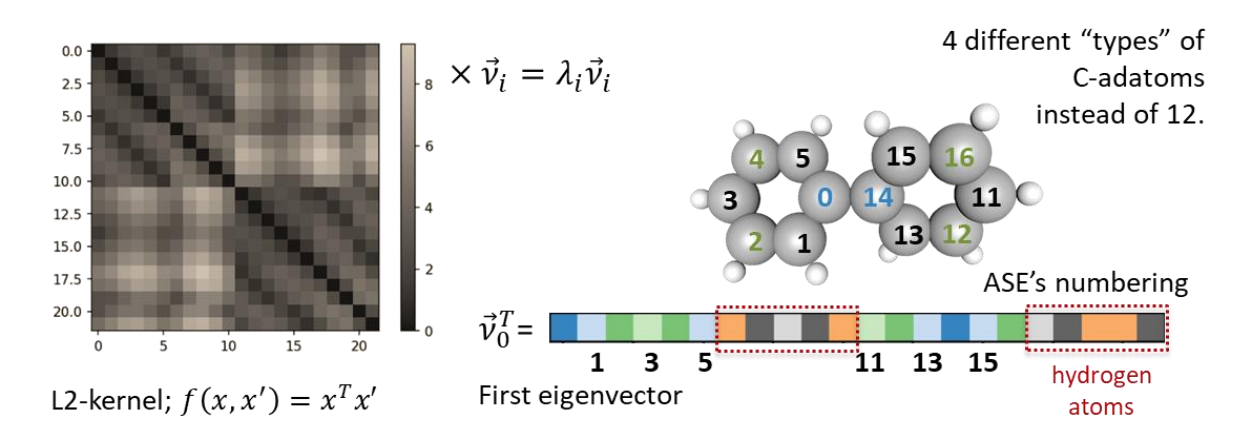


Figure 35. Adsorbate/radical symmetry detection: distance matrix (L2-kernel) eigendecompositions (left) and classification according to the projection on the first principal component (right).

The symmetry detection routine can hence be used as a pre-processing step in the generation of adsorbate-slab pairs, which is illustrated in Figure 33. A single element of an adatom group is therefore picked and positioned over each sampled active site at a fixed distance, and the distance between all other molecule/radical atoms from the surface is maximized using a global optimization algorithm with the adatom as pivot point.

# (ii) Subtask 7.2 - Construct screening model

A general pipeline for the utilization of literature-based Brønsted–Evans–Polanyi, BEP-type, scaling relationships was developed. DFT energies for the fully converged Cu(111) transition-metal DFT simulation set were used in comparison to those of Grabow's paper. To adopt BEP-type scaling relations to the Grabow's original mechanism, assumptions had to be made concerning concerted surface reactions, i.e. hypothesizing a set of elementary steps for which BEP parameters are available.

In the preliminary version of the microkinetic model (MKM), global literature-reported Brønsted–Evans–Polanyi (BEP) scaling relationships<sup>41–43</sup> were utilized to build the mapping between DFT-derived reaction energies and their respective transition state energies (reaction barriers) for the studied transition metal catalysts. For the previous BEP references, as a general approximation, only global hydrogenation and non-hydrogenation BEP correlations were included in the estimation of transition state energies. In the refined BEPs, scaling relations are assigned to the majority of reactions that involve carbon, oxygen and hydrogen and their various groups, e.g. C-O, C-OH, CO-O, HO-H, CO-CH. <sup>41–43,48</sup>

The Cu(111) refined potential energy diagram along with those of the remaining transition metals is shown in Figure 36. As previously, concerted surface reactions were algebraically broken down into potential lower-energy paths within the reaction network. The highest BEP-derived energy barrier along the reaction path was initially considered to be the upper-bound estimate for the transition state energy of such non-elementary reactions. Nevertheless, concerted steps involving CO-assisted hydrogenation, i.e. HCO\*, were suppressed from the model, since the hydrogen reservoir approximation is

utilized and, therefore, H<sub>2</sub> adsorption does not compete with other adsorbates, and direct protonation pathways are not hindered by high coverage.

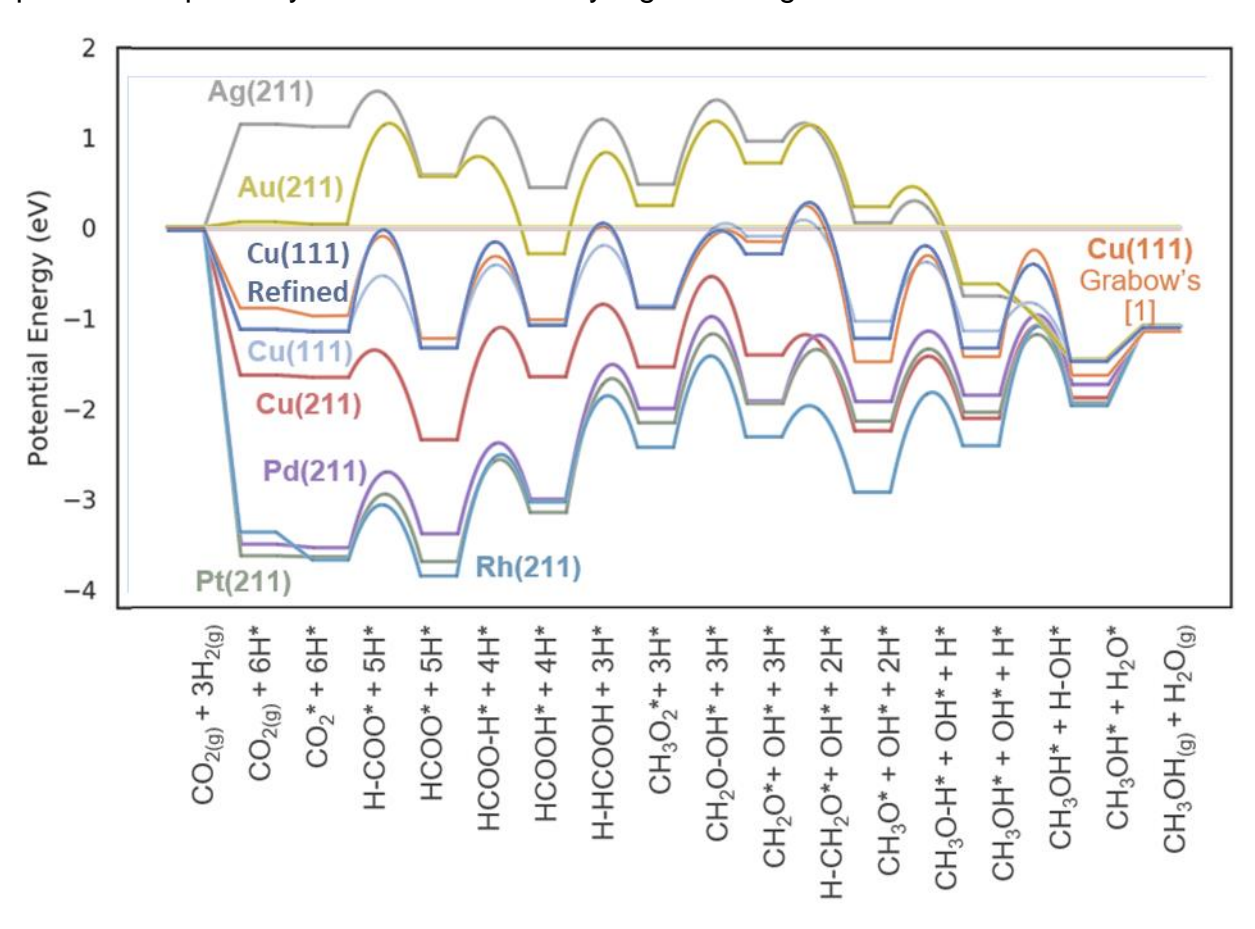


Figure 36. CO<sub>2</sub> hydrogenation potential energy diagram for different transition metals with Cu(111) refined BEP scaling relations.

From the results in Figure 36, it becomes clear that by selecting appropriate BEP relations, especially for reactions involving HO-H cleavage, leads to a better match between fully NEB-calculated DFT energies and their estimates from scaling relations. While the previous difference for the Cu(111) set would vary up to 0.2 eV, the refined set of scaling relations brings this value to below 0.1 eV. As done in Q8, CatMAP will be further utilized to update the overall binding energies with the formation energy approach. The linear scaling coefficients from the previous report will be updated accordingly to reflect the changes in transition states formation energies with the refined BEP scaling relations set.

It is worth noting that generally, even for complex reaction mechanisms, only a few of the elementary steps govern catalytic activity. Therefore, with the utilization of "degree of rate control" or other sensitivity analysis methods, one can refine scaling-relations based microkinetic models by using first principles methods for more accurate estimation of transition state energies of rate-controlling steps.

Furthermore, CatMAP was utilized to create an overall binding energies linear mapping under the so-called 'formation energy approach', that allows the interpolations of the binding energies of adsorbed intermediate species and transition states in terms of those of CO\* and O\*, adsorbed carbon monoxide and atomic oxygen. Table 3 conveys the regression coefficients for the derived linear relationships between adsorbates (intermediate species) and the binding energies of the selected descriptors. Similarly, in Table 4, there are the regression coefficients for the linear mappings between binding energy descriptors and transition-states formation energies.

Table 3. Linear Scaling Relations for Adsorbates in terms of CO\* and O\* binding energies, Eco and Eo.

Adsorbate	Binding Energy (eV)	Adsorbate	Binding Energy (eV)
CH2CO	0.88×E <sub>CO</sub> - 2.52	СОН	1.67×E <sub>CO</sub> + 1.71
CH2OH	0.61×E <sub>CO</sub> + 0.07×E <sub>O</sub> - 0.85	СООН	$0.48 \times E_{CO} + 0.26 \times E_{O} + 0.01$
CH2O	0.11×E <sub>CO</sub> + 0.12×E <sub>O</sub> - 1.01	С	$1.78 \times E_{CO} + 0.29 \times E_{O} + 0.93$
CH2	1.0×E <sub>CO</sub> - 1.03	H2CO2	0.75×E <sub>○</sub> - 0.94
CH3CH2OH	0.06×E <sub>CO</sub> + 0.1×E <sub>O</sub> - 5.61	H2COOCH3	0.5×E <sub>0</sub> - 4.02
СНЗСНОН	0.7×E <sub>CO</sub> - 3.8	H2O	$0.04 \times E_{CO} + 0.11 \times E_{O} + 0.27$
СНЗСНО	0.14×E <sub>CO</sub> + 0.21×E <sub>O</sub> - 4.81	НСОН	1.15×E <sub>CO</sub> + 0.43
CH3CO	0.77×E <sub>CO</sub> + 0.03×E <sub>O</sub> - 3.44	НСООСН3	0.12×E <sub>CO</sub> + 0.06×E <sub>O</sub> - 3.06
CH3O2	0.51×E <sub>0</sub> - 1.35	НСООН	0.19×E <sub>CO</sub> + 0.1×E <sub>O</sub> - 0.52
СНЗОН	$0.04 \times E_{CO} + 0.12 \times E_{O} - 2.36$	HCOO	0.54×E <sub>0</sub> - 1.67
CH3O	0.54×E <sub>O</sub> - 2.82	HCO	0.9×E <sub>CO</sub> + 0.32
CH3	0.52×E <sub>CO</sub> - 2.45	O2	$0.53 \times E_{CO} + 0.06 \times E_{O} + 6.51$
CHCO	0.41×E <sub>CO</sub> + 0.22×E <sub>O</sub> - 3.28	ОН	0.49×E <sub>0</sub> - 0.14
СН	$1.45 \times E_{CO} + 0.03 \times E_{O} + 0.2$	Н	$0.39 \times E_{CO} + 0.06 \times E_{O} + 0.11$
CO2	0.02×E <sub>CO</sub> + 0.08×E <sub>O</sub> - 0.21		

Table 4. Linear Scaling Relations for Transition States (TS) in terms of CO\* and O\* binding energies,  $E_{CO}$  and  $E_{O}$ .

TS	Binding Energy (eV)	TS	Binding Energy (eV)
C-H	$1.67 \times E_{CO} + 0.13 \times E_{O} + 1.19$	H-CO	$1.05 \times E_{CO} + 0.02 \times E_{O} + 0.98$
C2H6-	0.9×E <sub>CO</sub> - 5.0	H-HCOH	$0.9 \times E_{CO} + 0.07 \times E_{O} + 0.31$
CH-CO	0.96×E <sub>CO+</sub> 0.17×E <sub>O-</sub> 1.3	H-HCOOCH3	$0.16 \times E_{CO} + 0.38 \times E_{O} - 2.95$
CH-H	$1.26 \times E_{CO} + 0.03 \times E_{O} + 0.12$	Н-НСООН	$0.18 \times E_{CO} + 0.4 \times E_{O} - 0.33$
CH2-H	$0.79 \times E_{CO} + 0.02 \times E_{O} - 1.24$	H-HCOO	$0.12 \times E_{CO} + 0.7 \times E_{O} - 0.4$
CH2-O	$0.35 \times E_{CO} + 0.36 \times E_{O} + 0.03$	H-HCO	$0.48 \times E_{CO} + 0.1 \times E_{O} + 0.17$
CH2CO-H	$0.93 \times E_{CO} + 0.04 \times E_{O} - 2.39$	H-OH	$0.15 \times E_{CO} + 0.25 \times E_{O} + 0.91$
CH2O-H	$0.58 \times E_{CO} + 0.1 \times E_{O} - 0.13$	H2CO-O	$0.03 \times E_{CO} + 0.85 \times E_{O} + 0.08$
CH2O-OCH2	$0.15 \times E_{CO} + 0.11 \times E_{O} - 1.74$	НСО-Н	1.2×E <sub>CO+</sub> 0.02×E <sub>O+</sub> 1.16
CH2O-OCH3	$0.03 \times E_{CO} + 0.54 \times E_{O} - 2.93$	HCO-OH	$0.38 \times E_{CO} + 0.21 \times E_{O} + 0.7$
CH2O-OH	$0.03 \times E_{CO} + 0.53 \times E_{O} - 0.26$	HCO-O	0.24×E <sub>CO+</sub> 0.67×E <sub>O-</sub> 0.1
CH3-CO	$0.97 \times E_{CO} + 0.02 \times E_{O} - 2.13$	HCOH-O	$0.45 \times E_{CO} + 0.35 \times E_{O} + 0.77$
CH3-OH	0.48×E <sub>CO+</sub> 0.52×E <sub>O-</sub> 1.9	HCOO-CH3O	-0.05×E <sub>CO+</sub> 1.09×E <sub>O-</sub> 2.94
CH3CH2O-H	$0.38 \times E_{CO} + 0.09 \times E_{O} - 4.28$	HCOO-HCO	$1.02 \times E_{CO} + 0.35 \times E_{O} + 0.18$
CH3CH2OH-	_5.11	НСОО-Н	0.25×E <sub>CO+</sub> 0.26×E <sub>O-</sub> 0.12

СН3СНО-Н	0.65×E <sub>CO+</sub> 0.08×E <sub>O-</sub> 3.35	O-CO	0.28×E <sub>CO+</sub> 0.33×E <sub>O+</sub> 0.88
СН3СО-Н	$0.46 \times E_{CO} + 0.17 \times E_{O} - 3.62$	O-HCO	$0.9 \times E_{CO} + 0.99 \times E_{O} + 0.89$
CH3O-HCO	$0.97 \times E_{CO} + 0.34 \times E_{O} - 1.2$	O-H	$0.12 \times E_{CO} + 0.67 \times E_{O} + 0.67$
CH3O-H	$0.15 \times E_{CO} + 0.27 \times E_{O} - 1.73$	0-0	$0.39 \times E_{CO} + 0.59 \times E_{O} + 5.79$
CH3O-O	$0.16 \times E_{CO} + 0.66 \times E_{O} - 0.18$	O2-	+ 7.59
CH4-	$0.76 \times E_{CO} + 0.05 \times E_{O} - 2.42$	OCH-CH2O	1.01×E <sub>CO+</sub> 0.22×E <sub>O-</sub> 0.32
CHCO-H	$0.86 \times E_{CO} + 0.09 \times E_{O} - 1.99$	OCH-HCOOH	$1.06 \times E_{CO} + 0.21 \times E_{O} + 0.65$
СО-Н	$1.58 \times E_{CO} + 0.02 \times E_{O} + 1.95$	OH-HCO	$0.96 \times E_{CO} + 0.33 \times E_{O} + 1.4$
CO-OH	$0.62 \times E_{CO} + 0.32 \times E_{O} + 1.01$	OH-OH	$0.02 \times E_{CO} + 1.05 \times E_{O} + 0.66$
СОО-Н	$0.46 \times E_{CO} + 0.22 \times E_{O} + 0.7$	OOCH-HCO	$0.94 \times E_{CO} + 0.62 \times E_{O} + 0.27$
COOH-OH	$0.38 \times E_{CO} + 0.61 \times E_{O} + 0.79$	H2-	$0.13 \times E_{CO} + 0.02 \times E_{O} + 0.21$
H-CH2OH	$0.34 \times E_{CO} + 0.12 \times E_{O} - 1.12$	H-COOH	$0.4 \times E_{CO} + 0.17 \times E_{O} + 0.41$
H-CH2O	$0.16 \times E_{CO} + 0.42 \times E_{O} - 1.49$	H-COO	0.13×E <sub>CO+</sub> 0.42×E <sub>O-</sub> 0.46

The overall mean absolute error (MAE) for the linear model is below 0.1 eV, which is a reasonable value since the MAE for the DFT-based binding energies given the current exchange correlation functional (PBE) is around 0.2 eV. The error distribution for intermediate and transition states is portrayed in Figure 37.

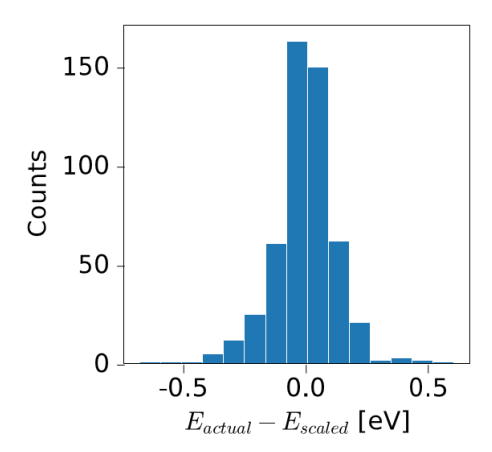


Figure 37. Error distribution between predicted (scaled) and actual transition states and adsorbate binding energies

# (iii) Subtask 7.3 - Computationally identify target catalysts

The main elementary steps from Medford et. al.<sup>49</sup> along the CH<sub>4</sub> pathways for the formation of methane in Rh-like catalysts were included into the microkinetic model. Since the intermediate species in the CH<sub>4</sub> pathway were already part of the model, no additional DFT simulation had to be carried out. Transition state energies were estimated with the refined set of BEP scaling relations. The updated volcano plots (activity maps) are currently being calculated and they will be included in the next report.

The identification of target catalysts is guided by the screening model developed in Subtask 7.2. It consists of finding regions in the oxygen and carbon binding energies (descriptors) space that favors the formation of methanol to the detriment of methane. Figure 38 shows volcano plots for the turnover frequency of methane and methanol as a

function of the selected binding energy descriptors at reaction conditions in the high end of activity toward methanol. The identification of Cu as the best methanol catalyst is consistent with the well-known Cu-based industrial catalysts. However, the methane formation activity of more reactive metals, such as Rh, is significantly underestimated.

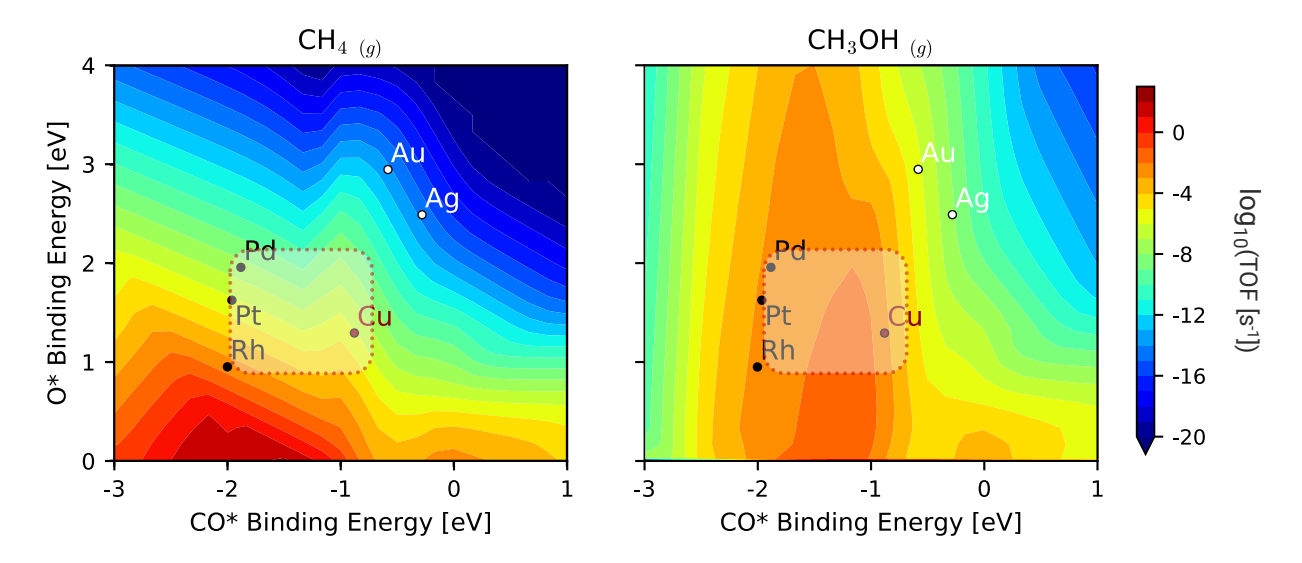


Figure 38. Descriptor-based volcano plot for methane and methanol turn-over frequencies at 700 K, 50 bar and CO<sub>2</sub>:CO:H<sub>2</sub> = 0.05:0.05:0.90 (molar).

The bimodal optima in activity toward methane at different CO\* binding energies in Figure 38 is a result of mechanistic assumptions, as proposed by Medford et. al.  $^{49}$ , where for rhodium-like catalysts, which are known to be suitable catalysts for methanation, methane is formed by C-O cleavage at the four-fold sites, followed by diffusion to the terrace site and successive hydrogenation of CH<sub>x</sub> intermediates. At the static condition at which the volcano plots Figure 38 were evaluated, potential catalysts (e.g. alloys) would lie in the region where there is a compromise between methanol synthesis and methanation, i.e. in the quadrant encompassing Pd, Pt, Rh and Cu.

#### D. Conclusions

<u>Subtask 7.1 – DFT calculations of other TMs</u>: DFT calculation for non-magnetic metallic catalysts. Additional metals may be included into the model to widen its coverage in the descriptor space. Incremental and/or refinement DFT calculations steps may be performed in future developments to allow the propagation of uncertainties, with the utilization of BEEF-vdW exchange correlation functional without substantially affecting the current results.

<u>Subtask 7.2 – Construct screening model</u>: The thermochemistry (formation energies) for the different single-metal catalysts has been completed. The underlying linear models for the construction of the set of scaling relations-based microkinetic models has been built.

<u>Subtask 7.3 – Computationally identify target catalysts:</u> A region for potential catalyst of interest in the binding-energy descriptor domain is conveyed in Subtask 7.3 in terms of trade-off between methanol synthesis and methanation reaction.

# X. Task 8.0 – Experimental testing of chemical mixtures (hydrogenation catalyst supported on zeolite catalyst)

## A. Goals and Objectives of the Task

Using Task 6.0 as a basis, we will further decrease the reaction-diffusion length scales by synthesizing materials with metal nanoparticles impregnated within/on the zeolite domain.

<u>Subtask 8.1 – Establish synthesis procedures:</u> Synthesis and characterization of ZSM5 structures with appropriate nanoparticles including ZnZrO nanoparticles imbedded within or supported on the framework will be completed.

<u>Subtask 8.2 – Experimental evaluation of intimate mixing of acid and metal domains:</u> Steady-state conversion testing, measuring rates and selectivities to compare to the physical mixtures synthesized in Task 6.0 will be conducted.

# B. Background and Research Methods

Literature has been reviewed for the most efficient method for the synthesis of chemical mixtures of the hydrogenation and aromatization catalysts. The ion exchange method cannot be used as an efficient method since the ratio of metal oxides to zeolite used is 1:2 and, considering the low acid density of H-ZSM-5 used for this reaction, there are not enough ion exchange sites in the zeolite framework to exchange with the desired value of Zn and Zr. Therefore, the wetness impregnation method was used for chemically embedding ZnZrO<sub>x</sub> particles on H-ZSM-5 structure at this time.

The H-ZSM-5 catalyst with a Si/Al ratio of 300 and crystal size of 300 nm was chosen for this synthesis. Initially 1 g of this catalyst was placed in a flask with 50 mL of deionized water while stirring vigorously. A mixture of 0.18 g of  $Zn(NO_3)_2 \cdot 6H_2O$  and 1.63 g of  $ZrO(NO_3)_4 \cdot xH_2O$  (x  $\approx$  6) was dissolved in 50 mL of deionized water and then added to the H-ZSM-5 solution. The mixture was stirred for another 6 hours and then the water was removed from it using a rotary evaporator at 50 °C. The sample was dried overnight and then calcined at 500 °C for 5 hours.

The catalyst was then characterized by means of NH<sub>3</sub>-TPD, XRD, SEM. The WI ZnO-ZrO<sub>2</sub>/H-ZSM-5 catalyst will be tested at the temperature of 320 °C, pressure of 600 psi, WHSV of 7,200 mL/g<sub>catalyst</sub>/h and the feed with the H<sub>2</sub>/CO<sub>2</sub> ratio of 3 to complete this subtask. The activities on this subtask will be resumed during the next quarters.

#### C. Results and Discussions

<u>Subtask 8.1 – Establish synthesis procedures:</u> The obtained sample was analyzed for the presence of ZnO and ZrO<sub>2</sub> crystals and their impact on the H-ZSM-5 crystal structure and

acidity of the catalyst using XRD, SEM, and NH<sub>3</sub>-TPD analysis. During these analyses, the chemically embedded wetness impregnation catalyst (WI) was compared to the physically mixed catalyst (PM). The NH<sub>3</sub>-TPD results in Figure 39 show that WI and PM catalysts share similar acid site desorption temperatures. These acid sites are a combination of those belonging to H-ZSM-5 (at approximately 150 °C and 320 °C) and ZnO-ZrO<sub>2</sub> (at approximately 125 °C and 250 °C, according to the literature<sup>19,20,25</sup>) catalysts. The deconvolution of these peaks for the mixed catalysts is a challenge due to the presence of the acid sites in similar regions and the low acid site density of the H-ZSM-5 catalyst used. It can be observed that the density of acid sites in the WI catalyst is twice as much of that of the PM catalyst. This is probably due to the formation of agglomerates of ZnO-ZrO<sub>2</sub> particles in the PM catalyst, which reduces the overall available surface area of ZnO-ZrO<sub>2</sub> and reduces its surface acidity.

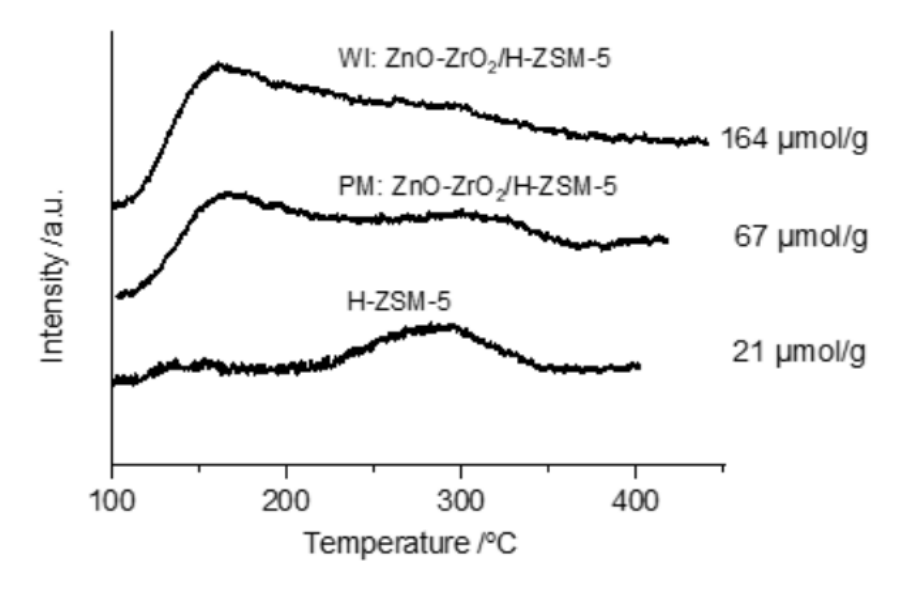


Figure 39: NH<sub>3</sub>-TPD of H-ZSM-5 catalyst and its mixture with ZnO-ZrO<sub>2</sub> catalyst via physically mixing (PM) and wetness impregnation (WI)

The results of the XRD analysis, shown in Figure 40, indicate that the chemically embedded metals maintain the same oxide crystal phase as that of the physically mixed and metal oxide catalysts. According to the literature, the metal oxide related peaks in the XRD are attributed to the tetragonal  $ZrO_2$  (t- $ZrO_2$ ), which forms upon the introduction of ZnO to  $ZrO_2$  catalyst.<sup>19,25</sup> Moreover, the ratio of the height of the largest ZSM-5 representing peak (at  $2\theta$ = 8.0 °) to that of the largest t- $ZrO_2$  peak (at  $2\theta$ = 30.5 °) is slightly larger in the PM catalyst compared to the WI catalyst (3.3 for the PM catalyst and 2.9 for the WI catalyst). This larger ZnO- $ZrO_2$  peak in the WI catalyst could be attributed to two main factors: (a) higher available surface of  $ZrO_2$  in the WI catalyst as they are chemically synthesized over ZSM-5, and (b) the higher coverage of ZSM-5 outer surface by  $ZrO_2$  in the WI impregnation catalyst, leading to the coverage of the surface and less crystallinity of ZSM-5 particles.

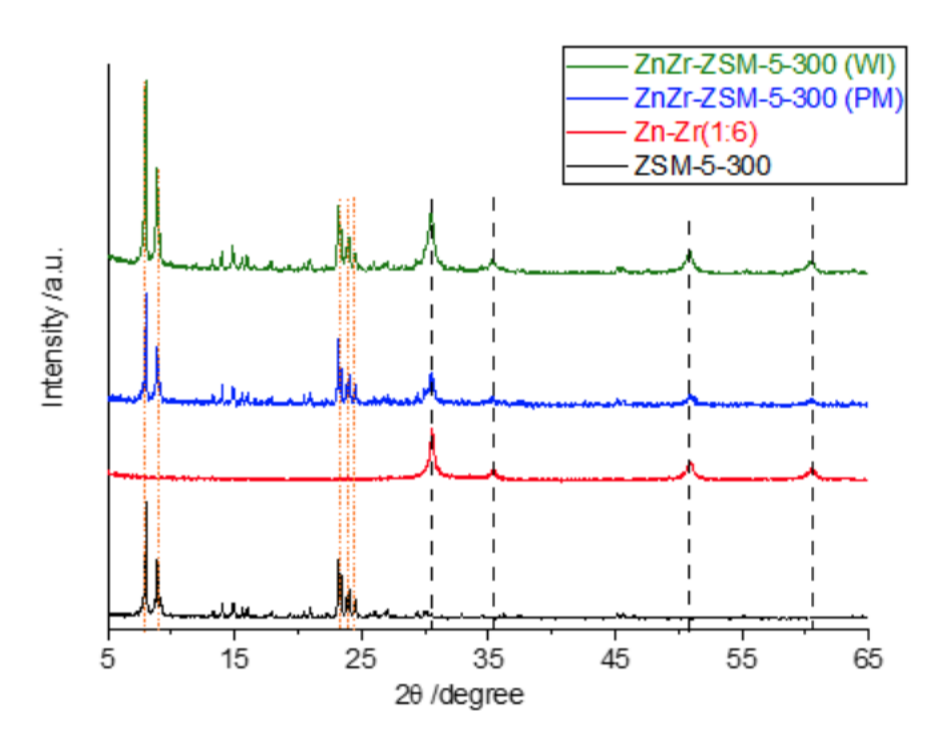
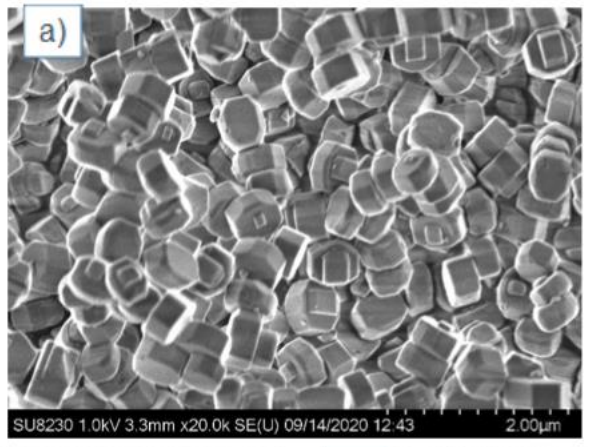
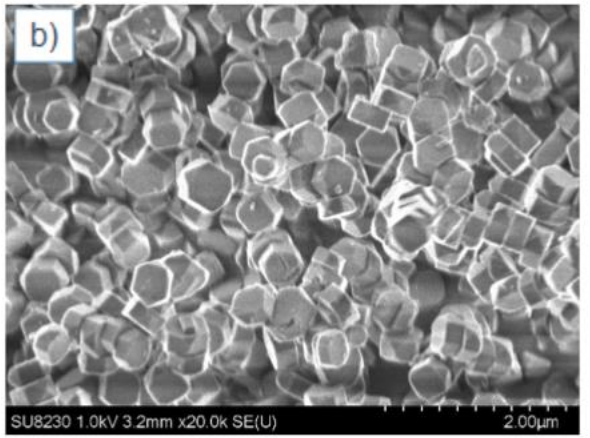


Figure 40: XRD spectra of ZSM-5 (black), ZnO-ZrO<sub>2</sub> (red), and their physical (blue), and chemical (green) mixture. Black vertical dashes identify the peaks representing tetragonal ZnO-ZrO<sub>2</sub> crystals and the orange vertical dashes show the location of main ZSM-5 peaks

The images obtained from the SEM analysis and their comparison with the physical mixture catalyst provide further evidence for the two points mentioned above. As shown in Figure 41, the crystal shape of the metal oxide-free ZSM-5 and the PM catalysts are very similar to each other. Small particles observed in the PM catalyst represent the ZnO-ZrO<sub>2</sub> particles. These particles are separate from ZSM-5 crystals and their size can vary in a wide range from a 20-200 nm. However, in the WI catalyst, the crystal structure of the ZSM-5 is largely affected by layers and particles of chemically embedded metal oxide. Unlike the PM catalyst, the metal oxides in the WI catalyst are not separate particles and are embedded to the crystal structure of ZSM-5.





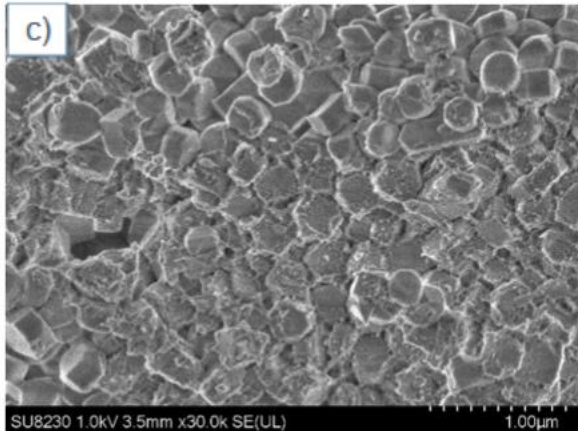


Figure 41: SEM images obtained from a) ZSM-5, b) PM, and c) WI catalysts

Subtask 8.2 – Experimental evaluation of intimate mixing of acid and metal domains: The wetness impregnation (WI) ZnZrOx/H-ZSM-5 catalyst was tested at the temperature of 320 °C, pressure of 600 psi, and a feed with the H<sub>2</sub>/CO<sub>2</sub> ratio of 3 to complete this Subtask. The results of the studies at different WHSVs are shown in Figure 42. As expected, the CO<sub>2</sub> conversion increases as the WHSV reduces. However, unlike the mixed powder catalyst case, an increasing trend in aromatics selectivity and decreasing trend in CO and paraffins selectivity is observed upon going to lower WHSVs. This is an interesting observation that shows that upon the chemical embedding of the ZnZrO<sub>x</sub> over ZSM-5 catalyst the reaction behavior is affected to a significant extent, suggesting impacts beyond simply reducing the diffusion path length. It could be hypothesized that during the WI synthesis, different types and quantities of metal oxide sites are formed. Also, since the WI occurs over the surface of ZSM-5 catalyst, a more exposed metal oxide on the surface of the catalyst is expected compared to the powder mixing catalysts.

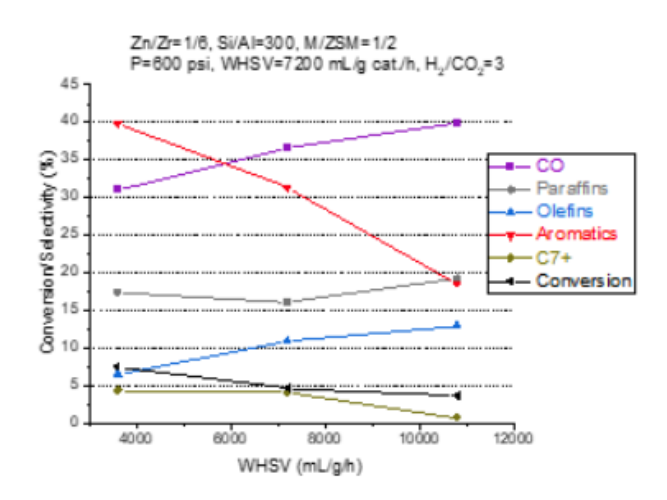


Figure 42: Performance of the ZnZrO(WI)-ZSM-5-300-300 catalyst at different WHSVs

Next, we analyzed the catalyst at different temperatures. The pressure was set at 600 psig, and a feed of H<sub>2</sub>/CO<sub>2</sub> ratio of 3 at a WHSV of 7200 mL/g/h was employed. The results of the studies at different temperatures are shown in Figure 43. The CO<sub>2</sub> conversion increases with increasing temperature as expected. While at lower range of temperatures the CO selectivity decreases with increasing temperature, it starts increasing again at higher temperatures. Unlike the mixed-powder catalyst, the WI catalyst shows a significant increase in selectivity of paraffins, while the olefin selectivity remains constant with an increase in temperature. The similar trends for the mixed-powder and WI catalyst suggest that the reaction pathways for the aromatics as well as CO as side products at the respective temperatures does not vary. However, the rate of aromatization on the WI catalyst is more than for the mixed-powder catalyst, which could point towards the short diffusion path lengths obtained when the metal oxides are embedded in the zeolite (as opposed to being physically mixed as separate particles).

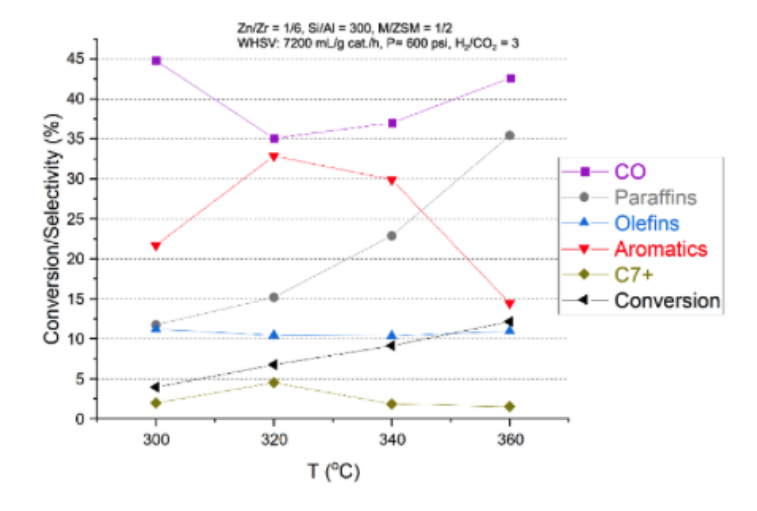


Figure 43: Performance of the ZnZrO(WI)-ZSM-5-300-300 catalyst at different temperatures

#### D. Conclusions

H-ZSM-5 was impregnated with ZnZrO to further minimize the distance between the 2 catalysts. While the aromatics production rate increased, the rate of paraffins production also increased leading to lower aromatics selectivity as compared to PM catalysts.

# XI. Task 9.0 - Computational screening of alloy compositions

# A. Goals and Objectives of the Task

The model developed in Task 7.0 will be utilized to determine selectivities of various metal alloy compositions.

<u>Subtask 9.1 – DFT on alloys</u>: Complete necessary DFT calculations of descriptors on binary transition metal (211) surfaces.

<u>Subtask 9.2 – Identify target alloy catalysts</u>: Use the descriptor-based micro-kinetic model from Task 7.2-7.3 to predict selectivity of alloys.

# B. Objectives and Research Methods

The adsorbate symmetry detection and adsorbate-slab pair simulation generation from Subtask 7.1 was utilized in Subtask 9.1 to minimize the number of simulations to be carried out for the binary alloys. The number of potential adsorption sites to be sampled increases for binary-alloy slabs. Furthermore, Subtask 7.3 serves as guidance to reduce the number of binary alloys to be assessed, since otherwise, if all possible binary alloys for the metals under study were considered, DFT simulations would be necessary for 21 different alloys. Since scaling-relations parameters are bulk-structure and facet-dependent, the alloys generated in this project are all constrained to the 211-facet of face-centered cubic (FCC) arrangements. The estimation of bimetallic-alloy surface thermochemistry follows five steps:

- i. FCC lattice constant (single parameter) optimization from DFT primitive unit-cell relaxation for different ratios of bimetallic alloys: 1:1, 3:1 and pure, as in Figure 44.
- ii. Utilization of the lattice constant and optimized unit-cell from (1) to create extended FCC bulk structures, and subsequently extract their 211-facet cleavages.
- iii. DFT simulation: ionic relaxation of the extended 211 slab, Figure 45.
- iv. Generation of the different combinations of adsorbate-adsorption site for bindingenergy descriptors.
- v. DFT simulation: ground state energy for binding-energy descriptors.

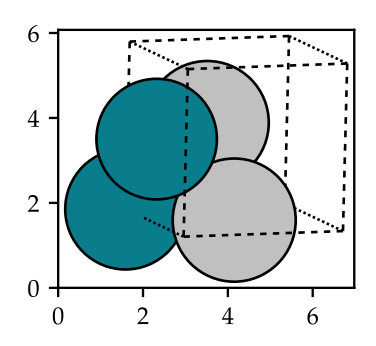


Figure 44. Bimetallic alloy cubic primitive cell example.

Steps (i) and (ii) have been automated. Thirty-five out the fifty DFT slab calculations of step (iii) had been completed by the end of Q7 and the remaining ones, some which presented convergence issues, are being analyzed case by case. Importantly, singlemetal primitive-cells are also computed to refine, if necessary, some of previously calculated single-metal DFT sets. Upon finalization of step (iii), the automation routines from Subtask 7.1 routines (adsorbate-slab pair simulation generation) were utilized to accelerate the combinatorial process of probing the bimetallic-alloy potential active sites.

#### C. Results and Discussions

# (i) Subtask 9.1 – DFT on alloys

The ionic relaxation step of routines previously devised underwent slight adjustments to (i) improve the numerical convergence, with the change of optimization algorithm, and (ii) to obtain more accurate bulk-structure lattice constants as compared to reported experimental values in literature with the selection of suitable pseudopotentials, i.e. from SG15 Optimized Norm-Conserving Vanderbilt (ONCV) to Ultrasoft (USP) pseudopotentials. The procedure for the estimation of bimetallic-alloy surface thermochemistry, more specifically for the 211 facets of FCC bulk-structures, remains the same in Q7, with the 211-FCC bimetallic surfaces shown in Figure 45.

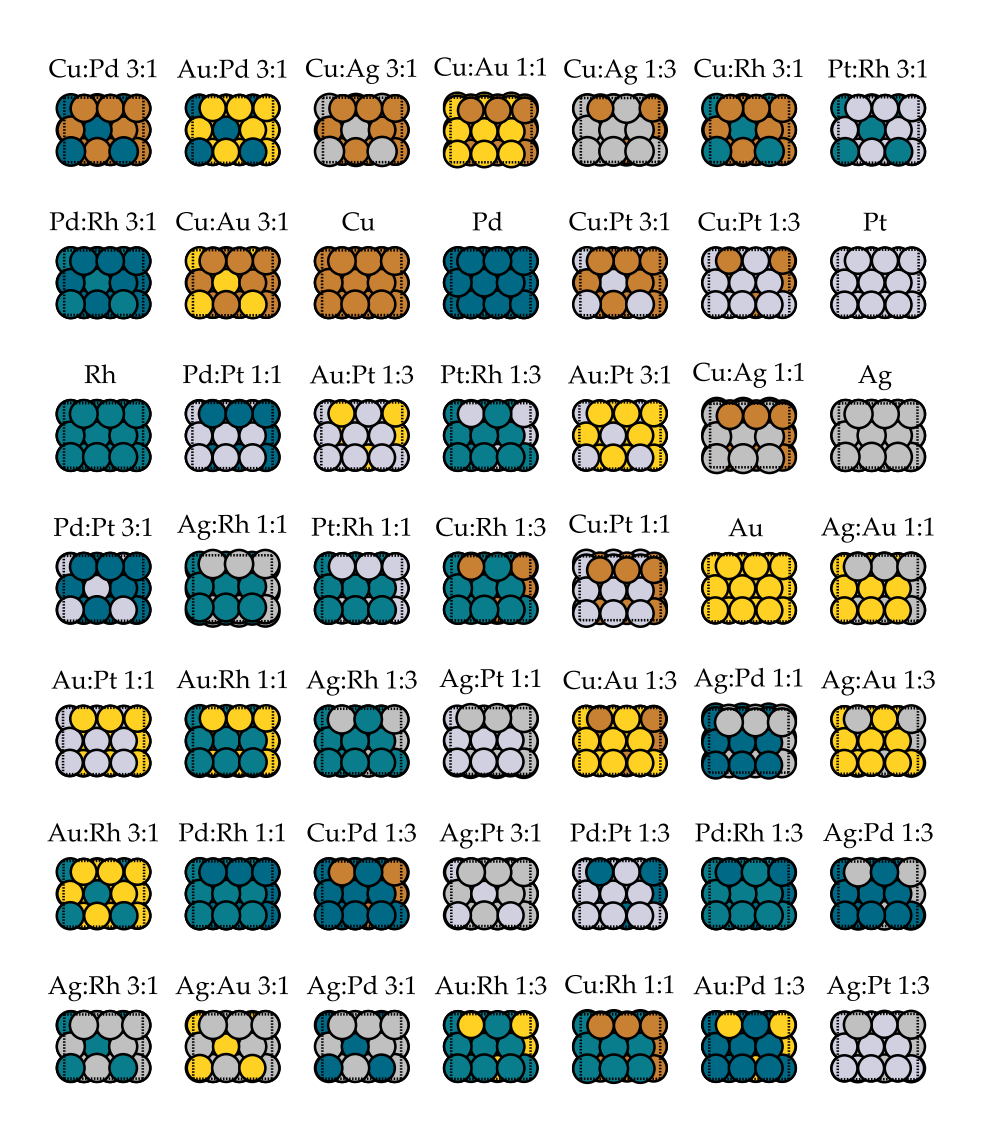


Figure 45. Sample of generated bimetallic-alloys.

Nevertheless, despite the flexible and robust infrastructure that was built for the automatic generation of alloy-slab simulations and their submission for calculation, to mitigate inconsistencies between pseudopotentials, bimetallic-alloy DFT data available on the CatalysisHub<sup>50</sup> database was retrieved and re-referenced in agreement with the current microkinetic model. This strategy was adopted to accelerate the generation of results while covering a broader range of alloy compositions, thus providing more alternatives for potential bimetallic catalyst candidates, with a total of 330 available carbon and oxygen 211-facet binding energies for combination of the over 39 different metallic elements.

Figure 46 illustrates the information flow from the traditional DFT-to-formation energies scheme, the grey arrows, and the inverse approach, the red path. The inverse problem consists of the reparameterization of reaction energies in terms of the energy of specific reference species. We have developed an algebraic approach to perform such reparameterization, and thus allow the utilization of reaction-energy data from the

literature. The approach consists of representing the interdependence between elementary reactions and their associated energies through the chemical system's stoichiometry matrix (M). This gives rise to an underlying system of linear equations whose solutions are the re-referenced formation energies. The linear system of equations can be solved in a least-squares sense or by utilizing the Moore-Penrose low-rank inversion method.

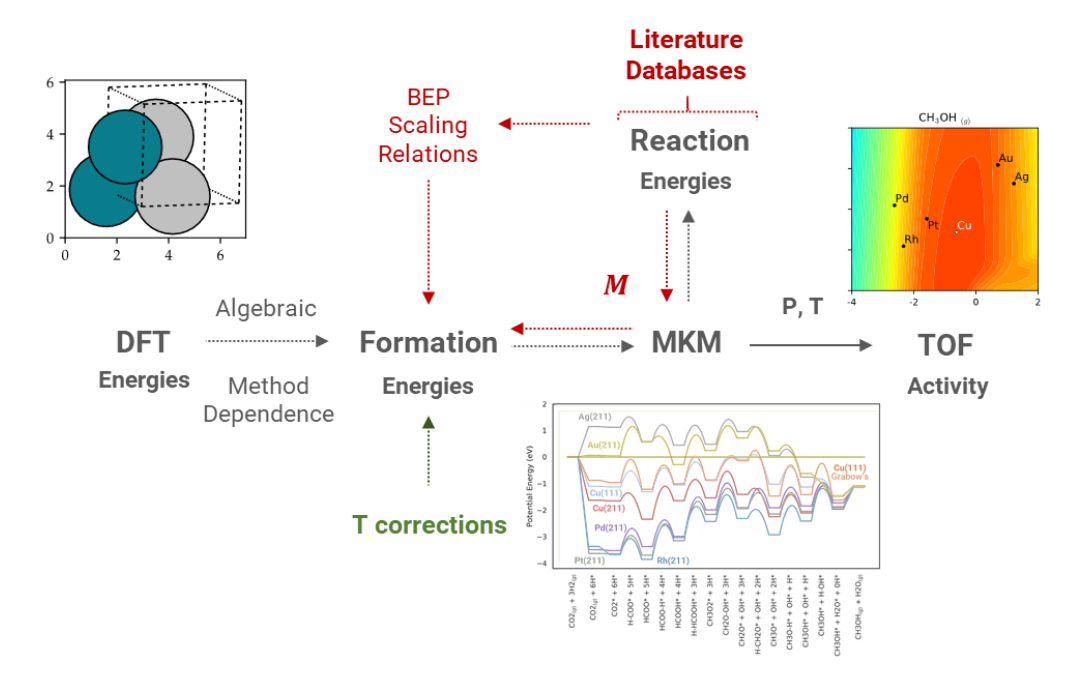


Figure 46. Proper referencing scheme for literature-gathered DFT energies.

Since all the binding energies in the database have molecular oxygen and graphene as a reference, the latter DFT energy was also computed to allow for energies to be rereferenced in alignment with those used within the microkinetic model. This strategy was successfully implemented, and the alloy screening results follow in Subtask 9.2.

# (ii) Subtask 9.2 - Identify target alloy catalysts

DFT energies for bimetallic alloys were retrieved from CatalysisHub¹ database, which encompasses hundreds of reaction energies related to bi-metallic alloys, for different facets, e.g. 111, 211. A few additional DFT calculations were necessary to allow the rereferencing of literature-retrieved reaction energies with the same references as those in the microkinetic model.

The computational screening of alloys was performed at two different conditions: (i) reactor inlet/feed, 3:1 H<sub>2</sub>:CO<sub>2</sub>, 40 bar and 593K and (ii) equilibrated RWGS at 40 bar and 593K, starting at inlet conditions. With scenario (i) alloys can be discriminated according

<sup>&</sup>lt;sup>1</sup> https://www.catalysis-hub.org/

to their activity to methanol versus RWGS, where scenario (ii) describes an operating point where CO generated from RWGS is recycled to equilibrium; thus, in the latter case, alloys are evaluated in terms of methanol synthesis against methanation.

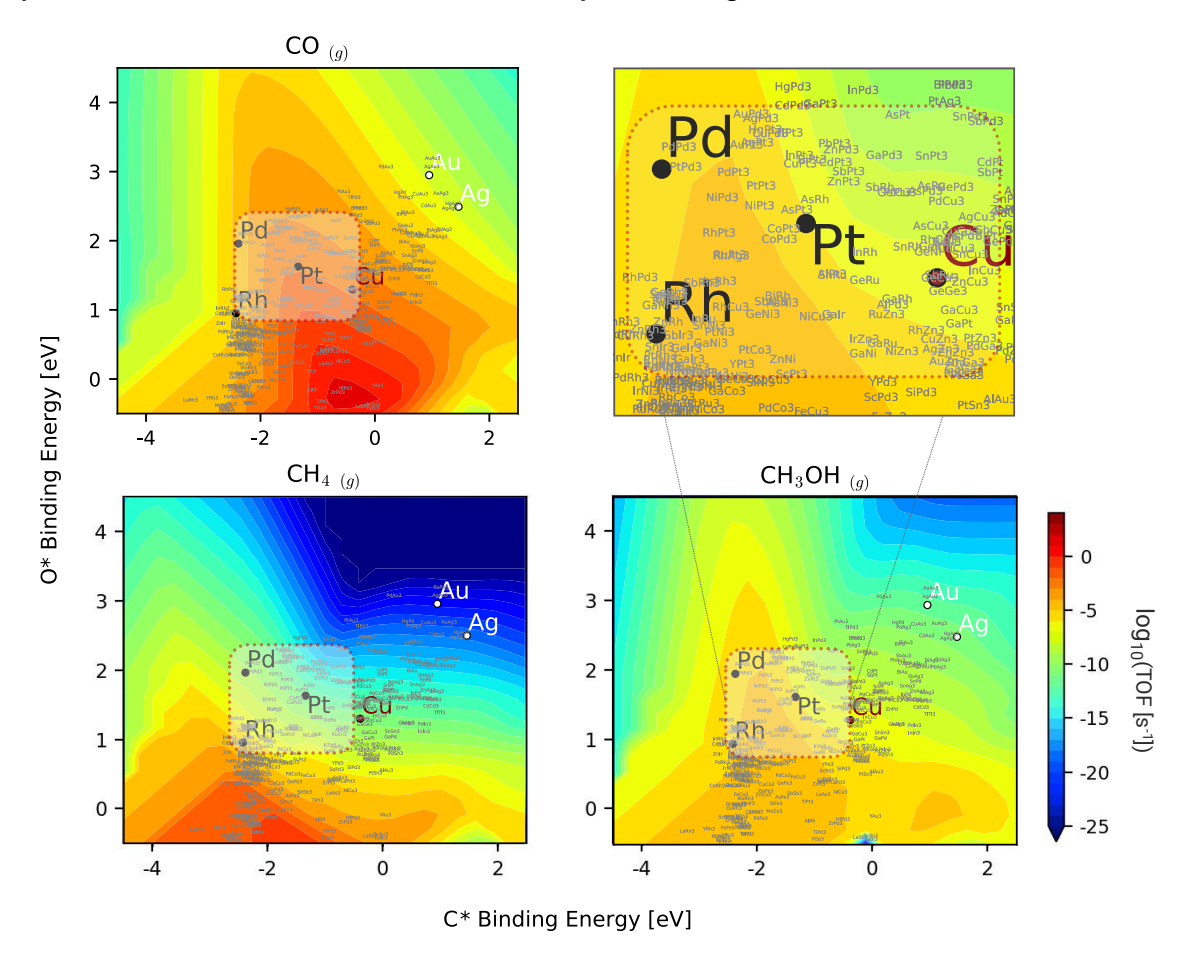


Figure 47. Bimetallic alloys screening: turnover frequencies for methane, carbon monoxide and methanol at reactor inlet conditions: 3:1 H<sub>2</sub>:CO<sub>2</sub>, 40 bar and 593 K.

From inspection of the trends in the catalytic activity map in Figure 47, the binding-energy region where there is an optimal trade-off between methanol production and byproducts carbon monoxide and methane entails the same metals as the base case scenario for the single-metal analysis, in Subtask 7.3, i.e. Rh, Pd, Pt and Cu. For lower oxygen binding energies, both methanation and RWGS prevail, whereas methanol synthesis activity decreases for either higher or lower carbon binding energies.

The RWGS-equilibrated scenario is the most interesting one from the application standpoint. The equilibrium conversion was obtained by estimating the equilibrium constant from the Gibbs free energy of reaction and solving for the extent of reaction starting at the inlet conditions. The final solution leads to approximately 3 mol% CO (and

H<sub>2</sub>O) recirculating in the stream. The Gibbs free energy of reaction for the RWGS was refined by including literature-reported standard Gibbs free energy of reaction from NIST Chemistry WebBook<sup>51</sup> for the estimation of species formation energies.

Interestingly, by equilibrating the RWGS reaction, the binding-energy region within which methanol synthesis is favored extends to higher carbon binding energy values as compared to the inlet reactor condition. The extended region includes additional Cu, Pt and Pd alloys, as shown in Figure 48. CO formation is negligible in this scenario. The main bimetallic catalysts reported in scientific literature for the synthesis of methanol from CO<sub>2</sub> lie within the boxed regions in Figures 47-48, e.g. nickel-gallium and gallium-palladium alloys, among many other more noble, e.g. PtPd, and exotic alloys, e.g. YPt<sub>3</sub>.

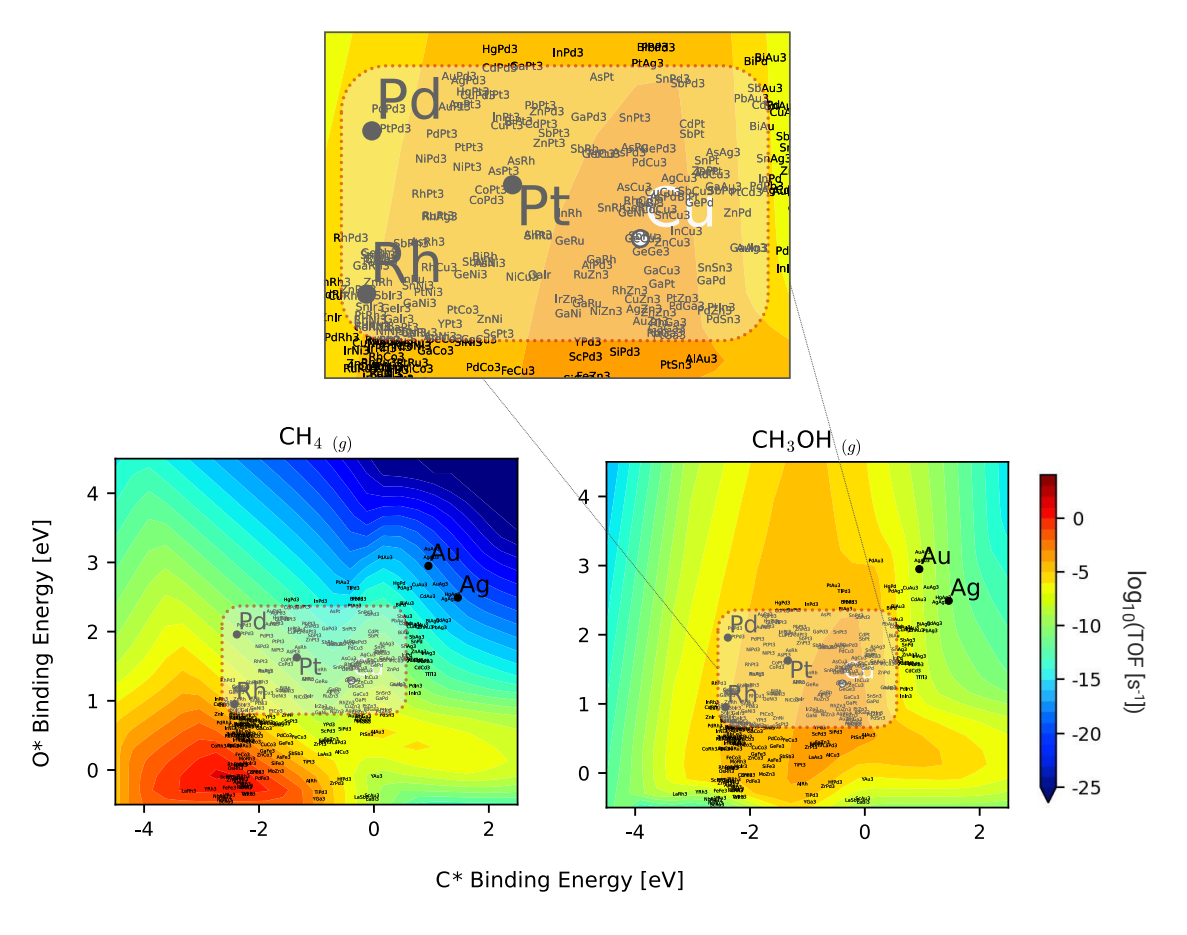


Figure 48. Bimetallic alloys screening: turnover frequencies for methane, carbon monoxide and methanol at RWGS equilibrated conditions: feed 3:1 H<sub>2</sub>:CO<sub>2</sub>,40 bar and 593K.

Anticipated metal combinations arise around the copper region, in a range between zinc, nickel, copper and gallium, as well as the noble metals gold, platinum, silver, palladium and rhodium. In Table 5, catalysts are ranked according to their selectivity and activity to methanol. The selectivity metric is given by the ratio between normalized TOF of methanol and methane, the major carbon-containing product. References for publication that have recently explored such catalysts follow in their captions.

Table 5. Bimetallic catalyst scores based on selectivity, S, and activity, TOF, to methanol for the RWGS equilibrated scenario

Catalyst	log(S)	Catalyst	log(TOF)
YPd3	25.95	SiPd3	-3.79195
SbRh	7.16	AuZn3	-3.83346
SnPd3	6.48	AgZn3	-3.83591
PdZn3	6.11	CuZn3	-3.85963
CuPd3 <sup>52</sup>	5.56	RhZn3	-3.88347
PtIn3	5.50	Zn	-3.89754
SnPt3	5.27	FeZn3	-3.90164
GaRh	5.19	RuGa3	-3.92626
GeNi	5.00	NiZn3	-3.92694
GaNi <sup>53</sup>	4.88	LaPd3	-3.93169
GePd3	4.82	Ga	-3.94496
AgCu3	4.73	ScPd3	-3.95983
PtGa3	4.67	RhGa3	-3.96673
RuGa3	4.50	PtGa3	-3.97279
LaPd3	4.39	SiCu3	-3.98152
AuZn3	4.29	YPd3	-3.98278
InRh	4.22	HfPt3	-3.98796
Ga	4.12	GaPt	-4.00731
GePd	3.96	GeCu3	-4.00934
PdGa3 <sup>54</sup>	3.92	Ge	-4.01004
AgZn3	3.88	SbRu	-4.01308
SbRu	3.83	GaCu3	-4.04398
RhZn3	3.79	GeNi	-4.06401
PtZn3	3.77	GeRh	-4.07422
RhGa3	3.76	ZrPt3	-4.08106

#### D. Conclusions

<u>Subtask 9.1 – DFT on alloys</u>: An alternative approach to accelerate the generation of results is provided in Subtask 9.2, where over 300 literature-reported bimetallic alloys DFT energy were properly reparameterized to allow their use in conjunction with the current microkinetic model.

<u>Subtask 9.2 – Identify target alloy catalysts</u>: A range of potential bimetallic alloys is suggested in Subtask 9.2, being the most relevant from the application perspective, catalysts that exhibit high catalytic activity under equilibrated RWGS conditions.

# XII. Task 10.0 – Experimental testing of new alloy compositions

# A. Goals and Objectives of the Task

In this task, we look at identifying promising metal alloys. Synthesis and experimental testing of promising alloys identified computationally in Task 9.0 will be completed.

<u>Subtask 10.1 – Establish synthesis procedures:</u> In this subtask, we intend to synthesize and perform routine characterization of computationally predicted alloy nanoparticles. These catalysts will be physically mixed with ZSM5 crystals of size determined from Task 6.0 to have the optimal diffusion-reaction length scales.

<u>Subtask 10.2 – Experimental evaluation of alloys:</u> The synthesized metal alloy catalysts physically mixed with ZSM-5 crystals will be studied for steady-state conversion testing, measuring rates and selectivities.

# B. Objectives and Research Methods

Based on literature reports and preliminary computational results, a NiGa/SiO<sub>2</sub> catalyst was synthesized via incipient wetness impregnation. An aqueous solution of nickel nitrate (Ni(NO<sub>3</sub>)<sub>2</sub>·6H<sub>2</sub>O (98%, Alfa Aesar)) and gallium nitrate (Ga(NO<sub>3</sub>)<sub>3</sub>·xH<sub>2</sub>O (99.9%, Sigma-Aldrich)) with a molar ratio of 5:3 was added dropwise to silica gel (70-230 mesh, 60 Å, Aldrich) to obtain a final metal load of 20 wt%. The catalyst was dried in air at 75 °C overnight, calcined in air at 400 °C for 4 h with a heating ramp of 5 °C/min and reduced at 700°C under 10%  $H_2/N_2$  for 2 h. On the successful synthesis of the metal alloy catalyst by this method, other metal alloy catalysts in this study would be synthesized by following similar procedure as well.

These synthesized catalysts would be tested for successful synthesis by means of XRD and H<sub>2</sub>-TPR. Following that each of the metal alloy catalyst would then be individually tested for CO<sub>2</sub> hydrogenation to methanol performance across a range of temperatures and pressures to find the best performing metal alloy catalyst for physically mixing with H-ZSM-5 for high performance of CO<sub>2</sub> hydrogenation to aromatics.

#### C. Results and Discussions

Subtask 10.1 – Establish synthesis procedures: The formation of a NiGa alloy instead of separate phases of Ni and Ga was determined by temperature programmed reduction in H2 (TPR) and X-ray diffraction analysis (XRD). Figure 49(a) presents the TPR profile of NiGa compared with a Ni/SiO<sub>2</sub> catalyst with the same metal loading. For the Ni/SiO<sub>2</sub> catalyst, only two peaks were observed at 303.7 °C and 414.6 °C, which are related to reduction of NiO species. On the contrary, for the NiGa catalyst, multiple peaks were observed at 283.5, 381.9 490.3 and 632.0 °C. Sharafutdinov et al.<sup>55</sup> assigned peaks beyond 400 °C to the formation of NiGa alloys with different stoichiometry, Ni<sub>3</sub>Ga and Ni<sub>5</sub>Ga<sub>3</sub>, respectively. Figure 49(b) presents XRD pattern of the reduced catalyst, where characteristic peaks of Ni<sub>5</sub>Ga<sub>3</sub> phase at 43°, 48°, 75° 87°, and 95° were observed.<sup>55</sup> Thus, incipient wetness impregnation was a successful synthesis procedure for the formation of the NiGa alloys and can be considered for the synthesis of additional alloys proposed from the computational experiments.

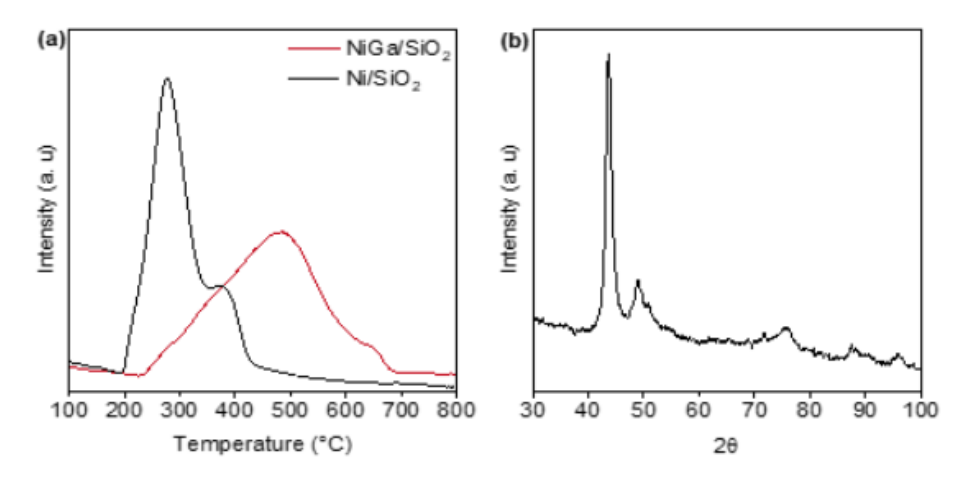


Figure 49: (a) TPR profile of NiGa/SiO<sub>2</sub> catalyst, and (b) XRD pattern of the reduced NiGa/SiO<sub>2</sub> catalyst

PdZn/SiO<sub>2</sub> and PdGa/SiO<sub>2</sub> have also been synthesized. The synthesis method followed was similar to that used for NiGa/SiO<sub>2</sub>. The synthesis process involves incipient wetness impregnation of the metal ions on SiO<sub>2</sub> followed by calcination. The X-ray diffraction results of these synthesized bimetallic alloy catalysts can be found in Figure 50. The crystalline structure, in comparison with the existing ICDD data, supports the formation of the bimetallic alloy.

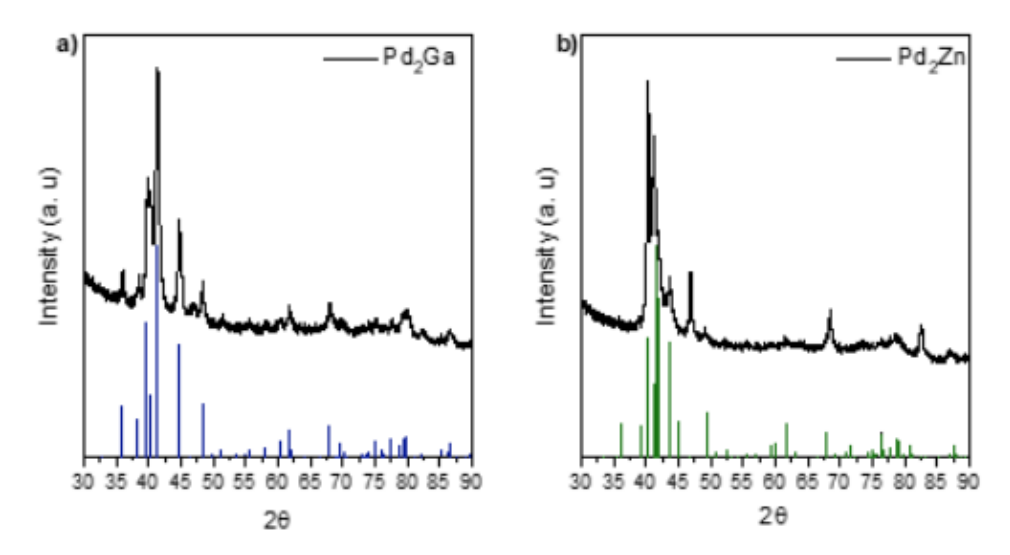


Figure 50: X-ray diffraction of a) PdGa/SiO<sub>2</sub> and b) PdZn/SiO<sub>2</sub>. The peaks are compared with the ICDD database

<u>Subtask 10.2 – Experimental evaluation of alloys:</u> An evaluation of the synthesized alloy catalysts in the temperature range between 240 – 340 °C and WHSV between 3600 - 32400 mL/g<sub>cat</sub>/h was completed. Figure 51 presents CO<sub>2</sub> conversion and product selectivity of NiGa/SiO<sub>2</sub>, PdGa/SiO<sub>2</sub> and PdZn/SiO<sub>2</sub> catalysts. For all catalysts, the main products obtained were CO, MeOH, DME and CH<sub>4</sub>. High WHSV has a positive effect on MeOH selectivity, but a negative effect on CO<sub>2</sub> conversion. At 320 °C, the required

temperature for aromatics synthesis, PdGa/SiO<sub>2</sub> exhibit the highest MeOH selectivity (~15 %) and CO<sub>2</sub> conversion (~8%) at 7200 mL/g<sub>cat</sub>/h.

Additionally, similar behavior was observed upon temperature increase for all the alloy catalysts. At low temperatures, MeOH selectivities above 90% were obtained, but conversion decreases to ~1, 6, and 5% for NiGa/SiO<sub>2</sub>, PdGa/SiO<sub>2</sub> and PdZn/SiO<sub>2</sub> catalysts, respectively. High CO<sub>2</sub> conversion over the Pd catalysts can be related to high activity of Pd for H<sub>2</sub> dissociation. However, at high temperatures, the endothermic RWGS reaction becomes more relevant, following Le Châtelier's principle, and CO selectivity increases above 80%. PdGa/SiO<sub>2</sub> alloy catalyst exhibit the best CO<sub>2</sub> conversion and MeOH selectivity at the relevant conditions for CO<sub>2</sub> to aromatics reaction. For that reason, this catalyst was selected for further testing of the tandem catalyst for aromatics synthesis. Further analysis for testing CO<sub>2</sub> hydrogenation to aromatics when the PdGa/SiO<sub>2</sub> (best catalyst per our results) used in tandem with H-ZSM-5 will be covered in Task 12.0.

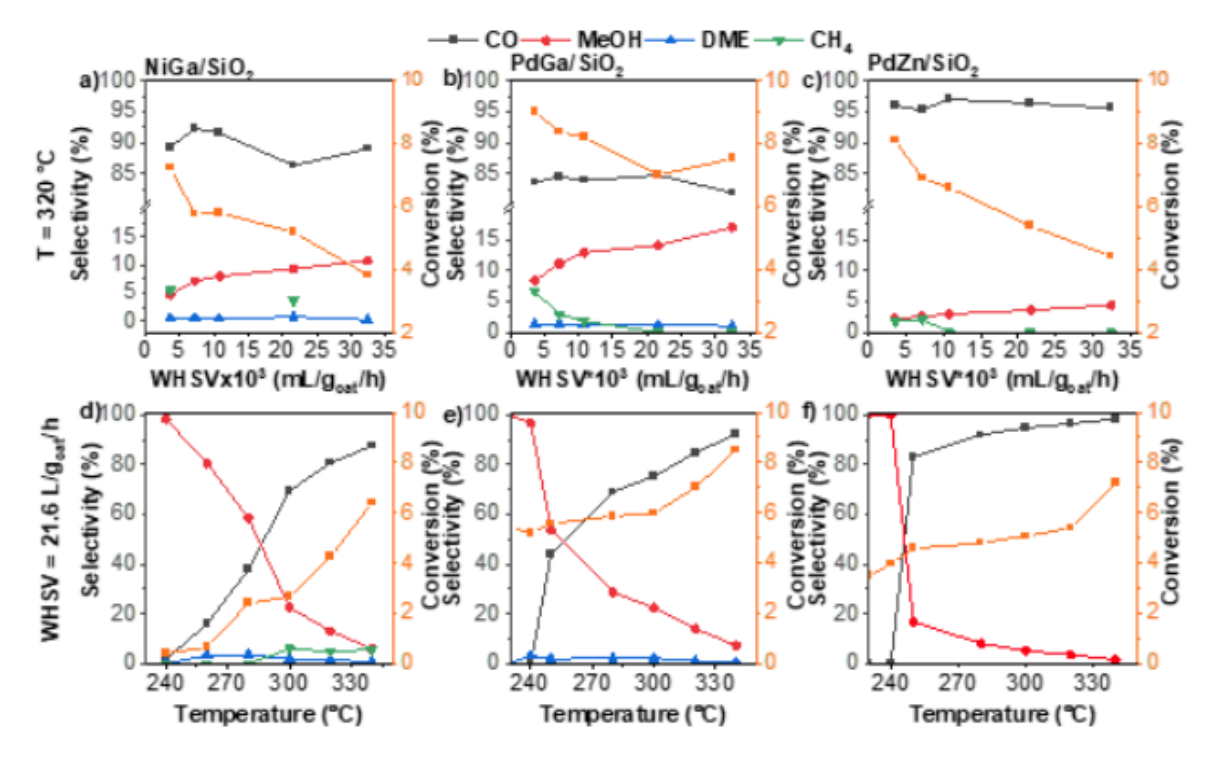


Figure 51: Catalytic activity of a,d) NiGa/SiO<sub>2</sub>; b,e) PdGa/SiO<sub>2</sub>; c,f) PdZn/SiO<sub>2</sub> at different WHSV (a-c) and temperatures (d-f)

#### D. Conclusions

Catalysts NiGa/SiO<sub>2</sub>, PdGa/SiO<sub>2</sub> and PdZn/SiO<sub>2</sub> were tested with varying temperatures and WHSV. The selectivity for MeOH decreases significantly with increasing temperatures where reverse water-gas shift reaction dominates leading to high production of CO. While all the 3 catalysts still show very low selectivity for MeOH compared to ZnZrO, PdGa/SiO<sub>2</sub> shows the best performance of the 3 catalysts.

## XIII. Task 11.0 – Refine mechanism based on presence of aromatics

## A. Goals and Objectives of the Task

Aromatic species will be incorporated into the model based on a coupled kinetic model for ZSM5 conversion of methanol/alkanes to/from aromatics to assess the influence of conversion on back-reactions and selectivity.

<u>Subtask 11.1 – Macroscale model development:</u> Develop macro-scale kinetic model of conversion of methanol/alkanes to aromatics based on experimental results.

<u>Subtask 11.2 – Model combination/integration:</u> Integrate the macro-scale kinetic model with the micro-kinetic model in CatMAP.

<u>Subtask 11.3 – Extended CatMAP to varied conversion prediction:</u> Use the CatMAP model to evaluate activity/selectivity as a function of conversion to aromatics.

# B. Background and Research Methods

The initial CO<sub>2</sub> to methanol macroscale model development started with the reparameterization of the standard Cu/ZnO/Al<sub>2</sub>O<sub>3</sub> Langmuir-Hinshelwood-Hougen-Watson (LHHW) lumped-kinetics based on experimental data for ZnZrO<sub>x</sub> initially devised by Buschen et. al.,<sup>56</sup> then readjusted by Mignard and Pitchard<sup>57</sup> using the equilibrium constants by Graaf et. al.<sup>58</sup>.

The estimation of kinetic parameters for the tandem ZnZrO<sub>x</sub>:ZSM-5 catalyst relied on the CO<sub>2</sub> to methanol LHHW model in combination with similar LHHW structures for methanol to hydrocarbons (MTH). Moreover, given the complex pool of species that are found experimentally for the MTH reaction, i.e., short and long chain olefins and paraffins, ranges of methylated aromatics, species were lumped according to mechanism postulates. The initial attempts of kinetic parameter fitting were based on an algebraic model for the dual-cycle mechanism on H-ZSM-5, as proposed by Janssen et al.<sup>60</sup>, which is shown in Figure 52 below.

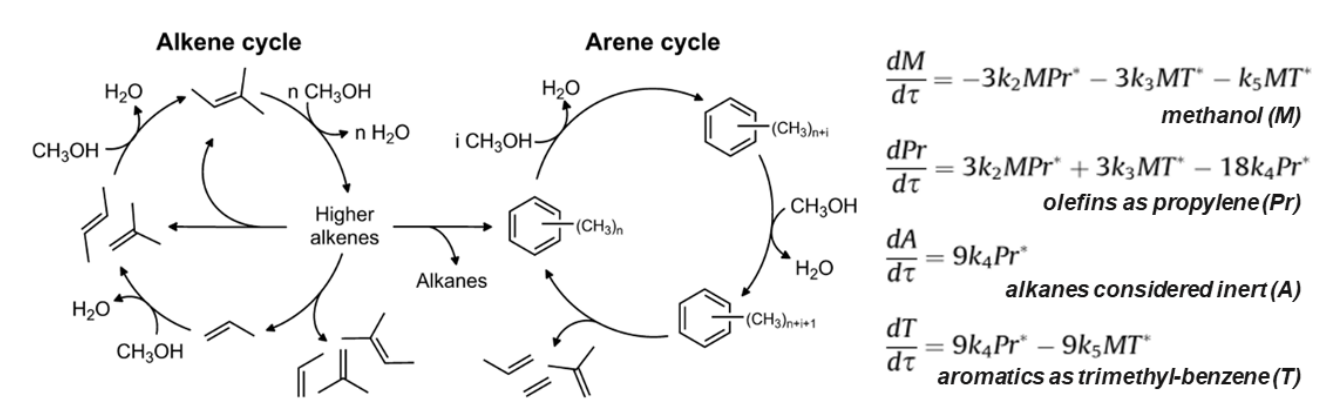


Figure 52. Dual cycle mechanism (left) and simplified algebraic model (right) by Janssens et al. 61

#### A. Results and Discussions

## (i) Subtask 11.1 – Macroscale model development

#### (a) CO2 to Methanol

The lumped-kinetic model consists of the rate-equations for the RWGS and methanol synthesis, with five Arrhenius/Van't-Hoff-like temperature-dependent parameters and another five pre-exponential factors, as depicted in equations 15-18.

$$r_{CH_3OH} = \frac{k_1 P_{CO} P_{H_2} \left( 1 - \frac{1}{K_{eq_1}} \frac{P_{H_2O} P_{CH_3OH}}{P_{H_2}^3 P_{CO_2}} \right)}{\left( 1 + k_2 \frac{P_{H_2O}}{P_{H_2}} + k_3 P_{H_2}^{0.5} + k_4 P_{H_2O} \right)^3} \left[ \frac{mol}{kg_{cat} s} \right]$$
(15)

$$r_{RWGS} = \frac{k_5 P_{CO_2} \left( 1 - K_{eq_2} \frac{P_{H_2O} P_{CO}}{P_{CO_2} P_{H_2}} \right)}{\left( 1 + k_2 \frac{P_{H_2O}}{P_{H_2}} + k_3 P_{H_2}^{0.5} + k_4 P_{H_2O} \right)} \left[ \frac{mol}{k g_{cat} s} \right]$$
(16)

$$k_i = A_i \exp\left(\frac{B_i}{RT}\right) \tag{17}$$

$$\log_{10} K_{eq_1} = \frac{3066}{T} - 10.592$$

$$\log_{10} K_{eq_2} = \frac{2073}{T} - 2.029$$
(18)

The literature-reported Cu/ZnO/Al<sub>2</sub>O<sub>3</sub> refined kinetic parameters and those found based on experimental data for ZnZrO<sub>x</sub> are conveyed in Table 6 as reported by Van-Dal et. al.<sup>59</sup>.

Table 6. Kinetic parameters CO<sub>2</sub> to methanol for Cu/ZnO/Al<sub>2</sub>O<sub>3</sub> [B given in kJ/mol] and adjusted parameters for ZnZrO<sub>x</sub> (this work).

Parameter		Cu/ZnO/Al <sub>2</sub> O <sub>3</sub>	$ZnZrO_x$
$k_1$	$A_1$	1.07	
	$B_1$	40.0	56.10
$k_2$	$A_2$	3453.38	
	$B_2$	_	-17.65
$k_3$	$A_3$	0.499	
	$B_3$	17.197	4.399
$\overline{k_4}$	$A_4$	$6.62 \times 10^{-11}$	
	$B_4$	124.119	135.9
$k_5$	$A_5$	$1.22 \times 10^{10}$	
	$B_5$	-98.084	-75.25

The underlying inverse problem, i.e., to estimate the kinetic model parameters based on known model structure, was solved by integrating a simplified fixed-bed reactor model over the catalyst mass used experimentally. Since low conversion ranges are covered under experimental conditions, the simplified model is assumed isothermal, and any pressure drop is neglected; additionally, mass-transfer resistances in our ZnZrO<sub>x</sub> experimental data are insignificant across the WHSV and temperature range studied. For the sake of simplification, the gas phase is modelled as an ideal gas. Importantly, a strong assumption is that the CO<sub>2</sub> to methanol mechanism for ZnZrO<sub>x</sub> would be similar to that of Cu/ZnO/Al<sub>2</sub>O<sub>3</sub>. Under such conditions, the kinetic model can be represented by a set of coupled ordinary differential equations (ODE):

$$\frac{d}{dw}\,\dot{\boldsymbol{n}}_1 = -f_1(\boldsymbol{n}_1, \boldsymbol{p}_1) \tag{19}$$

where  $n_1$  is the molar flowrate of involved chemical species, w is the catalyst bed mass and  $f_1$  represents the kinetic model with parameters  $p_1$ . The parameter estimation problem is solved by enforcing experimental results as boundary conditions for the integration of equation 19, as conveyed by equation 20.

$$\min_{\boldsymbol{p}} \left\| \int_0^{w_{cat}} dw \left( f_1(\boldsymbol{n_1}, \boldsymbol{p_1}) - \frac{d}{dw} \, \dot{\boldsymbol{n}}_1 \right) \right\|_2^2 \tag{20}$$

In which the inlet and outlet experimental molar flowrates,  $\dot{\boldsymbol{n}}_1^0 = \dot{\boldsymbol{n}}_1(0)$  and  $\dot{\boldsymbol{n}}_1^0 = \dot{\boldsymbol{n}}_1(w_{cat})$ , respectively, are enforced.

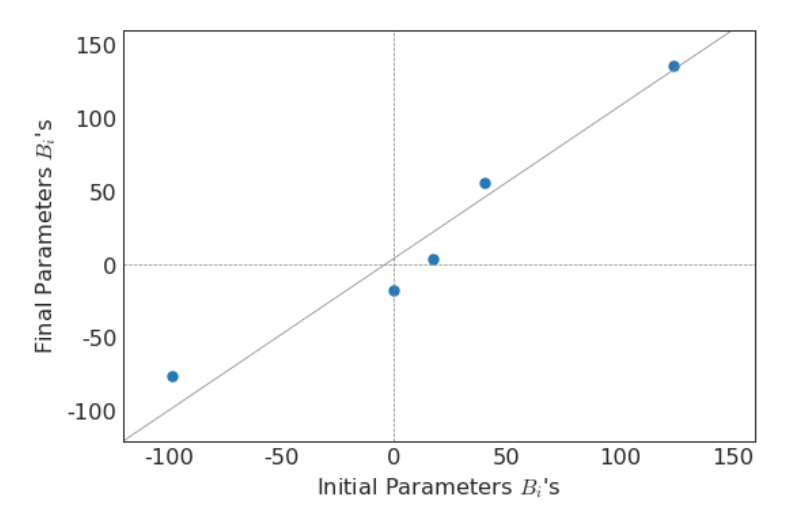


Figure 53. Temperature-related parameter ( $B_i$ ) estimation, initial vs. final estimated parameter from the inverse problem solution.

In Figure 53, the temperature-related final parameters from the inverse problem solution for ZnZrO<sub>x</sub> still preserve high correlation with the original refined parameters for the

Cu/ZnO/Al<sub>2</sub>O<sub>3</sub> catalyst. The boundary conditions for the inverse problem encompass sets of experimental data over a range of WHSVs and temperature, as shown in Figure 54.

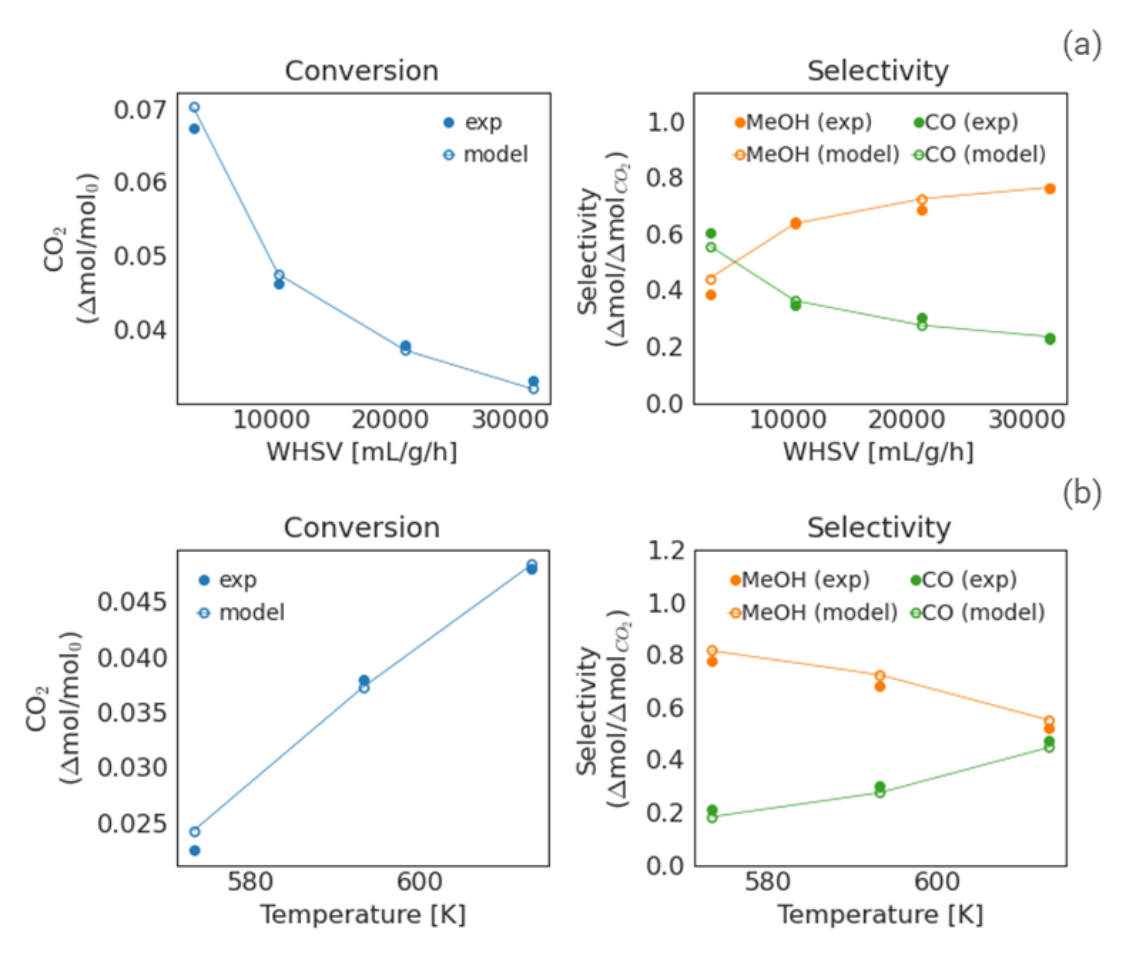


Figure 54. Experimental and predicted (ODE integration) outlet conditions: (a) fixed temperature (320°C) and varying WHSV, (b) fixed WHSV (21.2 L/g/h) and varying temperature.

Despite the low residuals between results predicted by integration of the CO<sub>2</sub>-to-methanol lumped-kinetics ODE model with the estimated model parameters and the experimental measurements, it is necessary to emphasize that the experimental conditions only span a narrow conversion range, and any extrapolation to higher CO<sub>2</sub> conversion values would implicate lower confidence.

### (b) CO2 (to Methanol) to Hydrocarbons

### Mechanistic Analysis and Experimental Results

Our experimental results for the tandem ZnZrO<sub>x</sub>:ZSM-5 catalyst over the range of weight-hourly space velocities (WHSV) between 600 to 10800 mL/g/h, and temperatures from 300 to 360°C, **Table 7** suggest that the pathway for the production of alkanes is detached from that of the aromatization of higher alkenes.

**Table 7**. Experimental results for CO<sub>2</sub> to hydrocarbons reaction over the tandem ZnZrO<sub>x</sub>:ZSM-5 catalyst (this work) as a function of WHSV and temperature.

Temp.	WHSV	Conv.	CO	Par.	Ole.	Arom.	C7+
_°C	L/g/h	%	C %	C %	C %	C %	C %
320	0.60	20.3	48.6	40.22	3.08	9.03	2.19
320	1.20	14.3	48.6	39.65	5.15	12.8	0.91
320	3.60	12.1	44.6	38.95	8.40	12.8	1.47
320	7.20	11.0	38.0	36.01	10.9	14.6	1.67
320	10.8	9.49	40.3	36.77	12.0	13.6	1.97
300	7.20	7.25	35.3	36.51	10.5	13.8	4.85
340	7.20	11.7	45.1	45.09	7.53	11.1	1.24
360	7.20	14.6	53.5	41.46	5.86	6.17	0.54

As a result, attempts to fit the dual-cycle simplified mechanism were unsuccessful. The carbon-selectivity correlation matrix involving the tandem catalyst reaction products for the CO<sub>2</sub> to hydrocarbons over different temperature and WHSV ranges is shown in Figure 55. Though the correlation matrix does not provide the full picture of the underlying reaction mechanism, it allows for the inference of the main reaction pathways. As expected, the CO production is anticorrelated with all products of the MTH reaction except for paraffins, with which it mildly correlated. Such a pattern supports the hypothesis that, for the tandem catalyst, the RWGS is independent of the MTH-associated pathways, and the more carbon is converted to CO through RWGS, the lower will be the production of methanol and, therefore, of MTH-related species.

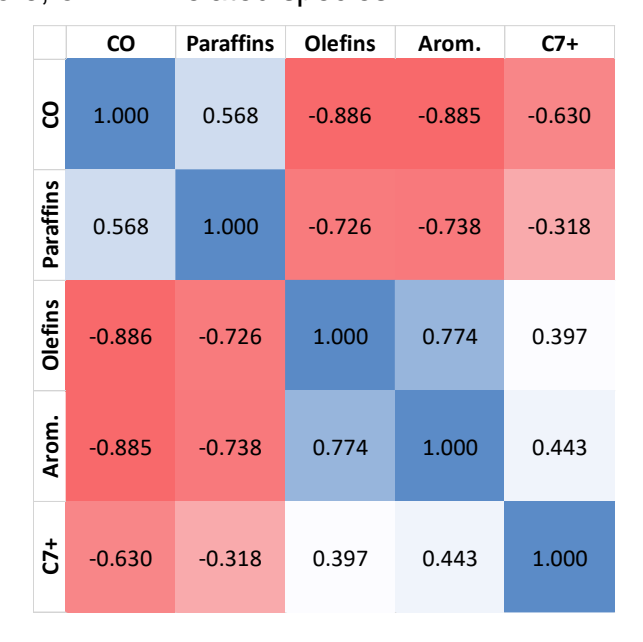


Figure 55. Carbon-selectivity reaction product correlation matrix for the CO2 to hydrocarbons reaction on the tandem ZnZrOx:ZSM-5 catalyst. Lumped hydrocarbons species have: 2.5, 5, 9 and 7 carbons, for paraffins, olefins, aromatics and C7+ alkanes, respectively.

As for the MTH-associated pathways, olefins, aromatics and C7+ species seem to follow a separate pathway than that of paraffins production. However, since unsaturated hydrocarbons are initially formed from methanol dehydration/methylation reactions, the

natural assumption is that olefins must still be an intermediate in the paraffins route, which corroborates the fact the latter is uncorrelated with all olefin-derived species, i.e., aromatics and, possibly, C7+.

#### General LHHW Framework

A proposed reduced set of chemical pathways connecting measurable gas-phase species and satisfying the overall material balances is shown in Table 8. This set of reactions was utilized to define the reaction network within which the inverse problem, equation 20, would have to be solved to retrieve kinetic parameter estimates for the LHHW-type rate-equations, as performed for the CO<sub>2</sub> to methanol and RWGS pathways. Various attempts to build LHHW-type rate equations for the MTH set of reaction led to unsatisfactory results, either not reproducing the selectivity or the conversion obtained experimentally. To supplant the need for heuristically devising LHHW rate equation hypotheses, we attempted to extend Ji and Deng's<sup>62</sup> approach for autonomous discovery of unknown reaction pathways from simple power-law kinetics to also include convoluted LHHW reaction types.

**Table 8**. Proposed MTH material balance. Where the methanol (MeOH) source is CO/CO<sub>2</sub> conversion from the fitted CO<sub>2</sub> hydrogenation and RWGS LHHW model. Subindices refer to the number of carbons considered for each lumped species.

Reaction	Stoichiometry
1	$2.5 MeOH \rightarrow 10 le_{C2.5} + 2.5 H_2O$
2	$2.5 MeOH \xrightarrow{Aro} 10 le_{C2.5} + 2.5 H_2O$
3	$2 \ Ole_{C2.5} \rightarrow 1Par_{C5} + 1H_2$
4	$3.6 \ Ole_{C2.5} \rightarrow 1Aro_{C9} + 3H_2$
5	$2.8 \ Ole_{C2.5} \rightarrow 1Par_{C7} + 1H_2$

The mathematical structure for the combined (coupled) tandem model follows in equation 21, where  $n_1$  refers to species in the CO<sub>2</sub> to methanol and RWGS pathways, i.e., CO<sub>2</sub>, H<sub>2</sub>, CO, H<sub>2</sub>O and methanol, whose reaction stoichiometries are conveyed by the columns of the stoichiometry matrix  $M_1$ . The LHHW rate equations for the first set of reactions are conveyed by the function  $\phi_1 = \left[r_{CH_3OH}, r_{RWGS}\right]^T$ , which has the known structure from LHHW models reported in literature, equations 15-18.

$$\frac{d}{dw}\dot{\boldsymbol{n}} = \frac{d}{dw} \begin{bmatrix} \dot{\boldsymbol{n}}_1 \\ \dot{\boldsymbol{n}}_2 \end{bmatrix} = -f(\boldsymbol{n}, T, \boldsymbol{p}_1, \boldsymbol{p}_2) = [\boldsymbol{M}_1 \quad \boldsymbol{M}_2] \times \begin{bmatrix} \phi_1(\boldsymbol{n}, T, \boldsymbol{p}_1) \\ \phi_2(\boldsymbol{n}, T, \boldsymbol{p}_2) \end{bmatrix}$$
(21)

The MTH set of reactions is represented by the stoichiometry matrix  $M_2$ , which connects the involved species in  $n_2$  with methanol and rate equations to which they are associated,  $\phi_2$ . As previously mentioned, the crucial issue regarding the MTH set of reactions is to find appropriate structures for the LHHW rate equations conveyed by  $\phi_2$ . Conversely, the positive aspect of the formulation in equation (21) is that the algebraic mapping (projection) of the nonlinear functions  $\phi$ 's onto M enforces that the material balance be satisfied irrespective of the structure of  $\phi$  under the assumption that kinetic ODEs are

also satisfied. The extension of Ji and Deng's<sup>62</sup> approach for a general LHHW framework was devised by generating structures for  $\phi_2$  of the following form:

$$\phi_{2}(\boldsymbol{x},T,\boldsymbol{p}_{2}) = \frac{\left(1 - \boldsymbol{W}_{3}^{1} exp\left(\ln\left(\boldsymbol{W}_{2}^{1} exp\left(\boldsymbol{W}_{1}^{1} \ln \boldsymbol{x} - \frac{\boldsymbol{b}_{1}^{1}}{T}\right)\right) - \frac{\boldsymbol{b}_{2}^{1}}{T}\right)\right) exp\left(-\frac{\boldsymbol{b}_{3}^{1}}{T}\right)}{\left(1 + \mathbf{1}^{T} \boldsymbol{W}_{3}^{2} exp\left(\ln\left(\boldsymbol{W}_{2}^{2} exp\left(\boldsymbol{W}_{1}^{2} \ln \boldsymbol{x} - \frac{\boldsymbol{b}_{1}^{2}}{T}\right)\right) - \frac{\boldsymbol{b}_{2}^{2}}{T}\right)\right)^{\boldsymbol{b}_{3}^{2}}}$$
(22)

where  $x = n/\sum n$  is the concentration of species vector and  $p_2$  encompasses all of the  $\phi_2$  parameters, i.e.,  $p_2 = \{W,b\}_i^j$  for  $i \in [1;3]$  and  $j \in [1,2]$ . Such a mathematical formulation allows for the representation of linear combination of power-law kinetics, i.e.,  $exp\left(W_1^1 \ln x - \frac{b_1^1}{T}\right)$ , in the numerator, where the  $W_1^1$  matrix is constrained to only map concentrations of species  $i, x_i$ , involved in a particular reaction, whereas the denominator is shared among all rate equations, and may encompass any power-law-type kinetics between any species in the chemical reaction. The inverse problem for the MTH set of reactions consists of solving for the parameters  $p_2$  given fixed stoichiometry matrices and pre-fitted  $p_1$  the inverse problem in (23). Proper boundary conditions are necessary, which are determined from the experimental results. In addition, since the parameter space for the general LHHW framework can be large, we introduce a LASSO penalization term (L1-norm) with hyperparameter  $\lambda$ , which is known to provide shrinkage behavior, reducing the final size of the model by forcing the shrinkage of correlated parameters.

$$\min_{\boldsymbol{p}_2} \left\| - \int_0^{w_{cat}} dw \left( f(\boldsymbol{n}, T, \boldsymbol{p}_1, \boldsymbol{p}_2) - \frac{d}{dw} \, \dot{\boldsymbol{n}} \right) \right\|_2^2 + \lambda |\boldsymbol{p}_2|_1$$
 (23)

### General LLHW Model Results and Directions

The inverse problem solution entails an optimization problem in terms of the kinetic model parameters,  $p_2$ , while satisfying the chemical kinetics ODE. We formulated the optimization problem simultaneously for the eight different experimental conditions and their associated results. While  $\phi_2$  was built according to equation 22, the ODE solution n(w) was solved with fully-connected feed-forward physics-informed neural network (PINN)<sup>63</sup> as basis functions, with their own non-physical parameter, which acts as a general neural-network based surrogate approximation for differential equations.

Despite the general aspect of our LHHW framework, the dynamics of the first set of reactions,  $\phi_1$ , involving methanol synthesis and RWGS, embeds high stiffness to the ODE solution. In such a scenario, we were only able to obtain partial convergence of the inverse problem, which could be justified for the inability of the PINN to represent stiff or vanishing gradient behavior, or that the LHHW assumption may not hold. Representative results for the partial method convergence are shown in Figure 56 with the results for the eight different experimental conditions in terms of WHSV and temperature, for which the

PINNs solution diverts from the actual numerical one under the same underlying kinetic model at flat response regions.

Given the potential utility and general aspect of the neural-network based LHHW framework, we will continue to explore other strategies for the autonomous retrieval of LHHW-type kinetic model based on data. However, if this endeavor proves unsuccessful for the experimental data associated with the complex MTH set of reactions, further macroscale-dependent analyses may be carried out about the actual experimental conditions, without a true mechanistic model, but still reflecting the performance metrics, e.g., conversion and selectivity, of the developed tandem catalyst.

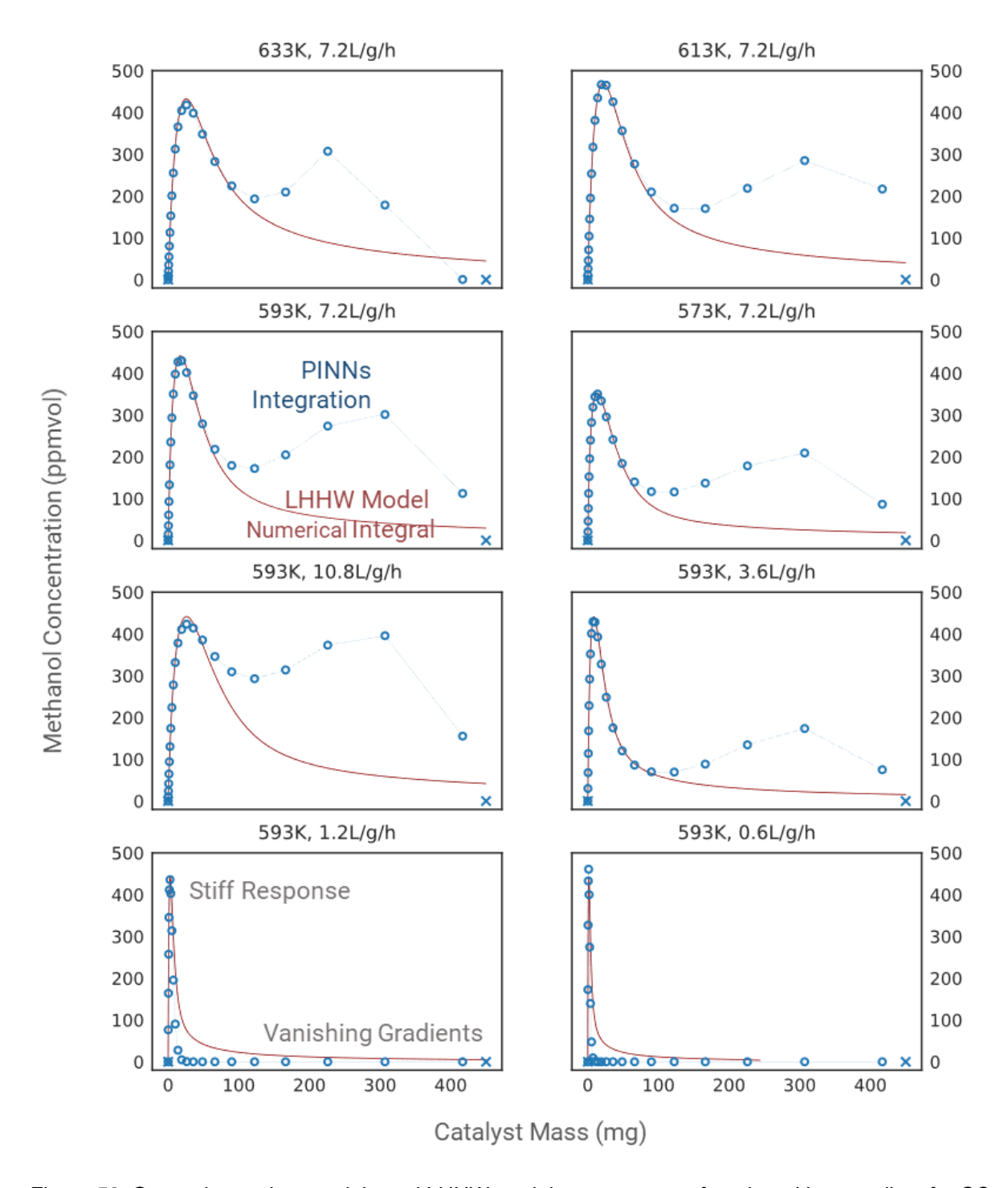


Figure 56. General neural-network based LHHW partial convergence of methanol intermediate for CO<sub>2</sub> to aromatics conversion on the tandem catalyst ZnZrO<sub>x</sub>:ZSM-5; PINNs based- (open circles) and numerical integration (solid line) of the incumbent LHHW model structure.

### Model Simplification and the Introduction of an Algebraic Framework

Given the difficulties associated with solving the inverse problem, especially due to numerical instability and the complexity of the LLHW structure, we studied simplified versions of  $\phi_2$ , as power-law kinetics, and lumped the methanol synthesis reaction with the olefin intermediate formation. In this case, a mechanistic model for the former reaction is not assumed and its concentration profile and associated stiffness need not be estimated. For the sake of simplification, the set of reactions is assumed reversible and are shown in Table 9.

Table 9. Simplified MTH material balance, where the methanol intermediate is suppressed and lumped into the CO<sub>2</sub> to olefins reaction. Subindices refer to the number of carbons considered for each lumped species.

Reaction	Stoichiometry
1	$2.5 CO_2 + 7.5 H_2 \rightarrow 10 le_{C2.5} + 5 H_2 O$
2	$2 \ Ole_{C2.5} \rightarrow 1Par_{C5} + 1H_2$
3	$3.6 \ Ole_{C2.5} \rightarrow 1 Aro_{C9} + 3 H_2$
4	$2.8 \ Ole_{C2.5} \rightarrow 1Par_{C7} + 1H_2$

The power-law kinetics with Arrhenius temperature dependence leads to reducing equation 22 into 24. In the latter, b conveys the Arrhenius-like temperature dependence, c the entropic factor and w introduces the power dependence of each species in a specific reaction. The advantage of working with equation 24 is that the law-of-mass action reversibility factor need not be explicitly enforced, and it is instead conveyed by explicitly including forward and reverse pathways in w.

$$\Phi_2(\mathbf{x}, T, \mathbf{p}_2) = exp\left(\mathbf{W}_1^1 \ln \mathbf{x} - \frac{\mathbf{b}_1^1}{T} + \mathbf{c}_1^1\right)$$
 (24)

To assist the solution of the underlying boundary value problem through PINNs, we proposed a novel formulation to the original design equation described in equation 25that relies on the concept of extent of reaction,  $\xi$ , and the representation of the material balance in terms of the singular value decomposition, SVD, of the stoichiometry matrix. Additionally, the representation of molar flowrates in terms of a neural network is changed to a vector of molar fraction and the total molar flowrate scalar. Equation 25 represents the integral form of equation 21 and outlines the connection between  $\xi$  and the rate equations,  $\phi$ .

$$\dot{n}\mathbf{x} - \dot{n}_0 \mathbf{x_0} = -\int_{w} f(\mathbf{n}, T, \mathbf{p}_1, \mathbf{p}_2) \, dw = \mathbf{M} \times \int_{w} \boldsymbol{\phi} \, dw = \mathbf{M} \times \boldsymbol{\xi}$$
 (25)

Where  $\dot{n}_0$  is the molar flowrate and  $x_0$  is the molar fraction vector at the reactor inlet. Such an integral form allows for the representation of any molar fraction x along a reactor catalyst bed in terms of the extent of reaction by noticing that  $n = n_0 + \mathbf{1}^T M \xi$ , which leads to the relationship in equation 26.

$$\mathbf{x} = \frac{\dot{n}_0 x_0 + M \xi}{\dot{n}_0 + \mathbf{1}^T M \xi} \tag{26}$$

An outcome of equation 26 is that any pair of solutions  $\xi$  and x that satisfies the equality, and such that  $x(0) = x_0$  and  $x(1) = x_f$  over a normalized w domain, is a solution that satisfies the material balance imposed by the reaction stoichiometries.

To further simplify the representation of x, we explore a common feature of M, which is that it is often rank-deficient. SVD comes in handy to provide bases for the range and nullspace of  $M \in \mathbb{R}^{n \times m}$ , as represented by equation 27.

$$M = [\mathbf{U}^{\mathbf{R}} \ \mathbf{U}^{\mathbf{N}}] \operatorname{diag}([\mathbf{s}, \mathbf{0}]) [\mathbf{V}^{\mathbf{R}} \ \mathbf{V}^{\mathbf{N}}]^{\mathbf{T}}$$
(27)

Where  $U^R$  is an orthonormal basis for the range of M. Therefore, any  $\mathbf{x} = M\mathbf{\phi}$ ,  $\mathbf{x} \in \mathbb{R}^n$  and  $\mathbf{\phi} \in \mathbb{R}^m$  can be represented as  $\mathbf{x} = \mathbf{U}^R\mathbf{z}$ , where  $z \in \mathbb{R}^k$ ,  $\mathbf{z} = \mathbf{S}\mathbf{V}^{R^T}\mathbf{x}$ ;  $k = dim(\mathbf{s})$  is the rank of M, and s > 0 are the singular values of M. Additionally, SVD also allows for components of rate equations  $\mathbf{\phi}$  that do not contribute to net rates-of-change – i.e., those associate to equilibrated reactions – to be penalized, given that they are represented by the projection  $\mathbf{\phi}$  onto the nullspace of M, as shown by the nullspace residuals conveyed by equation 28.

$$\|\mathbf{V}^{\mathbf{N}^T}\mathbf{\phi}\|_{2}$$
, (equilibrated reactions) (28)

Hence, equation 26 can be represented in reduced dimension by noticing that  $M\xi = U^R z$ , where  $\xi \in \mathbb{R}^m$  and  $z \in \mathbb{R}^k$ ,  $k \le m$ . The final representation of x feasibility is shown in thre residual term in equation 29.

$$\|\mathbf{x}(\dot{n}_0 + \mathbf{1}^T \mathbf{U}^R \mathbf{z}) - \dot{n}_0 \mathbf{x}_0 - \mathbf{U}^R \mathbf{z}\|_2$$
, (feasible solution) (29)

Following, equation 25 can be differentiated to provide a relationship between  $\xi$ , now represented in terms of z and the rate equations  $\varphi$ , as in equation 30.

$$\frac{d}{dw}\left(\mathbf{M} \times \int_{w} \boldsymbol{\phi} \, dw\right) = \mathbf{M} \times \frac{d}{dw} \int_{w} \boldsymbol{\phi} \, dw = \mathbf{M} \times \boldsymbol{\phi} = \mathbf{M} \boldsymbol{\xi}' = \mathbf{U}^{\mathbf{R}} \mathbf{z}' \tag{30}$$

SVD and the orthogonality principle provide the reduced relationship between z and  $\varphi$  in the row space of M, as shown in terms of the feasibility condition in equation 31.

$$\|\mathbf{S}V^{R^T}\mathbf{\Phi} - \mathbf{z}'\|_{2}$$
, (feasible model) (31)

The reformulated inverse problem consists of a combination of equations 28, 29 and 31, which can either be solved simultaneously by minimizing a weighted sum of the associated residuals (problem 32, for some  $\alpha > 0$ ) or in a two-step fashion, where (i) feasible solutions x are obtained by minimizing the cost function defined by 29 only

followed by the minimization of 31 combined with 28 to find physically-consistent rate equations  $\phi$ . The latter problem consists of using  $\alpha = [1,0,0]$  for the first step and  $\alpha = [0,1,1]$  for the second one.

$$\operatorname{Min}_{\mathbf{p}} \int_{0}^{w_{cat}} dw \ \alpha_{1} \left\| \mathbf{x}(w) \left( \dot{n}_{0} + \mathbf{1}^{T} \mathbf{U}^{\mathbf{R}} \mathbf{z}(w) \right) - \dot{n}_{0} \mathbf{x}_{0} - \mathbf{U}^{\mathbf{R}} \mathbf{z}(w) \right\|_{2}^{2} \\
+ \alpha_{2} \left\| \mathbf{S} \mathbf{V}^{\mathbf{R}^{T}} \mathbf{\phi}_{\mathbf{p}} (\mathbf{x}(w)) - \mathbf{z}'(w) \right\|_{2}^{2} + \alpha_{3} \left\| \mathbf{V}^{\mathbf{N}^{T}} \mathbf{\phi} (\mathbf{x}(w)) \right\|_{2}^{2}$$
(32)

Implicit in all solutions is that both  $\mathbf{x}$  and  $\mathbf{z}^{\mathbf{R}}$  are artificial neural networks with their own parameter tensors, which are constructed such that the boundary value conditions are structurally satisfied, i.e.,  $\mathbf{x}(0) = \mathbf{x}_0$ ,  $\mathbf{x}(1) = \mathbf{x}_f$ , and  $\mathbf{z}^{\mathbf{R}}(0) = \mathbf{0}$ ,  $\mathbf{z}^{\mathbf{R}}(1) = n_f \mathbf{U}^{\mathbf{R}^T} \mathbf{x}_f - n_0 \mathbf{U}^{\mathbf{R}^T} \mathbf{x}_0$ .

### Simplified Power-Law Model Results and Directions

In the same fashion as for the general LHHW model, here the PINN structure depends on artificial neural networks  $\mathbf{z}^R(w)$  and  $\mathbf{x}(w)$ , where the former provides potential state candidates along the reactor bed and the latter acts like a filter to provide feasible solutions. The filter attribute of x arises for its architecture embeds a DAE constraint, such that  $0 \le \mathbf{x}(w) \le 1$ ,  $\mathbf{1}^T \mathbf{x}(w) = 1$ ,  $\forall w$ , as proposed by Gusmão et. al.<sup>64</sup>. Hence, only feasible solutions are parsed to  $\phi$ , preventing numerical inconsistent (negative values) results and errors during the neural network training procedure.

For the simplified power-law model, the MTH reaction set was considered reversible, and the temperature-dependent parameters for the RWGS reaction in Table 6 were allowed to vary. As previously mentioned, the  $CO_2$  to methanol reaction is lumped within the olefins pathway. That, especially because no methanol was reported in the tandem catalyst experimental data and any estimate of its concentration profile would be not unique. The total catalyst mass in the reactor bed is of 450mg, where 1/3 is  $ZnZrO_x$  and 2/3 H-ZSM-5. For the sake of simplicity, we assume a homogeneous media, and the kinetic parameters here found are reported in terms of the whole catalyst mixture instead of possibly independent or distinguishable reaction domains. To avoid numerical issues, the integration interval, i.e., the total catalyst bed mass is normalized prior to PINNs training. Therefore, rate constants were further rescaled accordingly. The model-predicted (after integration) versus experimental results for the tandem catalysts for the groups of lumped hydrocarbons are shown in Figure 57. The estimated kinetic parameters can be found in Table 10. All experiments were carried out at 40bar.

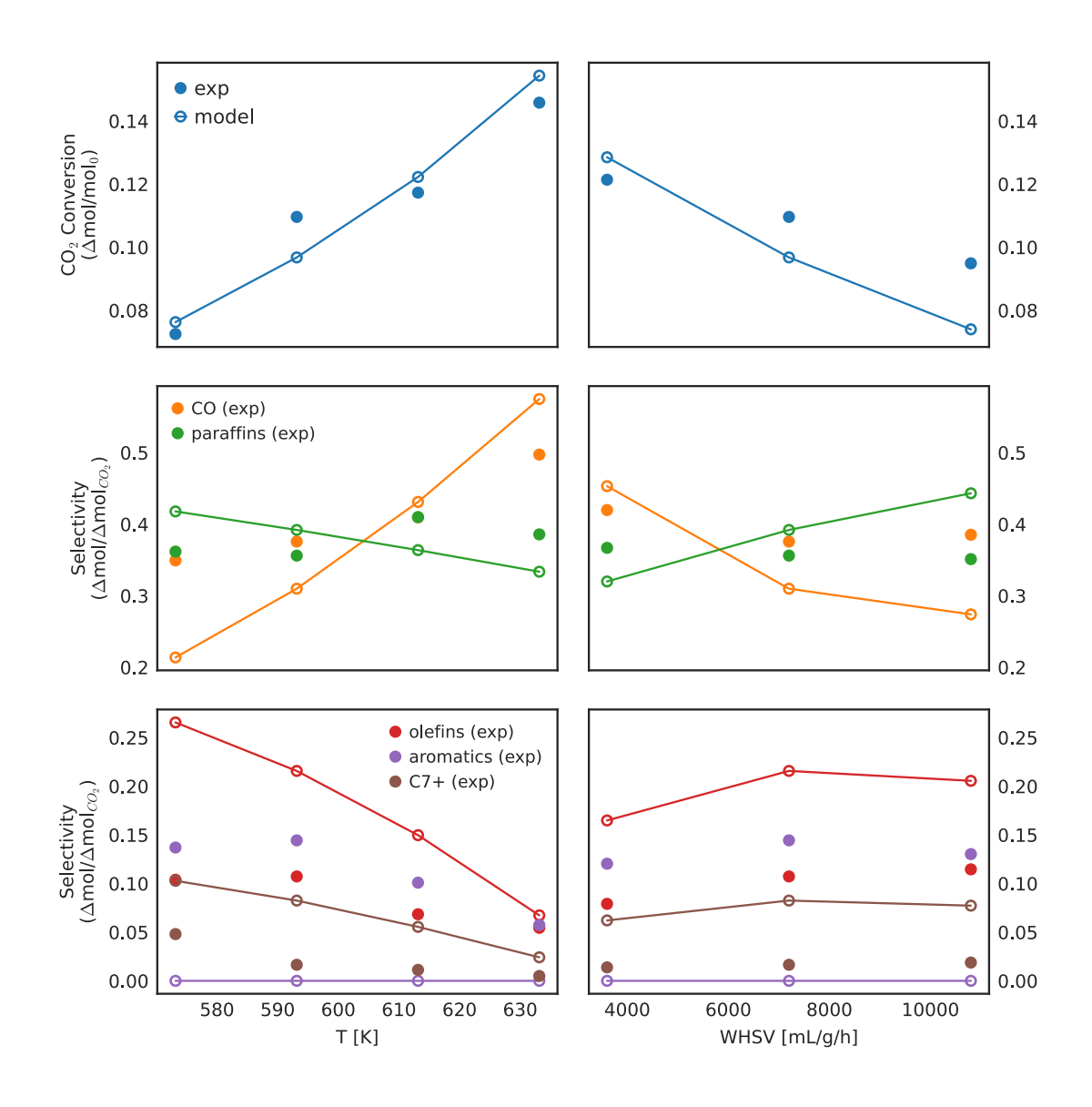


Figure 57. Combined-model experimental and predicted (ODE integration) outlet conditions: (right) fixed temperature (320°C) and varying WHSV, (left) fixed WHSV (7.2 L/g/h) and varying temperature.

Table 10. Simplified MTH material balance and RWGS power-law kinetic model results.

Reaction	$k_0$	$\boldsymbol{E_A}$	Power	Term						
Units	$mol\ s^{-1}kg$	kJ /mol	CO <sub>2</sub>	$H_2$	CO	$H_2O$	Par <sub>C5</sub>	Ole	Arom	Par <sub>C7</sub>
1 (fwd)	560	32	2.7	-	-	-	-	-	-	-
2	1	34	-	-	-	-	-	-	-	-
3	1	55	-	-	-	-	-	4	-	-
4	$1.24 \times 10^{8}$	-	-	4	-	-	-	2.8	-	-
1 (rev)	170	10	-	-	-	2.4	-	-	-	-
2	70.2	-	-	-	-	-	1.6	-	-	-
3	4.39×10 <sup>1</sup>	-	-	-	-	-	-	-	4	-
4	$3.16 \times 10^7$	-	-	-	-	-	-	-	-	2.2
RWGS (f)	4.88×10 <sup>4</sup>	88	1	-	-	-	-	-	-	-
RWGS I	5.20×10 <sup>7</sup>	128	-	-1	1	1	-	-	-	-

Concentrations are considered in terms of molar fractions.

We hypothesize that the utilization of a full reversible model given the reduced set of available experimental points might have caused the concentration power-dependences to reach the imposed bounds (i.e., between 0 and 4). An even more simplified model is under construction considering only the forward reaction.

#### Neural-network approach assessment based on SSITKA transient data

To assess the developed neural-network approach, we applied it to an external steady-state isotopic transient kinetic analysis (SSITKA) data. SSITKA consists of a conjunction of operando analytical-chemistry techniques that provide temporal information about catalyst, i.e., adsorbates, and gas phase composition as a heterogeneous reaction proceeds. Gas phase composition is typically analyzed through mass spectroscopy (MS) whereas surface intermediates (adsorbates) are identified and quantified with diffusive-reflectance infrared Fourier-transform spectroscopy (DRIFTS). To assess the ability of our physics-inspired neural network-based method to produce verisimilar LHHW models, we utilized a MS dataset provided by the Jones group on a chemical system involving CO<sub>2</sub> methanation and the reverse water-gas-shift reaction.

Only MS data were utilized in the assessment to resemble the experimental data obtained for the tandem ZnZrO<sub>x</sub>:ZSM-5 catalyst; however, instead of methanol synthesis in a plugflow reactor, in this case, we analyze the methanation reaction in a SSITKA cell. The MS data consist of the convoluted fragmentation pattern of the different molecules in the reactor outlet stream. In this preliminary study, we only analyze the first part of the isotopic experiments, where only carbon-12 isotopes are fed to the reactor, as shown in Figure 58.

Total pressure dependence is lumped in the pre-factors (40 bar)

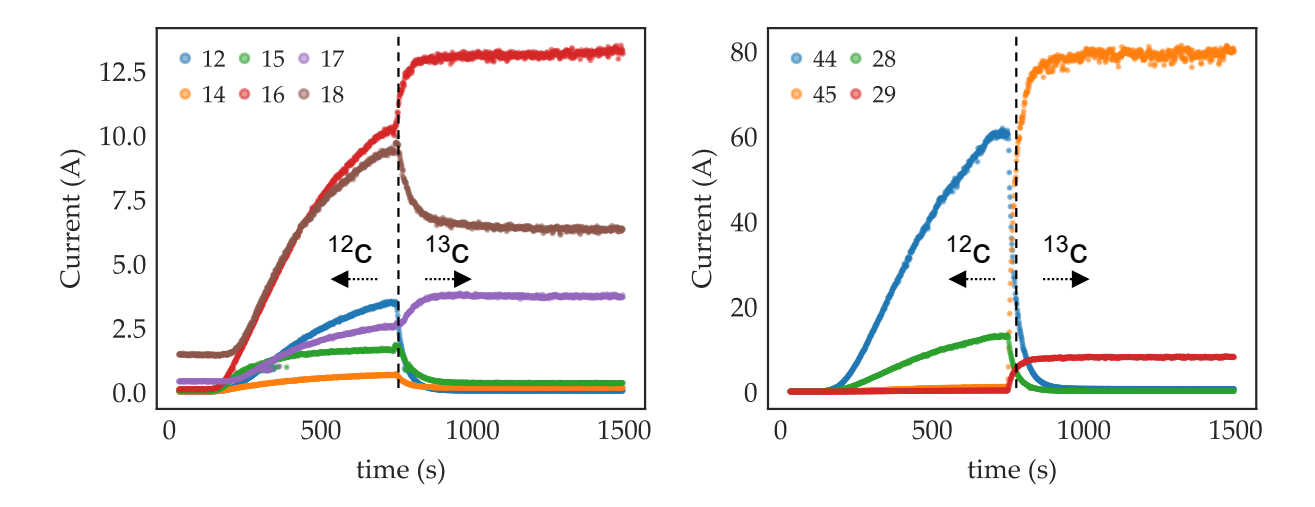


Figure 58. Convoluted methanation and reverse water-gas-shift. Convoluted methanation and RWGS SSITKA ionization mass-spectroscopy signals: water, methane, and CO2/CO fragments (left) nonfragmented CO2 and CO (right). Convoluted methanation and reverse water-gas-shift SSITKA mass-spectroscopy normalized signals.

To model the SSITKA cell, we approximate it as an adiabatic transient continuous-flow stirred tank reactor (CFSTR) under pseudo-homogeneous assumption, i.e., gas and solid phases with uniform properties, such that the chemical system may be represented by LHHW lumped models. Using a similar notation to equation 33, the CFSTR design equation takes the form of equation 33, where  $\bf x$  is a vector with molar fraction of involved chemical species inside the reactor,  $\bf x_{in}$  is the reactor feed compositions,  $\bf \tau$  is the residence time in the SSITKA cell,  $\bf M$  is the stoichiometry matrix encompassing both the methanation and RWGS, and  $\bf \phi$  is a function that maps concentrations into a LHHW rate equation with parameters  $\bf p$ , as in equation 33.

$$\frac{d}{dt}\mathbf{x} - \frac{\mathbf{x}_{in} - \mathbf{x}}{\tau} = -f(\mathbf{x}, T, \mathbf{p}) = \mathbf{M} \times \phi(\mathbf{x}, T, \mathbf{p})$$
(33)

Differently from the differential packed-bed reactor where only boundary values (concentrations at the inlet and outlet) are known and the model integration takes place over space, the main advantage of working with CFSTR transient data is that the integration is over time, and the outlet composition that is measured through MS is assumed to be the same of that of the reactor. The optimization problem to be solved is

shown in equation 34, which is similar to that of equation 21, except for the inclusion of measured data, i.e., MS signals  $\tilde{s}_i = \tilde{s}(t_i)$ , and the explicit representation of the PINN  $x_i = x(\omega, t_i)$ , where  $\omega$  are the parameter of the PINN x.

$$\min_{\mathbf{p}, \tau, \boldsymbol{\omega}, C} \sum_{i} \left\| \mathbf{M} \times \phi(\mathbf{x}_i, T, \mathbf{p}) - \left( \frac{d}{dt} \mathbf{x}_i - \frac{\mathbf{x}_{in} - \mathbf{x}_i}{\tau} \right) \right\|_2^2 + \|\mathbf{x}_i \mathbf{C} - \tilde{\mathbf{s}}_i\|_2^2 + \lambda |\mathbf{p}|_1$$
 (34)

From left to right, the first norm in the summation is related to satisfying the LHHW physical model, whereas the second term conveys the mismatch between measured and interpolated data (MS signal). Moreover, the fragmentation pattern may also be inferred during the training process by estimating the sparse matrix  $\mathcal{C}$  that maps molar fraction x into MS signals s. The sparsity is enforced a priori by only allowing non-zero terms in  $\mathbf{c}_{ij}$  for possible fragments j of related species i. Since all SSITKA data have been gathered at a fixed temperature and pressure, such parameter dependences are not explored in this study, and are assumed to be lumped in the LLHW-NODE parameters p. Accordingly, molar fraction constraints can be directly applied to x such that  $0 \le x \le 1$  and  $1^T x = 1$ , and that the normalization is always preserved by construction by applying a trigonometric operator as developed proposed by Gusmão et. al. 64

In the approach assessment, we adopted a PINN architecture consisting of a single 100-neuron hidden layer projected onto the normalization operator. Sparsity is enforced to the fragmentation pattern in  $\mathbf{C}$  by applying a mask matrix that only allows non-zero elements for possible species fragments. Only a single active site with over 20 power-law terms was initially defined for the LHHW-NODE model to provide extensive parameterization, which could be further shrunk in a LASSO scheme, i.e., L-1 regularization in the last term in equation 34. All the minimization parameters were learned simultaneously under the ADAM training algorithm,  $^{65}$  which combines stochastic gradient descent and momentum. The residence,  $\tau$ , time was fixed at 1 and the experiment timespan was normalized.

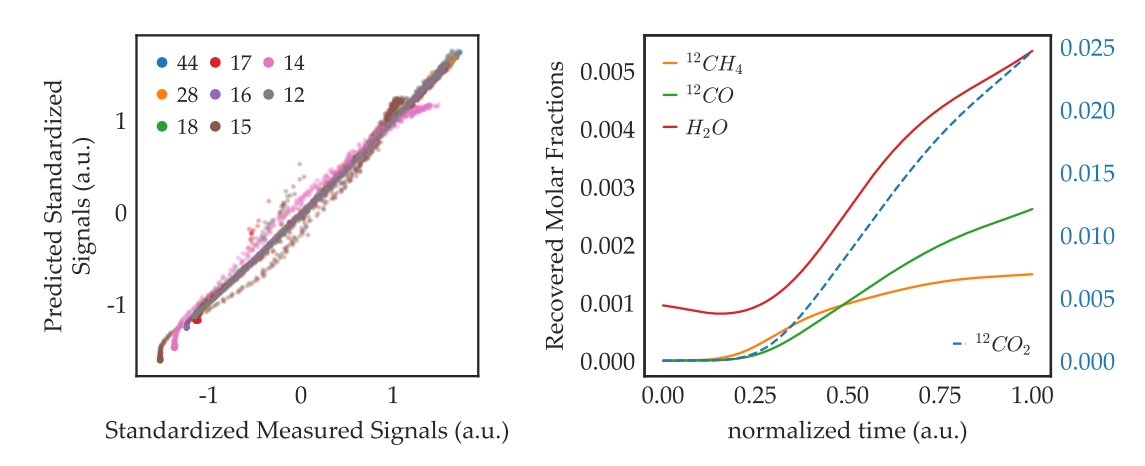


Figure 59. Parity plot for standardized MS signals (left) and reconstructed latent signals (PINNs output, right)

Preliminary results are shown in Figure 59, where the parity plot for standardized MS signals on the left represents the MS signal reconstruction under the fragmentation pattern  $\mathcal{C}$  and physical model constraints. The recovered molar fractions on the right are concentrations that are consistent with the fragmentation pattern and satisfy the incumbent NODE-LHHW model. Such results outline the PINN-NODE flexibility to interpolate dense temporal data, reconstruct latent variables (e.g., recovered molar fractions) and provide physically inspired differential equations (LHHW) that may be further validated via model-shrinkage and cross-validation scheme. There are other

sources of uncertainties in the provided dataset that were not thoroughly explored in this preliminary assessment scheme; however, the mere fact that the methods are able to reconstruct the data supports the hypothesis that it can also be utilized for the tandem-catalyst CO<sub>2</sub>-to-BTX experimental data.

## (ii) Subtask 11.2 – Model combination/integration with CatMAP

The CatMAP model expresses the first step of the CO<sub>2</sub> to BTX reaction, i.e., a wide range of possible chemical pathways involved in the conversion of CO<sub>2</sub> to methanol. In the original proposal, we assumed that the subsequent conversion of methanol to BTX would follow the same mechanism as methanol to olefins/BTX over ZSM5. However, the most recent results indicate that the bifunctional catalyst follows a different methanol conversion mechanism, and efforts have been devoted to elucidating an appropriate mechanistic kinetic model as described above. Identification of such a model is a prerequisite for integration with the existing CatMAP model, so we recommend discontinuing this task and focusing remaining efforts on identifying an appropriate macro-scale model.

The integrated macroscale model will depart from the detailed mechanistic structure that could be built for bimetallic alloys and rely on the lumped LHHW models commonly adopted for zeolitic catalysts, which is the case of H-ZSM-5. Therefore, results from Subtask 11.2 were sought in Subtask 11.1.

## (iii) Subtask 11.3 – Extended CatMAP to varied conversion prediction

This task has been merged into Subtask 11.1.

#### **B.** Conclusions

<u>Subtask 11.1 – Macroscale model development</u>: A literature-based LHHW-type lumped-kinetic model for methanol synthesis from CO<sub>2</sub> was calibrated based on experimental data for ZnZrOx. The methanol to BTX route on ZSM-5 complex mechanism involving cracking, oligomerization and alkylation has been modeled as lumped pathways to group of clustered species in terms of power-law kinetics based on the tandem catalyst experimental data.

<u>Subtask 11.2 – Model combination/Integration with CatMAP</u>: Instead of detailed-kinetic models, lumped LLHW models based on the tandem ZnZrOx:ZSM-5 experimental data was investigated in Subtask 11.1.

<u>Subtask 11.3 – Extended CatMAP to varied conversion prediction</u>: This task was discontinued and its objectives were moved to Subtask 11.1

# II. Task 12.0 – Experimental optimization of conditions for best alloy

# A. Goals and Objectives of the Task

In this task, we intend to test the best metal alloy catalyst on mixing it with H-ZSM-5 for steady state conversion under CO<sub>2</sub> hydrogenation, measuring rates and selectivities.

### B. Background and Research Methods

Best alloy catalyst (PdGa/SiO<sub>2</sub>) as inferred from Task 10 was evaluated for CO<sub>2</sub> to aromatics reaction and compared against ZnO-ZrO<sub>2</sub> catalysts. For all experiments in this task, a ratio of 1:2 of the MeOH catalysts: ZSM-5 zeolite was employed and H-ZSM-5 with Si/Al ratio of 80 and 300 was tested.

### C. Results and Discussions

Figure 60 presents the product distribution obtained with the different tandem catalysts. For all catalysts, CO<sub>2</sub> conversion was about 5% at the tested conditions. The ZnO-ZrO<sub>2</sub> tandem exhibit an aromatics selectivity of about 40%, with better performance for the low Si/Al ratio zeolite. Contrary, when using the PdGa/SiO<sub>2</sub> with H-ZSM-5, the main product was CO (> 90% selectivity), followed by C<sub>2</sub>-C<sub>3</sub> olefins. Interestingly, when using the alloy catalyst MeOH was detected in the outlet stream, with about 5% selectivity, indicating no total conversion of MeOH over the ZSM5 zeolite. It has been reported that the methanol aromatics reaction requires an induction period for the formation of the hydrocarbon pool, followed by autocatalytic reactions for olefins, paraffins and aromatics formations.<sup>10</sup> Due to low selectivity of the PdGa catalyst at 320 °C, it is possible that the hydrocarbon pool is not formed, which results in no aromatics production and low olefins and paraffins selectivity. Another possible explanation is the saturation of acid sites by high concentration of CO which could lead to low availability of acid sites to synthesize aromatics.<sup>11</sup>

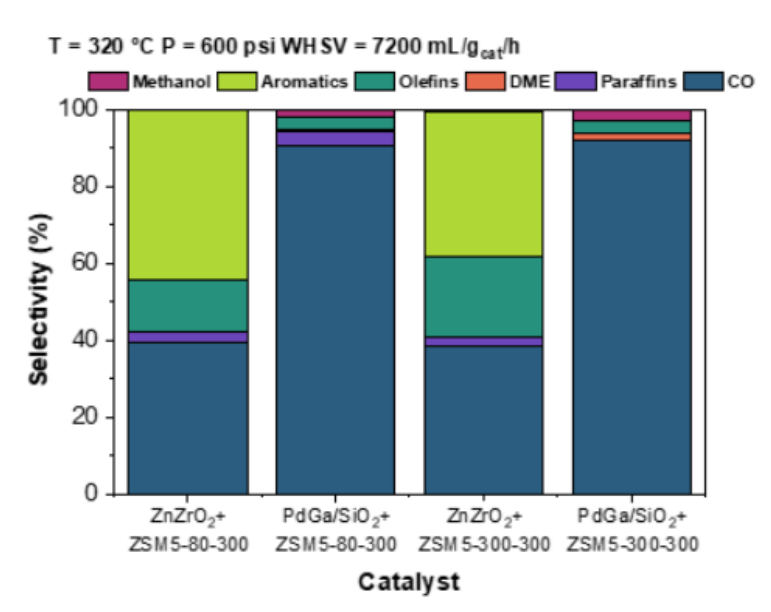


Figure 60: Product distribution of CO<sub>2</sub> hydrogenation over ZnZrO and PdGa/SiO<sub>2</sub> tandem catalysts

Figure 61 presents CO<sub>2</sub> conversion and product selectivity of the PdGa/SiO<sub>2</sub>+ZSM5 tandem catalyst from 340-280 °C at 600 psi and 7200 mL/g<sub>cat</sub>/h. CO, MeOH, DME and olefins were the main products detected for all temperatures. At high temperatures, CO and olefins selectivity increases from 80 to 96% and from 1 to 3%, respectively. Moreover, at low temperatures MeOH selectivity increases, following Le Châtelier's principle.

However, as the temperature decreases, DME also increases from MeOH dehydration reaction over the zeolite acid sites.

It can be concluded that alloy catalysts are not suitable for tandem reaction of  $CO_2$  to aromatics, because operating conditions between MeOH synthesis and aromatics production are not compatible. For instance, high MeOH selectivity is obtained at temperature below 280 °C, while aromatic synthesis from methanol is favored at temperature above 300 °C.

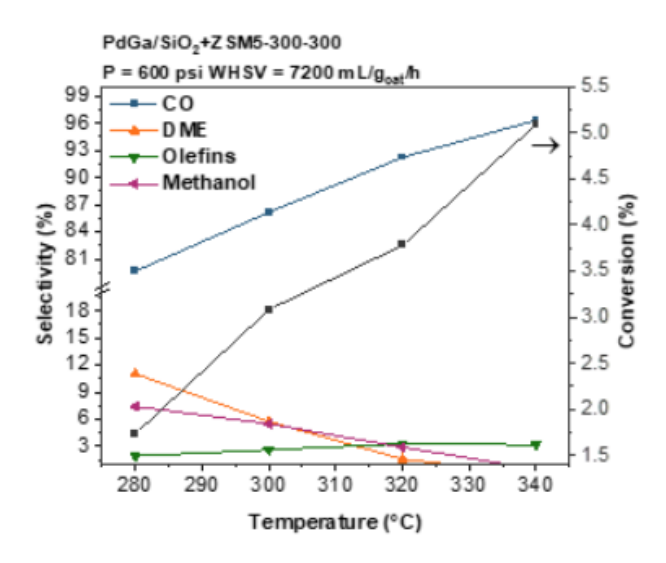


Figure 61: CO<sub>2</sub> conversion and products selectivity of CO<sub>2</sub> hydrogenation over PdGa/SiO<sub>2</sub>+ZSM-5-300-300 tandem catalyst at different temperatures

### D. Conclusions

The best performing catalyst PdGa/SiO<sub>2</sub> was mixed with H-ZSM-5 and tested for CO<sub>2</sub> hydrogenation for aromatics production. PdGa/SiO<sub>2</sub>/H-ZSM-5 shows little to no production of aromatics at temperatures between 280-340 °C. Due to low rates of MeOH production, it is expected that there was not much hydrogenation reaction and hence CO was the major product in the stream. Of the analysis done so far, ZnZrO/H-ZSM-5 shows the highest aromatics selectivity.

# III. Task 13.0 - Technology assessment of intensified reactor

# A. Goals and Objectives of the Task

The Recipient will assess the CO<sub>2</sub> footprint and techno-economic feasibility of the reaction process.

<u>Subtask 13.1 – Carbon footprint</u>: The Recipient will calculate carbon footprint of this process based on the collected data. This will be a key component of a life cycle assessment (LCA) focused on the reactions proposed and the reactor. The recipient will consider the use of water by the process, and the derived measures of LCA from energy

use such as contributions to eutrophication and acid rain using standard LCA tools. The boundary of the process will be the reactor system necessary to convert CO<sub>2</sub> from coal into aromatic products and will not include separation, distribution and ultimate fate of those aromatics within a chemical complex.

<u>Subtask 13.2 – Assess need for CO<sub>2</sub> purification</u>: The Recipient will determine if using raw flue gas (15% CO<sub>2</sub>) is feasible for aromatics production, or whether use of concentrated CO<sub>2</sub> improves overall techno-economics

## B. Background and Research Methods

To assess utility consumption and other process inputs, an initial chemical process flowsheet has been created on AspenPlus based on literature data for the CO<sub>2</sub> to BTX through the Fischer-Tropsch (FT) route. This flowsheet was then changed to better reflect the proposed process, specifically in the reactor specifications and the separation route used. The RWGS reaction is treated separately, under the assumption that it achieves equilibrium in a shorter timescale than those of other reactions. In the absence of a complete mechanistic model, the strategy thus far adopted for the FT-route, which might also be applied to the methanol-route for the tandem catalyst developed in this project, is the "design about", where a single operating condition is considered, in agreement with the laboratory-scale experimental conditions.

### C. Results and Discussions

## (i) Subtask 13.1 – Carbon Footprint

The AspenPlus flowsheets are shown below to highlight the changes that have been made. Two major changes were made to the separation of condensable hydrocarbons from water and light/non-condensable gases. The 2-flash separator block was replaced by a 3-flash separator to better reflect the desired separation of water from liquid hydrocarbons and gases and membrane separator blocks was replaced by a second 3-flash separator to minimize the amount of compression needed for the recycle stream and to achieve the desired recycle of H<sub>2</sub>, CO<sub>2</sub>, and CO. In addition, a purge stream was also added to avoid buildup of inert components in the system. More work needs to be done on the separation route, as the current model gives high quantities of benzene and other lighter aromatics in the vapor streams of the flash separators – which is undesirable, as the aim is for these light aromatics to be products, rather than be recycled or purged from the system. It is also important to note that the light gas and water recycle streams are not currently working/configured, so work will also be done in this area.

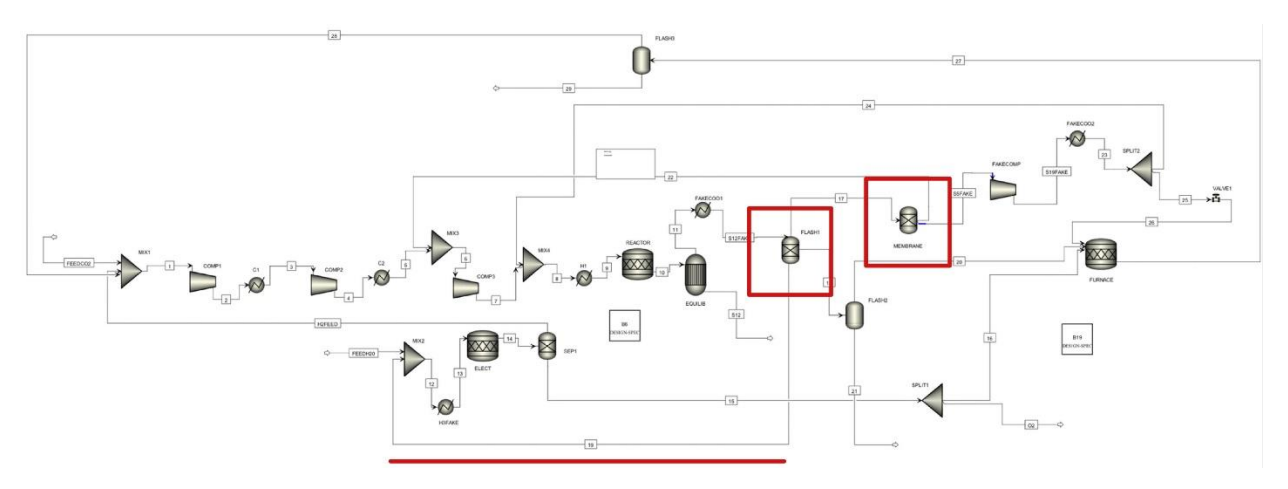


Figure 62. Original AspenPlus flowsheet through the FT route. Changed units and streams are shown in red.

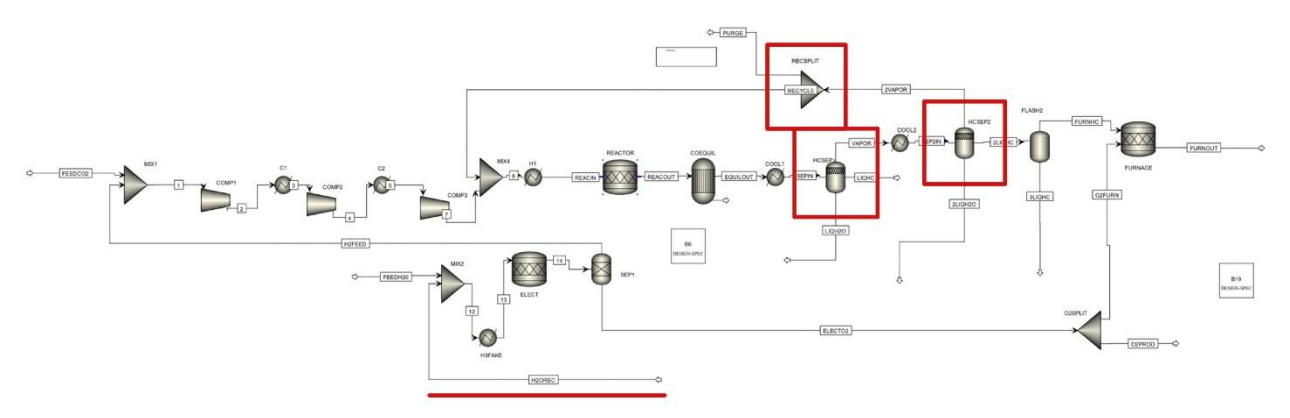


Figure 63. Modified AspenPlus flowsheet, reflecting the changes described above. Changed units and streams are shown in red.

Detailed below are the current reactor specifications and reaction inputs, the fraction of CO<sub>2</sub> that is converted into each main subgroup (paraffins, olefins, and C6 & C7+ aromatics) and the distribution of components within each subgroup. The reactor specifications and subgroup conversion fractions were found using experimental data, whereas literature data were used to estimate the distribution of components within each subgroup.

Table 11. AspenPlus RStoic Reactor Specifications and Reaction Inputs.

T (°C)	320
P (psi)	600
Reactions (CO <sub>2</sub> Fractional Conversion	<u> </u>
Methane	0.01386
Ethane	0.00685
Propane	0.00274
n-Butane	0.00137
n-Heptane	0.01422
Ethylene	0.00737
Propylene	0.00293
1-Butene	0.00147
Benzene	0.00014
Ethylbenzene	0.00154
Tetramethylbenzene	0.00322
Trimethylbenzene	0.01092
Toluene	0.00038
m-Xylene	0.00051
o-Xylene	0.00028
p-Xylene	0.00048
Naphthalene	0.00005
1-methylnaphthalene	0.00006
2,6-dimethylnaphthalene	0.00005
Total	0.06840

Table 12. CO<sub>2</sub> Conversion Fractions for Main Component Subgroup. \*Total CO<sub>2</sub> conversion number does not include the production of CO, which is simulated separately in an equilibrium reactor.

Total	Subgroup CO₂ Conversion Fractions					
CO₂ Conversion*	Paraffins	Olefins	C <sub>6</sub> Aromatics	C <sub>7</sub> + Aromatics		
6.84%	57.04%	17.19%	23.13%	2.65%		

Table 13. Component Distributions for Main Component Subgroups.

Paraffins (57.04%)	
Methane	35.50%
Ethane	17.54%
Propane	7.02%
n-Butane	3.50%
n-Heptane	36.44%
Olefins (17.19%)	
Ethylene	62.66%
Propylene	24.88%
1-Butene	12.46%
Benzene Aromatics (23.13%)	
Benzene	0.87%
Ethylbenzene	9.76%
Tetramethylbenzene	20.36%
Trimethylbenzene	69.01%
C <sub>7</sub> + Aromatics (2.65%)	_
Toluene	21.21%
m-Xylene	27.93%
o-Xylene	15.43%
p-Xylene	26.78%
Naphthalene	2.67%
1-methylnaphthalene	3.12%
2,6-dimethylnaphthalene	2.86%

Preliminary estimations for the life cycle analysis (LCA) of the reaction have been found through ApsenPlus, as shown below. Heat duty, CO2e production, and cooling water usage are estimated in Aspen for both the stoichiometric and equilibrium reactors as part of the operation block summaries. As the reaction section of the process is simulated by both reactors, the values in the table reflect the sum of the values for each reactor.

Table 14. Preliminary Life Cycle Analysis measures for the reaction. Includes the stoichiometric and equlibrium reactor blocks on AspenPlus. \*Products is defined as hydrocarbons including and heavier than benzene.

Reactor No	-401000			
Total CO26	-12600			
Cooling products*]	Water	Usage	[kg/hr-kg	232

Next steps include refinement of the separation process to achieve greater separation of hydrocarbon products from non-condensable gases, achieving a working recycle stream to feed into the reactor, and a more rigorous life cycle analysis on the hydrogen production, reaction, and separation sections of the AspenPlus simulation.

To assess utility consumption and other process inputs, an initial chemical process flowsheet has been created on AspenPlus based on literature data for the CO<sub>2</sub> to BTX through the Fischer-Tropsch (FT) route. This flowsheet was then changed to better reflect the proposed process, specifically in the reactor specifications and the separation route used. The RWGS reaction is treated separately, under the assumption that it achieves equilibrium in a shorter timescale than those of other reactions. In the absence of a complete mechanistic model, the strategy thus far adopted for the FT-route, which might also be applied to the methanol-route for the tandem catalyst developed in this project, is the "design about", where a single operating condition is considered, in agreement with the laboratory-scale experimental conditions.

The AspenPlus process flowsheet is shown below in seven sections: feed, compression, mixing and heating, reaction, hydrocarbon separation, recycle, and furnace. The feed section assumes pure  $CO_2$  and  $H_2$  are fed into the process at atmospheric conditions. These streams then go through a compression train to reach the desired reaction pressure of 600 psi. The feed streams are mixed with the recycle stream, all at 600 psi, and heated to the desired reaction temperature of 320 C using a gas-fired heater. The resulting stream then goes through the stoichiometric reactor and a water-gas shift equilibrium reactor, with an overall  $CO_2$  conversion rate of 10% (the details of the reactor and conversion amounts are given below in Tables 6-8). The hydrocarbon products are then separated out from the water and light gases coming out of the reaction section using two 3-phase flash separators, the first operating at 600 psi and 40 °C and the second operating at 0 °C. Finally, the vapor stream out of the second separator, containing most of the unconverted  $CO_2$  and  $CO_2$  and  $CO_3$  are light hydrocarbons, is split 85:15 to be recycled and combusted, respectively.

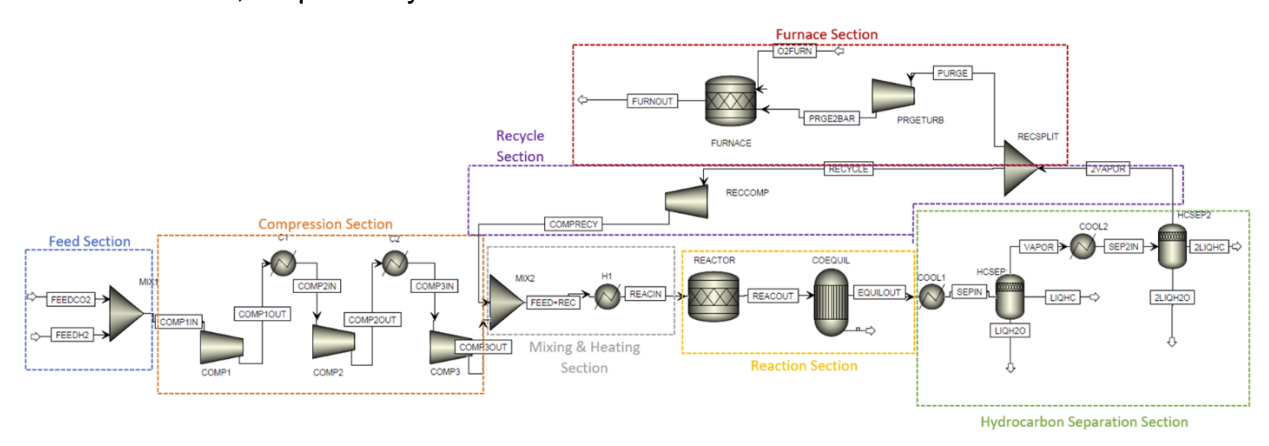


Figure 64: Process Flow Diagram of the Macroscale Model designed in AspenPlus

Detailed below are the current reactor specifications and reaction inputs, the fraction of CO<sub>2</sub> that is converted into each main subgroup (paraffins, olefins, and C6 & C7+ aromatics) and the distribution of components within each subgroup. The reactor specifications and subgroup conversion fractions were found using experimental data, whereas literature data were used to estimate the distribution of components within each subgroup.

Table 15. AspenPlus RStoic Reactor Specifications and Reaction Inputs.

T (°C)	320
P (psi)	600
Reactions (CO <sub>2</sub> Fractional Convers	ion)
Methane	0.01386
Ethane	0.00685
Propane	0.00274
n-Butane	0.00137
n-Heptane	0.01422
Ethylene	0.00737
Propylene	0.00293
1-Butene	0.00147
Benzene	0.00014
Ethylbenzene	0.00154
Tetramethylbenzene	0.00322
Trimethylbenzene	0.01092
Toluene	0.00038
m-Xylene	0.00051
o-Xylene	0.00028
p-Xylene	0.00048
Naphthalene	0.00005
1-methylnaphthalene	0.00006
2,6-dimethylnaphthalene	0.00005
Total	0.06840

Table 16. CO<sub>2</sub> Conversion Fractions for Main Component Subgroup. \*Total CO<sub>2</sub> conversion number does not include the production of CO, which is simulated separately in an equilibrium reactor.

Total	Subgroup CO₂ Conversion Fractions					
CO <sub>2</sub> Conversion*	Paraffins	Olefins	C <sub>6</sub> Aromatics	C <sub>7</sub> + Aromatics		
6.84%	57.04%	17.19%	23.13%	2.65%		

Table 17. Component Distributions for Main Component Subgroups.

Paraffins (57.04%) 35.50% Methane 17.54% Ethane Propane 7.02% n-Butane 3.50% 36.44% n-Heptane Olefins (17.19%) Ethylene 62.66% 24.88% Propylene 1-Butene 12.46% Benzene Aromatics (23.13%) 0.87% Benzene 9.76% Ethylbenzene Tetramethylbenzene 20.36% Trimethylbenzene 69.01%  $C_7$ + Aromatics (2.65%) Toluene 21.21% m-Xylene 27.93% o-Xylene 15.43% p-Xylene 26.78% Naphthalene 2.67% 3.12% 1-methylnaphthalene 2,6-dimethylnaphthalene 2.86%

Preliminary estimations for the life cycle analysis (LCA) of the reaction have been found through AspenPlus, as shown below. The heat duties of each process unit are estimated using the results given in AspenPlus, given in MW. This is then converted to watt-hours and normalized against the flowrate of liquid hydrocarbon product to get energy usage in kwh/kg HC product. This energy usage is used in combination with the utility used by each process unit to find the global warming potential (GWP) in kg CO2e/kg HC product. The GWP of each process unit and the CO2 in and out of the process (also normalized against kg HC product) are combined to get the total GWP of the process. Finally, this is compared to the GWP of the production of benzene via catalytic reforming (in kg CO2e/kg benzene product).

Table 18. Utilities, Heat Duties, and Normalized Energy Usage for Each Process Unit

Unit	Utility Type	Duty (MW)	kWh/kg HC product*
Feed Compressor Train	Electricity	42.8	5.24
Feed Coolers	Cooling Water	-24.1	2.96
Reactor		-39.5	-
1st Separator	Cooling Water	-312.6	38.28
2nd Separator	Refrigeration	-37.2	4.56
Purge Turbine		-5.0	
Purge Furnace		-342.0	
Furnace Heat Integration**		-105.4	
Recycle Compressor	Electricity	1.8	0.22
Gas Heater	Hot Oil	295.7	36.22
Gas Heater Heat Integration**	Hot Oil	190.3	23.31

<sup>\*</sup>For 8165 kg/hr of liquid hydrocarbon product

Table 19. GWP of Each Process Unit and Total GWP of the Macroscale Model, Compared to Benzene

Unit/Stream	Туре	Duty (kWh/kg product)	Original Energy Source	Efficiency	kgCO2e/ kWh	kg CO2e/kg HC product
CO <sub>2</sub> In						-15.31
CO <sub>2</sub> Out						11.80
Feed Compressor Train	Electricity	5.24	Electricity	100%	0.505	2.65
Feed Coolers	Cooling Water*	2.96		100%		0.05
1st Separator	Cooling Water*	38.28		100%		0.71
2nd Separator	Refrigeration	4.56	Ammonia	90%	0.350	1.60
Recycle Compressor	Electricity	0.22	Electricity	100%	0.505	0.11
Gas Heater	Hot Oil	23.31	Natural Gas	85%	0.219	5.10
Total						6.71
Benzene Com	parison (kg CO2	e/kg benzen	e product)			1.86

<sup>\*</sup>Cooling Water GWP is calculated as a function of the amount of freshwater needed per hour, based on literature values

As shown above in the table, the GWP of this process, without consideration of hydrogen production GWP, is significantly greater than that of catalytic reformed benzene. Further work will be done to produce additional GWP analyses for cases of 15%, 20%, and 25%

<sup>\*\*</sup>The furnace and gas-fired heater were heat integrated to represent the actual energy usage of the gas-fired heater if the heat from the furnace was first used to heat up the stream that enters the reactor.

conversion of CO<sub>2</sub> in the reaction section of the process, as well as for cases where hydrogen production GWP is considered.

## (ii) Subtask 13.2 – Assess need for CO2 purification

A comparison between a scenario with raw flue-gas and purified CO<sub>2</sub> streams on the basis of 125,000 kg/hr of CO<sub>2</sub> for either scenario and 15% conversion. The heat duties of each major unit are given in Table 20, as well as the difference between them. The utilization of raw flue-gas leads to incremental utility consumption in all reaction sections.

	Flue Coe Heat	Pure	CO <sub>2</sub>	A book ito	
Unit	Flue Gas Heat Duties (MWh)	Heat (MWh)	Duty	Absolute Difference	Utility
1st Sep	-295	-117.3		177.7	Cooling water
2nd Sep	-28.91	-12.31		16.6	Ammonia
Pre-Reactor Heater	155.11	88.8		66.31	Natural Gas
H2 Elect	665.8	624.27		41.53	Electricity
H2 + CO2 Compression	168.03	44.3		123.73	Electricity

Table 20. Utility duties comparison between the flue gas and purified CO<sub>2</sub> scenarios

Additionally, the electrical duty of each scenario is shown in Table 21, where the electricity needed to purify CO<sub>2</sub> (2.8 GJ/ton CO<sub>2</sub>, 125,000 kg/h CO<sub>2</sub>), and the total differences are also reported. Due to significant increases in electrical heat duty as well as cooling water, ammonia, and natural gas utilities, purification of CO<sub>2</sub> before the process is recommended.

	, ,	•
	Flue Gas Electrical Duty (MWh)	Pure CO <sub>2</sub> Electrical Duty (MWh)
	(IVIVVII)	(1010011)
Compression Train	168.03	44.3
Hydrogen Electrolyzer	665.8	624.3
CO <sub>2</sub> Purification	0	97.2
Total	833.8	765.8

Table 21. Electrical duty comparsion between the flue gas and purified CO<sub>2</sub> scenarios

#### D. Conclusions

An Aspen simulation for carbon footprint was performed. It is found that the current process yields a greater carbon footprint than the current process of production of benzene. However, it is estimated that there is benefit of purifying the waste CO<sub>2</sub> stream to further improve the carbon footprint as well as the overall utilities cost.

### IV. References

- (1) Grabow, L. C.; Mavrikakis, M. Mechanism of Methanol Synthesis on Cu through CO2 and CO Hydrogenation. *ACS Catal* **2011**, *1* (4), 365–384. https://doi.org/10.1021/cs200055d.
- (2) Medford, A. J.; Shi, C.; Hoffmann, M. J.; Lausche, A. C.; Fitzgibbon, S. R.; Bligaard, T.; Nørskov, J. K. CatMAP: A Software Package for Descriptor-Based Microkinetic Mapping of Catalytic Trends. *Catal Letters* **2015**, *145* (3), 794–807. https://doi.org/10.1007/s10562-015-1495-6.
- (3) Grossale, A.; Nova, I.; Tronconi, E.; Chatterjee, D.; Weibel, M. NH3-NO/NO2 SCR for Diesel Exhausts Aftertreatment: Reactivity, Mechanism and Kinetic Modelling of Commercial Fe- and Cu-Promoted Zeolite Catalysts. *Top Catal* **2009**, *52* (13–20), 1837–1841. https://doi.org/10.1007/s11244-009-9354-6.
- (4) Hansen, M. H.; Nørskov, J. K.; Bligaard, T. First Principles Micro-Kinetic Model of Catalytic Non-Oxidative Dehydrogenation of Ethane over Close-Packed Metallic Facets. *J Catal* **2019**, *374*, 161–170. https://doi.org/10.1016/j.jcat.2019.03.034.
- (5) Nezam, I.; Zhou, W.; Gusmão, G. S.; Realff, M. J.; Wang, Y.; Medford, A. J.; Jones, C. W. Direct Aromatization of CO2 via Combined CO2 Hydrogenation and Zeolite-Based Acid Catalysis. *Journal of CO2 Utilization* 2021, 45, 101405. https://doi.org/10.1016/j.jcou.2020.101405.
- (6) Xu, Y.; Shi, C.; Liu, B.; Wang, T.; Zheng, J.; Li, W.; Liu, D.; Liu, X. Selective Production of Aromatics from CO2. *Catal Sci Technol* **2019**, *9* (3), 593–610. https://doi.org/10.1039/C8CY02024H.
- (7) Ni, Y.; Chen, Z.; Fu, Y.; Liu, Y.; Zhu, W.; Liu, Z. Selective Conversion of CO2 and H2 into Aromatics. *Nat Commun* 2018, 9 (1), 1–7. https://doi.org/10.1038/s41467-018-05880-4.
- (8) Cheng, K.; Kang, J.; King, D. L.; Subramanian, V.; Zhou, C.; Zhang, Q.; Wang, Y. Advances in Catalysis for Syngas Conversion to Hydrocarbons. *Advances in Catalysis* **2017**, *60*, 125–208. https://doi.org/10.1016/BS.ACAT.2017.09.003.
- (9) Yang, X.; Su, X.; Chen, D.; Zhang, T.; Huang, Y. Direct Conversion of Syngas to Aromatics: A Review of Recent Studies. *Chinese Journal of Catalysis*. Science Press April 1, 2020, pp 561–573. https://doi.org/10.1016/S1872-2067(19)63346-2.
- (10) Kondrat, S. A.; Smith, P. J.; Lu, L.; Bartley, J. K.; Taylor, S. H.; Spencer, M. S.; Kelly, G. J.; Park, C. W.; Kiely, C. J.; Hutchings, G. J. Preparation of a Highly Active Ternary Cu-Zn-Al Oxide Methanol Synthesis Catalyst by Supercritical CO2 Anti-Solvent Precipitation. *Catal Today* 2018, 317 (March), 12–20. https://doi.org/10.1016/j.cattod.2018.03.046.
- (11) Kiener, C.; Kurtz, M.; Wilmer, H.; Hoffmann, C.; Schmidt, H. W.; Grunwaldt, J. D.; Muhler, M.; Schüth, F. High-Throughput Screening under Demanding Conditions:

- Cu/ZnO Catalysts in High Pressure Methanol Synthesis as an Example. *J Catal* **2003**, *216* (1–2), 110–119. https://doi.org/10.1016/S0021-9517(02)00134-3.
- (12) Baltes, C.; Vukojević, S.; Schüth, F. Correlations between Synthesis, Precursor, and Catalyst Structure and Activity of a Large Set of CuO/ZnO/Al2O3 Catalysts for Methanol Synthesis. *J Catal* **2008**, *258* (2), 334–344. https://doi.org/10.1016/j.jcat.2008.07.004.
- (13) Cui, X.; Gao, P.; Li, S.; Yang, C.; Liu, Z.; Wang, H.; Zhong, L.; Sun, Y. Selective Production of Aromatics Directly from Carbon Dioxide Hydrogenation. *ACS Catal* **2019**, *9* (5), 3866–3876. https://doi.org/10.1021/acscatal.9b00640.
- (14) Li, Z.; Qu, Y.; Wang, J.; Liu, H.; Li, M.; Miao, S.; Li, C. Highly Selective Conversion of Carbon Dioxide to Aromatics over Tandem Catalysts. *Joule* **2019**, 3 (2), 570–583. https://doi.org/10.1016/j.joule.2018.10.027.
- (15) Xu, C.; Jiang, B.; Liao, Z.; Wang, J.; Huang, Z.; Yang, Y. Effect of Metal on the Methanol to Aromatics Conversion over Modified ZSM-5 in the Presence of Carbon Dioxide. *RSC Adv* **2017**, *7*(18), 10729–10736. https://doi.org/10.1039/c6ra27104a.
- (16) Nithyanandam, R.; Mun, Y. K.; Fong, T. S.; Siew, T. C.; Yee, O. S.; Ismail, N. Review on Production of Benzene from Petroleum Associated Gas by Dehydroaromatization, Partial Oxidation of Methane and Methanol-to-Aromatics Processes. *Journal of Engineering Science and Technology* 2018, 13 (12), 4290–4309.
- (17) Satthawong, R.; Koizumi, N.; Song, C.; Prasassarakich, P. Bimetallic Fe-Co Catalysts for CO2 Hydrogenation to Higher Hydrocarbons. *Journal of CO2 Utilization* **2013**, 3–4, 102–106. https://doi.org/10.1016/j.jcou.2013.10.002.
- (18) Mota, F. M.; Kim, D. H. From CO2 Methanation to Ambitious Long-Chain Hydrocarbons: Alternative Fuels Paving the Path to Sustainability. *Chem Soc Rev* **2019**, *48* (1), 205–259. https://doi.org/10.1039/c8cs00527c.
- (19) Wang, J.; Li, G.; Li, Z.; Tang, C.; Feng, Z.; An, H.; Liu, H.; Liu, T.; Li, C. A Highly Selective and Stable ZnO-ZrO2 Solid Solution Catalyst for CO2 Hydrogenation to Methanol. Sci Adv 2017, 3 (10). https://doi.org/10.1126/SCIADV.1701290/SUPPL FILE/1701290 SM.PDF.
- (20) Zhou, C.; Shi, J.; Zhou, W.; Cheng, K.; Zhang, Q.; Kang, J.; Wang, Y. Highly Active ZnO-ZrO2 Aerogels Integrated with H-ZSM-5 for Aromatics Synthesis from Carbon Dioxide. ACS Catal 2020, 10 (1), 302–310. https://doi.org/10.1021/ACSCATAL.9B04309/SUPPL\_FILE/CS9B04309\_SI\_001. PDF.
- (21) Wang, Y.; Kazumi, S.; Gao, W.; Gao, X.; Li, H.; Guo, X.; Yoneyama, Y.; Yang, G.; Tsubaki, N. Direct Conversion of CO2 to Aromatics with High Yield via a Modified Fischer-Tropsch Synthesis Pathway. *Appl Catal B* **2020**, *269*, 118792. https://doi.org/10.1016/J.APCATB.2020.118792.

- (22) Liu, X.; Wang, M.; Zhou, C.; Zhou, W.; Cheng, K.; Kang, J.; Zhang, Q.; Deng, W.; Wang, Y. Selective Transformation of Carbon Dioxide into Lower Olefins with a Bifunctional Catalyst Composed of ZnGa2O4 and SAPO-34. *Chemical Communications* **2017**, *54* (2), 140–143. https://doi.org/10.1039/c7cc08642c.
- (23) Li, N.; Meng, C.; Liu, D. Deactivation Kinetics with Activity Coefficient of the Methanol to Aromatics Process over Modified ZSM-5. *Fuel* **2018**, 233 (January), 283–290. https://doi.org/10.1016/j.fuel.2018.06.044.
- (24) Park, Y. K.; Park, K. C.; Ihm, S. K. Hydrocarbon Synthesis through CO2 Hydrogenation over CuZnOZrO2/Zeolite Hybrid Catalysts. *Catal Today* **1998**, *44* (1–4), 165–173. https://doi.org/10.1016/S0920-5861(98)00187-4.
- (25) Zhang, X.; Zhang, A.; Jiang, X.; Zhu, J.; Liu, J.; Li, J.; Zhang, G.; Song, C.; Guo, X. Utilization of CO2 for Aromatics Production over ZnO/ZrO2-ZSM-5 Tandem Catalyst. *Journal of CO2 Utilization* **2019**, *29* (December 2018), 140–145. https://doi.org/10.1016/j.jcou.2018.12.002.
- (26) Wang, Y.; Tan, L.; Tan, M.; Zhang, P.; Fang, Y.; Yoneyama, Y.; Yang, G.; Tsubaki, N. Rationally Designing Bifunctional Catalysts as an Efficient Strategy to Boost CO 2 Hydrogenation Producing Value-Added Aromatics. ACS Catal 2019, 9 (2), 895–901. https://doi.org/10.1021/ACSCATAL.8B01344/SUPPL\_FILE/CS8B01344\_SI\_001.PDF.
- (27) James Speight, Ph. D. *Lange's Handbook of Chemistry, Sixteenth Edition*, 16th ed. /.; McGraw-Hill Education: New York, 2005.
- (28) Guo, L.; Sun, J.; Ge, Q.; Tsubaki, N. Recent Advances in Direct Catalytic Hydrogenation of Carbon Dioxide to Valuable C2+ Hydrocarbons. *J Mater Chem A Mater* **2018**, *6* (46), 23244–23262. https://doi.org/10.1039/C8TA05377D.
- (29) Zhang, Q.; Chen, G.; Wang, Y.; Chen, M.; Guo, G.; Shi, J.; Luo, J.; Yu, J. High-Quality Single-Crystalline MFI-Type Nanozeolites: A Facile Synthetic Strategy and MTP Catalytic Studies. *Chemistry of Materials* 2018, 30 (8), 2750–2758. https://doi.org/10.1021/ACS.CHEMMATER.8B00527/SUPPL\_FILE/CM8B00527\_SI\_001.PDF.
- (30) Biscardi, J. A.; Iglesia, E. Reaction Pathways and Rate-Determining Steps in Reactions of Alkanes on H-ZSM5 and Zn/H-ZSM5 Catalysts. *J Catal* **1999**, *182* (1), 117–128. https://doi.org/10.1006/JCAT.1998.2312.
- (31) Zhang, J.; Zhang, M.; Chen, S.; Wang, X.; Zhou, Z.; Wu, Y.; Zhang, T.; Yang, G.; Han, Y.; Tan, Y. Hydrogenation of CO2 into Aromatics over a ZnCrOx–Zeolite Composite Catalyst. *Chemical Communications* **2019**, *55* (7), 973–976. https://doi.org/10.1039/C8CC09019J.
- (32) Medford, A. J.; Shi, C.; Hoffmann, M. J.; Lausche, A. C.; Fitzgibbon, S. R.; Bligaard, T.; Nørskov, J. K. CatMAP: A Software Package for Descriptor-Based Microkinetic

- Mapping of Catalytic Trends. *Catal Letters* **2015**, *145* (3), 794–807. https://doi.org/10.1007/s10562-015-1495-6.
- (33) Grabow, L. C.; Mavrikakis, M. Mechanism of Methanol Synthesis on Cu through CO2 and CO Hydrogenation. *ACS Catal* **2011**, *1* (4), 365–384. https://doi.org/10.1021/cs200055d.
- (34) Falsig, H.; Shen, J.; Khan, T. S.; Guo, W.; Jones, G.; Dahl, S.; Bligaard, T. On the Structure Sensitivity of Direct NO Decomposition over Low-Index Transition Metal Facets. *Top Catal* **2014**. https://doi.org/10.1007/s11244-013-0164-5.
- (35) Falsig, H.; Hvolbæk, B.; Kristensen, I. S.; Jiang, T.; Bligaard, T.; Christensen, C. H.; Nørskov, J. K. Trends in the Catalytic CO Oxidation Activity of Nanoparticles. *Angewandte Chemie - International Edition* **2008**. https://doi.org/10.1002/anie.200801479.
- (36) Wang, C.-M.; Brogaard, R. Y.; Weckhuysen, B. M.; Nørskov, J. K.; Studt, F. Reactivity Descriptor in Solid Acid Catalysis: Predicting Turnover Frequencies for Propene Methylation in Zeotypes. *J Phys Chem Lett* **2014**, *5* (9), 1516–1521. https://doi.org/10.1021/jz500482z.
- (37) Schumann, J.; Medford, A. J.; Yoo, J. S.; Zhao, Z. J.; Bothra, P.; Cao, A.; Studt, F.; Abild-Pedersen, F.; Nørskov, J. K. Selectivity of Synthesis Gas Conversion to C2+ Oxygenates on Fcc(111) Transition-Metal Surfaces. *ACS Catal* **2018**, *8* (4), 3447–3453. https://doi.org/10.1021/acscatal.8b00201.
- (38) Gusmão, G. S.; Christopher, P. A General and Robust Approach for Defining and Solving Microkinetic Catalytic Systems. *AIChE Journal* **2015**, *61* (1), 188–199. https://doi.org/10.1002/aic.14627.
- (39) Shomate, C. H. A Method for Evaluating and Correlating Thermodynamic Da Ta. *J Phys Chem* **1954**, *58* (4), 368–372. https://doi.org/10.1021/j150514a018.
- (40) Evans, M. G.; Polanyi, M. Some Applications of the Transition State Method to the Calculation of Reaction Velocities, Especially in Solution. *Transactions of the Faraday Society* **1935**, *31*, 875. https://doi.org/10.1039/tf9353100875.
- (41) Wang, S.; Temel, B.; Shen, J.; Jones, G.; Grabow, L. C.; Studt, F.; Bligaard, T.; Abild-Pedersen, F.; Christensen, C. H.; Nørskov, J. K. Universal Brønsted-Evans-Polanyi Relations for C–C, C–O, C–N, N–O, N–N, and O–O Dissociation Reactions. *Catal Letters* **2011**, *141* (3), 370–373. https://doi.org/10.1007/s10562-010-0477-y.
- (42) Wang, S.; Petzold, V.; Tripkovic, V.; Kleis, J.; Howalt, J. G.; Skúlason, E.; Fernández, E. M.; Hvolbæk, B.; Jones, G.; Toftelund, A.; Falsig, H.; Björketun, M.; Studt, F.; Abild-Pedersen, F.; Rossmeisl, J.; Nørskov, J. K.; Bligaard, T. Universal Transition State Scaling Relations for (de)Hydrogenation over Transition Metals. *Physical Chemistry Chemical Physics* 2011, 13 (46), 20760. https://doi.org/10.1039/c1cp20547a.

- (43) Ulissi, Z. W.; Medford, A. J.; Bligaard, T.; Nørskov, J. K. To Address Surface Reaction Network Complexity Using Scaling Relations Machine Learning and DFT Calculations. *Nat Commun* **2017**, 8 (1), 14621. https://doi.org/10.1038/ncomms14621.
- (44) PACE. {P}artnership for an {A}dvanced {C}omputing {E}nvironment ({PACE}). 2017.
- (45) Wellendorff, J.; Lundgaard, K. T.; Møgelhøj, A.; Petzold, V.; Landis, D. D.; Nørskov, J. K.; Bligaard, T.; Jacobsen, K. W. Density Functionals for Surface Science: Exchange-Correlation Model Development with Bayesian Error Estimation. *Phys Rev B* **2012**, *85* (23), 235149. https://doi.org/10.1103/PhysRevB.85.235149.
- (46) Perdew, J. P.; Burke, K.; Ernzerhof, M. Generalized Gradient Approximation Made Simple. *Phys Rev Lett* **1996**, *77* (18), 3865–3868. https://doi.org/10.1103/PhysRevLett.77.3865.
- (47) Kim, S. D.; Noh, S. H.; Park, J. W.; Kim, W. J. Organic-Free Synthesis of ZSM-5 with Narrow Crystal Size Distribution Using Two-Step Temperature Process. *Microporous and Mesoporous Materials* **2006**, *92* (1–3), 181–188. https://doi.org/10.1016/j.micromeso.2006.01.009.
- (48) Yang, N.; Medford, A. J.; Liu, X.; Studt, F.; Bligaard, T.; Bent, S. F.; Nørskov, J. K. Intrinsic Selectivity and Structure Sensitivity of Rhodium Catalysts for C 2+ Oxygenate Production. *J Am Chem Soc* 2016, 138 (11), 3705–3714. https://doi.org/10.1021/jacs.5b12087.
- (49) Medford, A. J.; Lausche, A. C.; Abild-Pedersen, F.; Temel, B.; Schjødt, N. C.; Nørskov, J. K.; Studt, F. Activity and Selectivity Trends in Synthesis Gas Conversion to Higher Alcohols. *Top Catal* **2014**, *57* (1–4), 135–142. https://doi.org/10.1007/s11244-013-0169-0.
- (50) Winther, K. T.; Hoffmann, M. J.; Boes, J. R.; Mamun, O.; Bajdich, M.; Bligaard, T. Catalysis-Hub.Org, an Open Electronic Structure Database for Surface Reactions. *Sci Data* **2019**, *6* (1), 1–10. https://doi.org/10.1038/s41597-019-0081-y.
- (51) Chase, M. W. NIST-JANEF Thermochemical Tables, Fourth Edition. *Journal of Physical Chemistry*. 1998.
- (52) Liu, L.; Fan, F.; Jiang, Z.; Gao, X.; Wei, J.; Fang, T. Mechanistic Study of Pd–Cu Bimetallic Catalysts for Methanol Synthesis from CO2 Hydrogenation. *Journal of Physical Chemistry C* 2017, 121 (47), 26287–26299. https://doi.org/10.1021/ACS.JPCC.7B06166.
- (53) Studt, F.; Sharafutdinov, I.; Abild-Pedersen, F.; Elkjaer, C. F.; Hummelshøj, J. S.; Dahl, S.; Chorkendorff, I.; Nørskov, J. K.; Elkjær, C. F.; Hummelshøj, J. S.; Dahl, S.; Chorkendorff, I.; Nørskov, J. K. Discovery of a Ni-Ga Catalyst for Carbon Dioxide Reduction to Methanol. *Nat Chem* **2014**, *6* (4), 320–324. https://doi.org/10.1038/nchem.1873.

- (54) Collins, S. E.; Delgado, J. J.; Mira, C.; Calvino, J. J.; Bernal, S.; Chiavassa, D. L.; Baltanás, M. A.; Bonivardi, A. L. The Role of Pd–Ga Bimetallic Particles in the Bifunctional Mechanism of Selective Methanol Synthesis via CO2 Hydrogenation on a Pd/Ga2O3 Catalyst. *J Catal* 2012, 292, 90–98. https://doi.org/10.1016/J.JCAT.2012.05.005.
- (55) Studt, F.; Sharafutdinov, I.; Abild-Pedersen, F.; Elkjær, C. F.; Hummelshøj, J. S.; Dahl, S.; Chorkendorff, I.; Nørskov, J. K. Discovery of a Ni-Ga Catalyst for Carbon Dioxide Reduction to Methanol. *Nature Chemistry 2014 6:4* 2014, 6 (4), 320–324. https://doi.org/10.1038/nchem.1873.
- (56) Vanden Bussche, K. M.; Froment, G. F. A Steady-State Kinetic Model for Methanol Synthesis and the Water Gas Shift Reaction on a Commercial Cu/ZnO/Al2O3 Catalyst. *J Catal* **1996**, *161* (1), 1–10. https://doi.org/10.1006/jcat.1996.0156.
- (57) Mignard, D.; Pritchard, C. On the Use of Electrolytic Hydrogen from Variable Renewable Energies for the Enhanced Conversion of Biomass to Fuels. *Chemical Engineering Research and Design* **2008**, *86* (5), 473–487. https://doi.org/10.1016/j.cherd.2007.12.008.
- (58) Graaf, G. H.; Winkelman, J. G. M. M. Chemical Equilibria in Methanol Synthesis Including the Water–Gas Shift Reaction: A Critical Reassessment. *Ind Eng Chem Res* **2016**, *55* (20), 5854–5864. https://doi.org/10.1021/acs.iecr.6b00815.
- (59) Van-Dal, É. S.; Bouallou, C. Design and Simulation of a Methanol Production Plant from CO2 Hydrogenation. *J Clean Prod* **2013**, *57*, 38–45. https://doi.org/10.1016/j.jclepro.2013.06.008.
- (60) Janssens, T. V. W.; Svelle, S.; Olsbye, U. Kinetic Modeling of Deactivation Profiles in the Methanol-to-Hydrocarbons (MTH) Reaction: A Combined Autocatalytic-Hydrocarbon Pool Approach. *J Catal* 2013, 308, 122–130. https://doi.org/10.1016/j.jcat.2013.05.035.
- (61) Janssens, T. V. W.; Svelle, S.; Olsbye, U. Kinetic Modeling of Deactivation Profiles in the Methanol-to-Hydrocarbons (MTH) Reaction: A Combined Autocatalytic-Hydrocarbon Pool Approach. *Journal of Catalysis*. 2013, pp 122–130. https://doi.org/10.1016/j.jcat.2013.05.035.
- (62) Ji, W.; Deng, S. Autonomous Discovery of Unknown Reaction Pathways from Data by Chemical Reaction Neural Network. *J Phys Chem A* **2021**, *125* (4), 1082–1092. https://doi.org/10.1021/ACS.JPCA.0C09316.
- (63) Lagaris, I. E. E.; Likas, A.; Fotiadis, D. I. I. Artificial Neural Networks for Solving Ordinary and Partial Differential Equations. *IEEE Trans Neural Netw* **1998**, *9* (5), 987–1000. https://doi.org/10.1109/72.712178.
- (64) Gusmão, G. S.; Retnanto, A. P.; Cunha, S. C. da; Medford, A. J.; da Cunha, S. C.; Medford, A. J. Kinetics-Informed Neural Networks. *Catal Today* **2020**. https://doi.org/10.1016/j.cattod.2022.04.002.

(65) Kingma, D. P.; Ba, J. L. Adam: A Method for Stochastic Optimization. In 3rd International Conference on Learning Representations, ICLR 2015 - Conference Track Proceedings; International Conference on Learning Representations, ICLR, 2015.